Fall 8-29-2018

Modeling and Simulation of Damage In The Brazilian Indirect Tension Test Using The Finite-Discrete Element Method

Jeremiah C. Leyba
University of New Mexico

Recommended Citation

Jeremiah Christopher Leyba
Candidate

Civil Engineering
Department

This thesis is approved, and it is acceptable in quality and form for publication:

Approved by the Thesis Committee:

Mahmoud Reda Taha, PhD, PEng , Chairperson

John Stormont, PhD, PEng

Esteban Rougier, PhD

MODELING AND SIMULATION OF DAMAGE
IN THE BRAZILIAN INDIRECT TENSION TEST
USING THE FINITE-DISCRETE ELEMENT METHOD

by

JEREMIAH CHRISTOPHER LEYBA

BACHELOR OF SCIENCE, CIVIL ENGINEERING

THESIS

Submitted in Partial Fulfillment of the
Requirements for the Degree of

Master of Science
Civil Engineering

The University of New Mexico
Albuquerque, New Mexico

December, 2018

ACKNOWLEDGEMENTS

MODELING AND SIMULATION OF DAMAGE
IN THE BRAZILIAN INDIRECT TENSION TEST
USING THE FINITE-DISCRETE ELEMENT METHOD

by

Jeremiah Christopher Leyba

B.S., Civil Engineering, University of New Mexico, 2017

M.S., Civil Engineering, University of New Mexico, 2018

ABSTRACT

The Brazilian indirect tension test is used to investigate possible correlations between progressive damage and associated permeability changes. The test offers ease of replicability with a damage behavior known to lead to fracture openings as a tool for interpreting the indirect tensile strength of concrete and rocks. This behavior can lend insight into the nature of tensile damage and fracture progression in association with changes in permeability. The nature of these brittle materials is known to exhibit rapid failures in the Brazilian indirect tension test and require a method to retard the progression of damage for the possibility of acquiring permeability measurements. Experimental results by Rusch et. al., (2018) represent a starting point of a system which measures permeability changes during the Brazilian indirect tension test and a system designed to slow the damage progression seen within the test. These results are replicated and investigated using the finite-discrete element method, which allows for the replication of

both the elastic and post-peak fractured behaviors seen within the test. The model results are used to interpret the progression of damage and its type. Investigations of a sample pre-damaged with a drop tower is also made to observe a differing damage mechanism. The model validates the methodology behind what is called the stiff Brazilian indirect tension test and results from the models indicate that damage progression initiates near the contact points as shear separations, quickly followed by tensile separations along the line of fracture. The FDEM code used is observed to be a useful method for continued investigations into future modifications to the Brazilian indirect tension test for the broader damage and permeability correlation objective.

TABLE OF CONTENTS

LIST OF FIGURES

LIST OF TABLES

CHAPTER 1 | INTRODUCTION

1.1 Motivation

The ability to understand how damage in concrete and rock is related to potential permeability changes is a key concern in many industries. In rock mining and engineering, the use of explosive networks in critical areas for tunnel creation present potential issues for the seepage of fluids and potentially harmful gases into unwanted areas. For the deposition of nuclear waste below ground it is critical to understand the potential for leakage outside of controlled zones. In concrete structures the corrosion of reinforcement could be observed in a new light with a better understanding of the points at which damage in concrete has passed a critical permeability threshold. The potential uses for correlation of damage in concrete and rock to permeability changes are varied and can add valuable insight to a plethora of industries.

One of the key components to the understanding of such a correlation comes from the knowledge of damage progression which can lead to an increase in permeability. As permeability is associated with pore space arrangements and micro paths of flow in concrete and rock, damage which compresses rock or concrete matrices leads to compaction, reducing potential paths of flow and associated permeabilities.(Bernabé et al., 2003). Therefore, mechanisms which lead to fracture openings and creation of connected pore spaces are most advantageous in helping with the understanding of potential increases in permeability which could present a problem in real world scenarios.

One common and reliable test to create tension failures is the Brazilian indirect tension test which facilitates the creation of damage leading to tensile fractures. The opening of microcracks under tensile stress in the indirect tension test allows for the potential creation of connected flow path networks, potentially exhibiting changes in permeability. The test also allows for relative ease in replicability and arrangement of a permeability measurement system, unlike a direct tension test which is difficult to control and not easily replicated. Rusch et. al., (2018) developed a foundation of such a measuring system, which utilizes the Brazilian indirect tension test in combination with an apparent permeability measurement system.

During the process of developing an experimental method attempting to capture changes in flow through a specimen as it is failing in the Brazilian disk test, several mechanical issues appeared. One such issue was the abrupt failure exhibited in concrete specimens, disallowing for any meaningful capture of flow changes near failure as hypothesized. In order to remedy this an attempt to slow the failure process was made by developing a stiff Brazilian indirect tension test, utilizing a mechanism which allows for the reduction of load to the concrete specimens as its stiffness decreases due to damage and cracking. These changes and other modifications to the standard Brazilian indirect tension test need to be understood to realize the damage creation in concrete and rock and its correlation with permeability.

Damage and fracture mechanisms in the Brazilian indirect tension test are not easily understood using classical theories and require the use of in depth numerical modeling methods. A high-performance finite-discrete element method which uses parallel computing power was made available through the geophysics department of Los Alamos

2

National Laboratory. This hybrid method allows for complete control and replication of the many complex failure processes which needed to be analyzed utilizing a unique damage model not available in commercial finite element analysis software. This modeling approach is used to simulate the standard and stiff Brazilian indirect tension tests.

Additionally, experimental work was completed to observe how the proposed stiff Brazilian indirect tension test and permeability measurement apparatus would correlate behavior of a sample which had already experienced damage from an alternative source followed by loading utilizing the Brazilian indirect tension test. A specimen with a hairline fracture induced from a drop tower impact was selected and placed in the stiff Brazilian indirect tension test apparatus and permeability set-up. This same specimen was also modeled using the FDEM platform while simulating the main line of fracture into the model. This work offers an in depth look into the analysis process necessary to correlate damage, fracture and permeability in concrete and rock using the Brazilian indirect tension test at a quasi-static loading rate.

1.2   Scope of Work

In this work a standard Brazilian indirect tension test is compared to a proposed stiff Brazilian indirect tension test using experimental data and a high intensity parallel computing finite-discrete element (FDEM) platform. The inherent difficulty in capturing the behavior of brittle and quasi-brittle damage and fractures experimentally is examined and potential solutions emerging from the proposed stiffened Brazilian apparatus are presented. The proposed stiff Brazilian aims at decreasing the load on the cracked concrete disk to slow crack propagation. This is in an effort to apprehend a clearer picture of the

failure process seen in the standard Brazilian indirect tension test. The traditionally instantaneous failure observed with the standard Brazilian indirect tension test hinders the ability to capture any meaningful changes in permeability that are potentially starting prior to sample failure. The FDEM platform used aids in developing an understanding of the damage and fracture processes existing in a quasi-brittle material like concrete under the loading conditions exhibited in the Brazilian indirect tension test at a quasi-static displacement rate. Investigation into the use of the proposed stiff Brazilian indirect tension test on a pre-damaged concrete disk is also made to enhance the understanding of the modified indirect tension test. The evaluation of a low velocity impact using a drop tower for the inducing of a variant preliminary damage on the concrete disk specimen is also made. Permeability measurements are completed in an effort to add understanding to the prevalent issues in the development of a numerical method able to evaluate damage and fracture growth in relation to permeability changes. The modeling of the stiff Brazilian indirect tension test along with the pre-damaged specimen adds valuable insight into modeling of crack growth and damage evolution and their relation to potential permeability changes in a three-dimensional model.

1.3 Outline of Work

The structure of this thesis consists of the following arrangement: Chapter 2 highlights the major contributions in the literature to the finite-discrete element method used in this study. Literature relevant to the ideas surrounding damage, the Brazilian indirect tension test and high velocity impacts on brittle materials are also discussed in Chapter 2. Chapter 3 outlines the experimental and numerical methods that were accomplished in this work. The experimental methods cover specimen preparations, a preliminary study completed on a

proposed rubber sleeve apparatus, and work done involving drop tower impacts combined with the stiff Brazilian indirect tension test and permeability measures using an apparatus developed by Rusch et. al., (2018). The numerical methods cover the modeling of a preliminary study on the effects of a rubber sleeve on the indirect tension test, experimental work completed by Rusch et. al., (2018) involving the standard Brazilian indirect tension test and the stiff Brazilian indirect tension test, and modeling specimens incorporating pre-existing damage tested in the stiff Brazilian indirect tension test. Chapter 4 presents the experimental and numerical results for the tests completed for this work as well as material characterization results. Discussion of the results are also included in Chapter 4. Chapter 5 provides conclusions from this study, the limitations of the methods used and recommendations for future work.

CHAPTER 2 | REVIEW OF THE LITERATURE

2.1   Finite-Discrete Element Hybrid Methodology

2.1.1 FDEM Development

The ability to properly model the behavior of varying rock lithologies, concrete and other similar brittle materials under various loading conditions has been a concern since the inception of finite element modeling. The inherent nature of these brittle materials poses many numerical, computational, and material challenges for the accurate and repeatable replication of their behavior within a numerical simulation. The nature of continuum mechanics used in finite element modeling utilizes idealized stiffness parameters to describe nodal and elemental responses to various loading and displacement conditions. A simple 2-D triangular element as seen in Figure 1 is described by Eq. 2-1 .
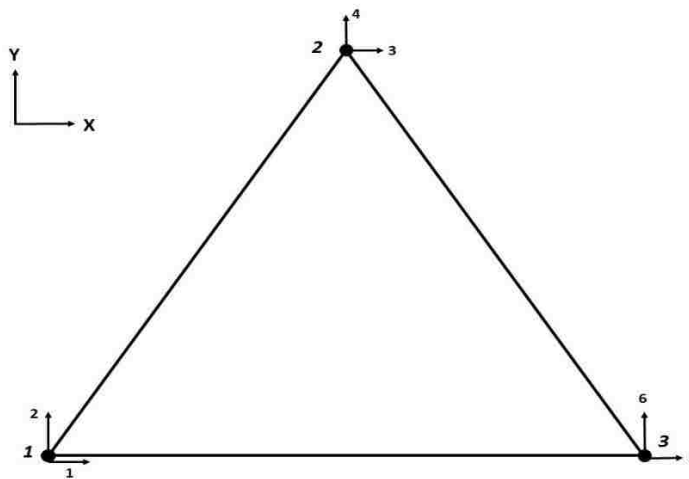
Figure 1: simple FEM three noded element with 6 degrees of freedom

Eq. 2-1
$$\{F_i\} = [K_{ij}]\{d_j\}$$

Where,

Eq. 2-2 $$\left[K_{ij}\right] = \int_A [B]^T[E][B]dA$$

Where, $\{F_i\}$ is the force vector at each node, $\{d_j\}$ is the displacement vector, and $\left[K_{ij}\right]$ is the stiffness matrix of the element. The stiffness matrix is derived by integrating $[E]$, the elastic matrix of the element, and $[B]$, the B matrix which relates strains and displacements at each node, over the area of the element, or the volume in the case of a 3D element. The basis of Eq. 2-1 is derived using kinematic relations between nodal displacements and strains, Hooke's law, and equilibrium assumptions.

The fundamental mathematics and physics principles used to derive and describe these basic components of FEM elemental behavior have initial assumptions of continuity. However, in reality no material is truly continuous at the microscopic, and atomic level. For materials with increasing heterogeneity at slightly higher levels of analysis, FEM is able to satisfactorily replicate their behavior. For brittle materials like concrete and rock, where discontinuities are much larger, these factors hinder the ability to simulate many of the common behaviors seen in experimentation. Fracture propagation and post failure strain softening behavior are fundamental components of brittle material behavior and are made intrinsically complicated when attempting to use traditional FEM assumptions.

Difficulties existing in finite-element modeling for many geotechnical applications led to the development of the distinct element method. The distinct or discrete-element method (DEM) in the geotechnical community was designed to model the interactions of granular soils and other similar particles, understanding the assumption of fundamental discontinuity present at more detailed levels in the real world. (Cundall, 1988a, 1988b;

Ishida et al., 1987). The elements are able to simulate normal force interactions, friction, and complex energy transfers between particles. (Yu, 2004). DEM has enabled the modeling of many complex geotechnical phenomena which FEM is incapable of adequately capturing due to the nature of particle interactions within a material with both elasto-plastic and fractured states. However, the inherent discretization of the elements in DEM can quickly result in large computational costs and the separation of elements make it difficult to consistently model rock formations and other materials which have an elastic state of particle cohesion.

The first combination of both types of numerical methods was made by Antonio Munjiza using C++ in 1990 and the first textbook was written on the subject and was published in 2004. (Munjiza, 2004). Figure 2 illustrates the idea behind the combination of DEM and FEM methods proposed by Munjiza. Munjiza combined the material stiffness capabilities of FEM with the particle interactions of DEM. This allowed for the ability to simulate continuum to discontuum mechanics of brittle materials and capture fracture propagation. The essential features of FDEM are the ability to capture contact detection, friction and interaction between elements, elastic deformation of combined elements, and development of damage and fractures. (World Congress on Engineering, 2016). The development of varying codes by Munjiza led to a plethora of investigations into the use of hybrid finite-discrete element (FDEM) modeling in the geotechnical world. (Munjiza and Andrews, 2000; Munjiza et al., 2000 and 2002).
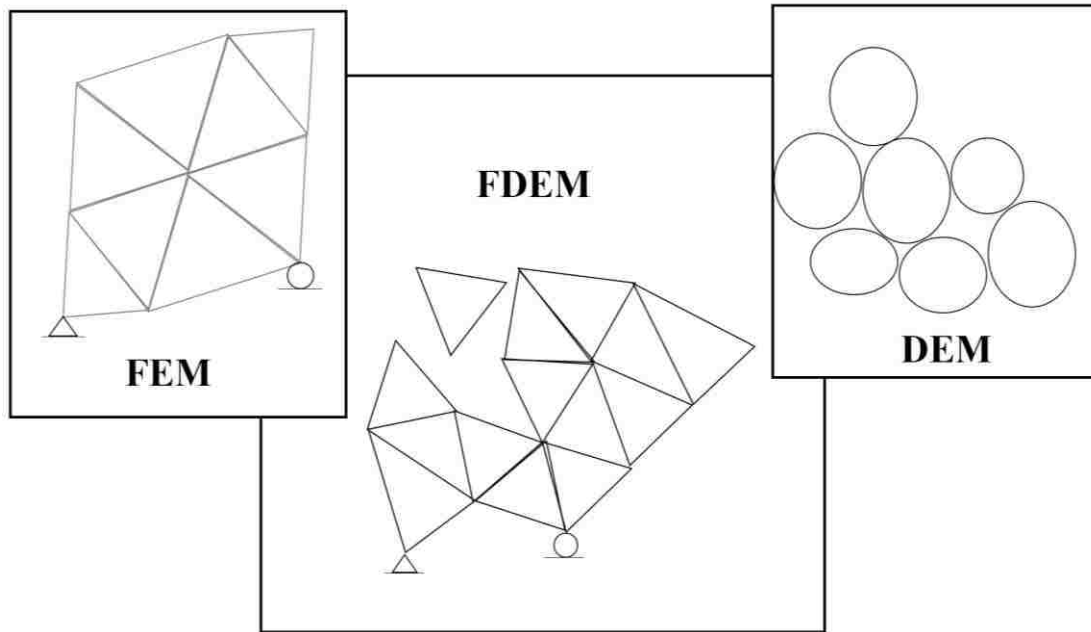
Figure 2: Summary of FDEM hybrid modeling

Supplemental work has also been done by Mahabadi et al., 2012, attempting to integrate Mohr-Coulomb failure criterion, rock joint interactions, and in-situ stresses. These investigations looked at the inherent compressibility of discrete elements and their effect on modeling the true nature of rock dynamics problems. The fundamental components of FDEM modeling, fracture propagation and strain softening are described in more detail in the following section.

2.1.2 Modeling of Fracture and Strain Softening

In the pursuit to describe fracture propagation in brittle materials like concrete and rock, many theories and models have been developed and proposed. (Bažant, 2002; Hillerborg et al., 1976; Jenq and Shah, 1985). A basic understanding of the development of fracture within concrete and brittle materials can be found in "*Fracture Mechanics of*

Concrete: Applications of Fracture Mechanics to Concrete, Rock and Other Quasi-Brittle Materials" by Shah et al., 1995. Generally, brittle materials exhibit a rather sudden drop in stress when a crucial fracture has propagated far enough throughout a specimen. (Shah et al., 1995). This failure mode can result in catastrophic outcomes in concrete structures, as well as many geotechnical structures, motivating the search to understand, design for, and model brittle material fracture.

For a single crack model, the resultant stress and strain at the tip of the crack can be described by the energy release rate G. Where $G = 2\gamma$ is the critical energy value needed to extend a crack a unit of area, with γ being the material specific surface energy. (Mustoe and Williams, 1989). The energy release rate can also be described by Irwin's formulation seen in Eq. 2-3. (Lemaitre and Chaboche, 1994)

Eq. 2-3
$$G = \frac{K_I{}^2}{E}$$

Where,

Eq. 2-4
$$K_I = \sigma\sqrt{\pi a}$$

Where, K_I is the stress intensity factor described by the crack width a and crack tip stress σ. The Dugdale model, in **Figure 3**, is a traditional single crack model for mode I fractures and aids in creating an understanding of the relationship between the critical crack opening δ_c, crack length zone Δ also known as the fracture processing zone, and the bonding resistance stress of the material, f_t.
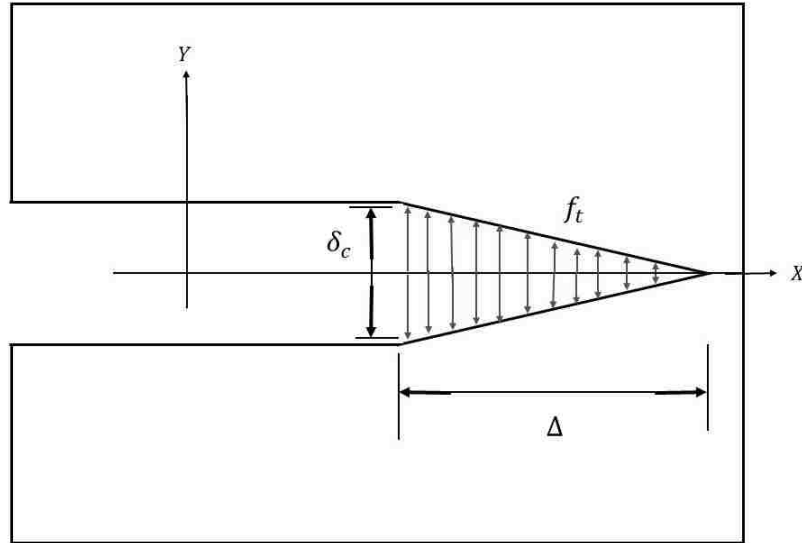
Figure 3: Dugdale Crack Model

When the crack opening is equal to δ_c the material bonding stress drops to zero. The crack length zone Δ, can be estimated by Eq. 2-5.(Munjiza et al., 1999).

Eq. 2-5
$$\Delta = \frac{\pi E \delta_c}{32 f_t}$$

With E being the Young's modulus of elasticity. It can be observed from this basic formulation that materials with high stiffness such as steel will tend to exhibit a higher fracture process zone, while materials like concrete and rock will exhibit a less substantial fracture process zone. The shape and length of this zone is critical to understanding the amount of energy dissipation that a material will display toward the growth of a fracture, or better termed the creation of new surfaces.

A crack can also be modeled and thought of as a band, rather than a single crack. This approach is known as a smeared crack model, where local strain and stresses are evaluated by constitutive laws in localized bands. (Cervera and Chiumenti, 2006). The

11

model implemented in this work utilizes a combined single and smeared crack model. The stress-strain interaction of the elements is described by a curve broken into two parts as shown in Figure 4. Part 'A' is governed by constitutive laws and finite element methodology while part 'B' is the representative strain softening modeled using a combined single smeared crack model.
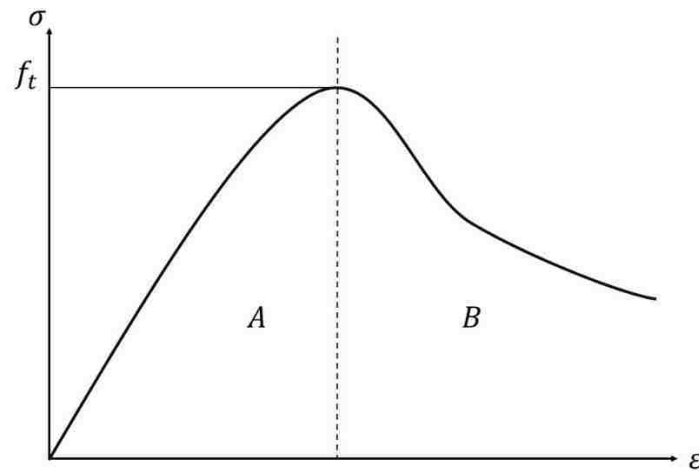
Figure 4: Elemental interaction stress-strain curve components
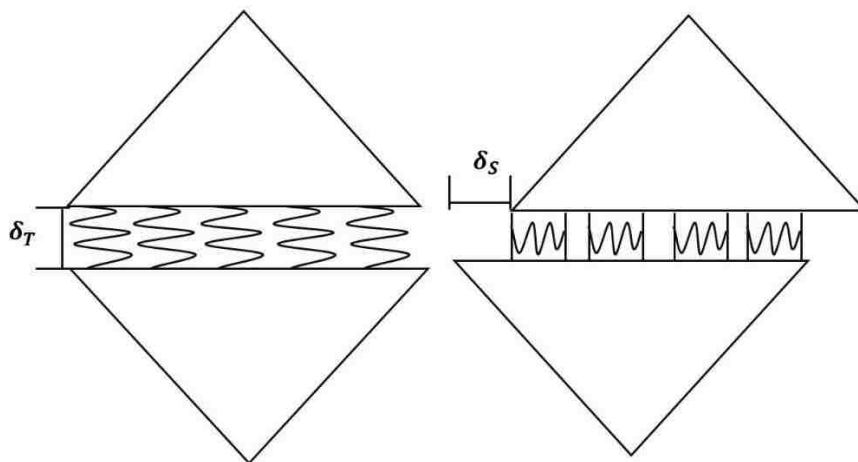
Figure 5: Representative element separations based on penalty functions

In this model cracks are assumed to occur at element boundaries where elements are represented as shown in Figure 5 for tensile and shear separations. The separation of the elements δ_T does not occur until the f_t stress is observed and is governed by Eq. 2-6. The shear separation, δ_S, is governed similarly with the use of a penalty term. (Munjiza et al., 1999).

Eq. 2-6
$$\sigma = \begin{cases} \left[2\frac{\delta}{\delta_p} - \left(\frac{\delta}{\delta_p}\right)^2\right]f_t, & if\ 0 \le \delta \le \delta_p; \\ zf_t, & if\ \delta > \delta_p; \\ 2\frac{\delta}{\delta_p}f_t, & if\ \delta < 0 \end{cases}$$

In Eq. 2-6 δ_p represents the separation where the bond stress, σ, equals the tensile strength of the material, f_t. After δ has passed this point the separation is represented by a heuristic softening parameter Z, which can be experimentally calibrated for different materials. The Z parameter is described in Eq. 2-7 and the experimentally derived values for concrete can be observed in Figure 6. (Munjiza et al., 1999).

Eq. 2-7
$$Z = \left[1 - \frac{a+b-1}{a+b}e^{\left(D\frac{a+cb}{(a+b)(1-a-b)}\right)}\right][a(1-D) + b(1-D)^c]$$

Where,

Eq. 2-8
$$D = \begin{cases} 0, & if\ \delta \le \delta_p \\ 1, & if\ \delta > \delta_c \\ \frac{\delta - \delta_p}{\delta_c - \delta_p}, & otherwise \end{cases}$$
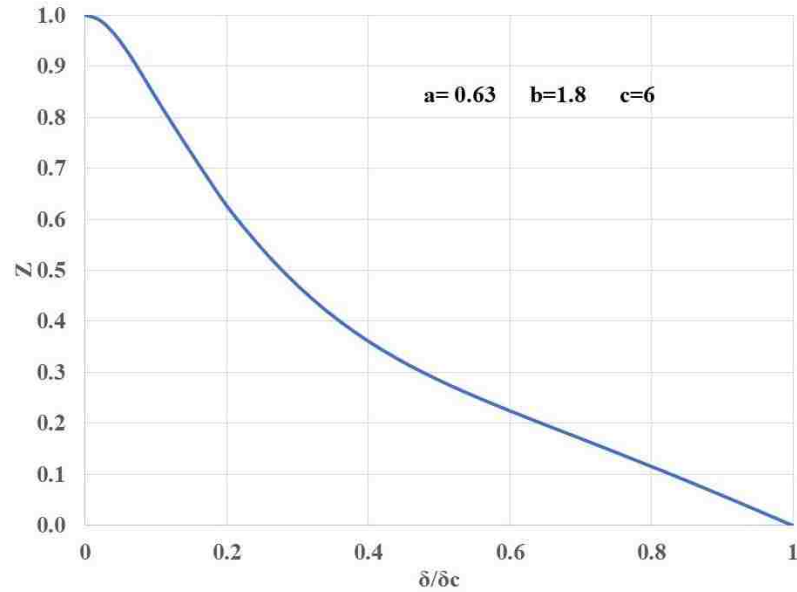
Figure 6: Heuristic softening parameter for concrete as suggested by Munjiza et al., 1999

This post-peak behavior is known as strain-softening with Z, a, b, c, δ, and δ_c described by Eq. 2-7 and Eq. 2-8. Experimentally it is an observation of a steady decrease in stress while displacement deformation continues to occur. This phenomenon was once thought of as a property inherent to the material, but has been further examined to reveal that it is a mechanism which is dependent upon several factors including specimen size, orientation, friction interactions and constituent elements. (Read and Hegemier, 1984). In the model, the heuristic curve can be calibrated for a brittle material at the elemental level and the fundamental strain-softening mechanisms inherent to that material can still be sufficiently replicated in other applications. However, the model must use a sufficient and reasonable mesh size and shapes to allow the stress fields to propagate appropriately. If an element is oriented incorrectly in the path of a crack, or if the element size is larger than the fracture processing zone Δ, the model will be unable to capture accurate crack

propagation. Because of this constraint the element size must be less than the fracture processing zone, which can again be estimated using Eq. 2-5. This combined method of fracture modeling is ideal for brittle materials, but is also applicable to ductile materials, as the fracture parameters and post-peak behaviors can be adjusted and experimentally calibrated as new materials emerge.

2.1.3 HOSS

Researchers in the geophysics group of Los Alamos National Laboratory collaborated with Antonio Munjiza to place all the relevant abilities of FDEM modeling into one cohesive package. (Munjiza, 2013). They developed MUNROU (Munjiza-Rougier), a parallel computing software specializing in continua-discontinua methods. MUNROU became the core tool to develop the uniting package which was named Hydrofrac Optimization Software Suite for its prevalence to the fracking industry, it later became Hybrid Optimization Software Suite (HOSS) as its range of applications broadened. The goal of HOSS was to develop a modeling tool which can be easily applied in a wide range of science and engineering applications, from material science to medicine, which involve varying levels of fundamental material discontinuity. Widely used applications of HOSS involve the modeling of slope stability, hydrofracture, seismic loads, glass fracture, caving, rock blasts, impacts, tunnel dynamics and more recently fluid pressure. The combined processing power available at LANL and the novelty of a cohesive platform for continua-discontinua computations have allowed HOSS to be a forerunner in the evolving world of FDEM.

2.1.4 FDEM issues and future development

One of the major issues in the development of a hybrid FDEM code is computational costs. The time needed to exhaustively calculate for all the interactions which were possible with each model becomes computationally expensive. The computational detection time was typically a $Nln(N)$ relationship, where N is the number of elements employed in any simulation. This led Munjiza to develop a no binary search (NBS) algorithm which reduced the detection time to instead be proportional to N. (Munjiza and Andrews, 1998). More complex simulations utilizing more representative elements could now be investigated in more reasonable time frames.

Additionally, Munjiza and LANL researchers improved NBS by developing MRCK (Munjiza-Rougier-Carney-Knight), a detection algorithm which breaks up the physical space into identical cells. (Munjiza and Rougier, 2010). The cells are selected so that the target points will not move more than the distance of one cell in a single time step. This arrangement allows for the parsing of the targets to only need to take place once. The sorting of the target points and their potential contacts are done using MR-Linear sort, a sorting algorithm developed by Munjiza and Rougier schematically depicted in Figure 7, making the total detection time proportional to the number of targets.

List position at time, t	Target Identifier
1	i
2	d
3	h
4	c
5	g
6	j
7	a
8	b
9	f
10	e
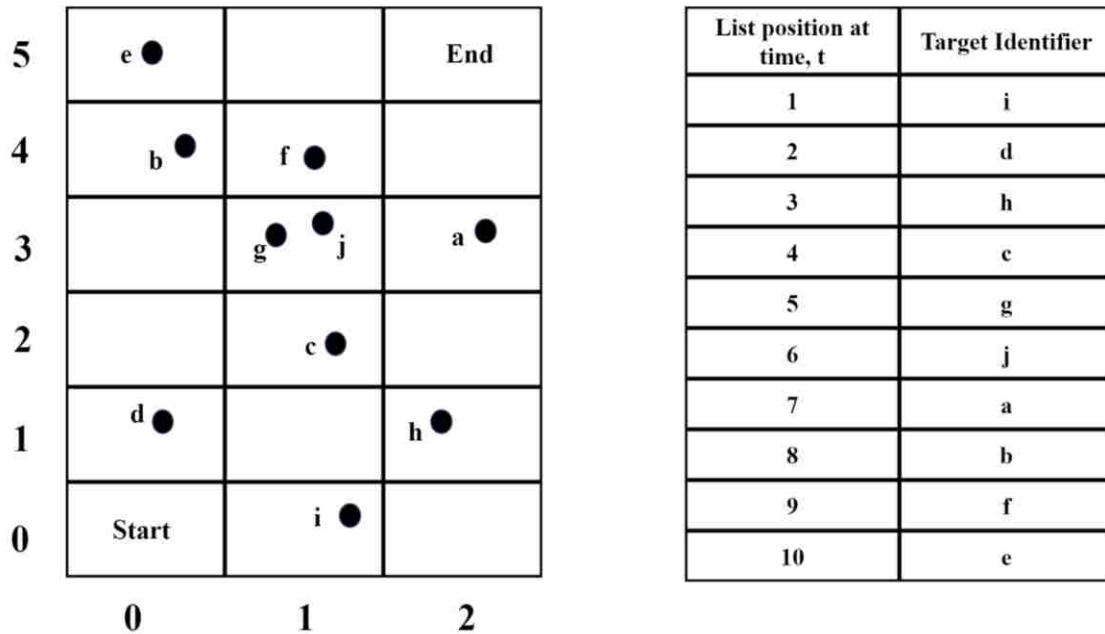
Figure 7: MR-Linear sort system mapping of target points (adapted from HOSS 2017 User Manual)

The time is further reduced by having designated contactor and target elements of any shape that can then be mapped in the modeling space and tracked. It has been found, however, that triangular shapes can more easily optimize the crack path formation and reduce mesh dependency issues, so triangular shapes are often used in FDEM. (Munjiza, 2004). The contactor element keeps the designated triangular shape and the target element is given a number of Gauss integration points dependent on the accuracy level desired, as shown in Figure 8, these points can then be integrated over to solve for the kinematic relations between each element. This system allows for the overlooking of target elements that are not within a contactor element, reducing the total number of overall calculations that need to take place.

17
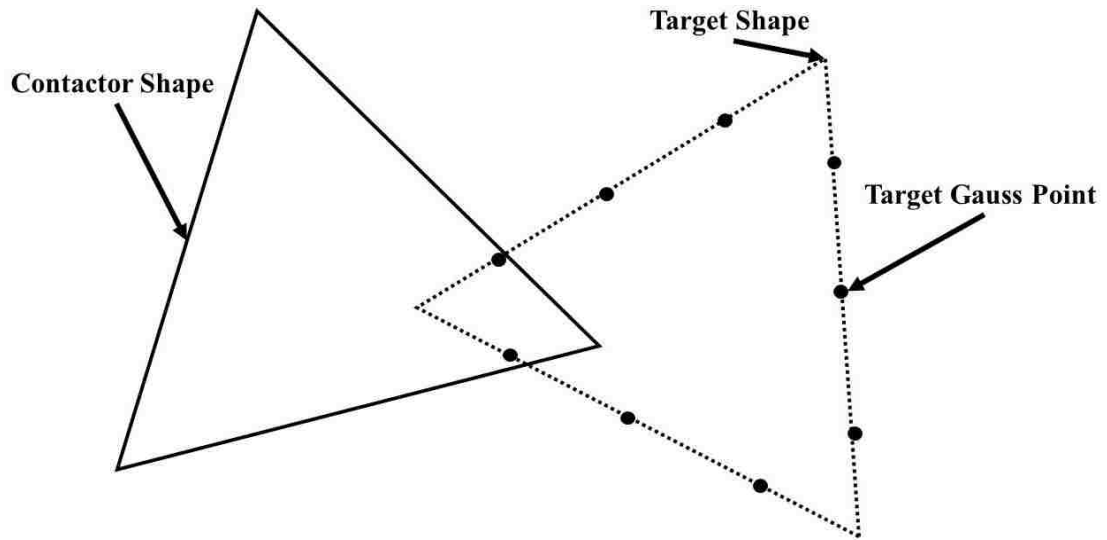
Figure 8: Interaction of contactor shape with target Gauss integration points (adapted from HOSS 2017 User Manual)

Despite these improvements the nature of FDEM modeling still requires significant computational ability and simulation time for many practical applications. However, this could be less of a concern as computational power is expected to increase rather dramatically in coming decades. Further development in FDEM methodology will include solving problems that arise with natural rock heterogeneity, mesh dependency, and the development of more material fracture models as well as investigations into fluid flow and pressure in relation to development of fractures and damage growth.

2.2   Damage in Brittle Materials

2.2.1 Damage Theory

The traditional idea of damage is usually detailed as irreparable deformation or permanent change in a material caused by internal stresses and energy losses. (Krajcinovic and Fonseka, 1981). Materials like concrete and rock are made up of existing imperfections, pre-existing micro-cracks, pore spaces, and different crystalline arrangements and interactions. The evaluation of any one point would require a substantial set of equations to determine all the respective forces and moments that could be contributing to the deformation of that point. As such, the analysis of this phenomena is largely based in thermodynamic and energy methods.

The Clausius Duhem inequality in thermodynamics dictates that the rate of energy dissipated in a given elastic material undergoing damage must be positive ($\dot{\Phi} \geq 0$), indicating that the rate of change in elastic and plastic strains must sum to be greater than 0. With damage (D) being connected to a specimen's stiffness (E), in order to fulfill the damage energy release rate, the inequality $\frac{\partial E}{\partial D} < 0,$ must be satisfied. This requires that in a generalized elastic material the stiffness of the material will decrease with increasing damage. (Mazars and Pijaudier-Cabot, 1989). This definition has allowed for the calculation of damage to take place using a method called the secant modulus method, where the damage in a given test is quantified by the change in secant stiffness, as described by in Eq. 2-9 and demonstrated by Figure 9 . (Chaboche, 1988; O'Brien, 1980; Reifsnider and Highsmith, 1982).

Eq. 2-9

$$D = 1 - \frac{E_s}{E_o}$$

Where E_0 is the initial elastic modulus, and E_s is the secant modulus at i. (Xi Yunping and Nakhi Ammar, 2005).
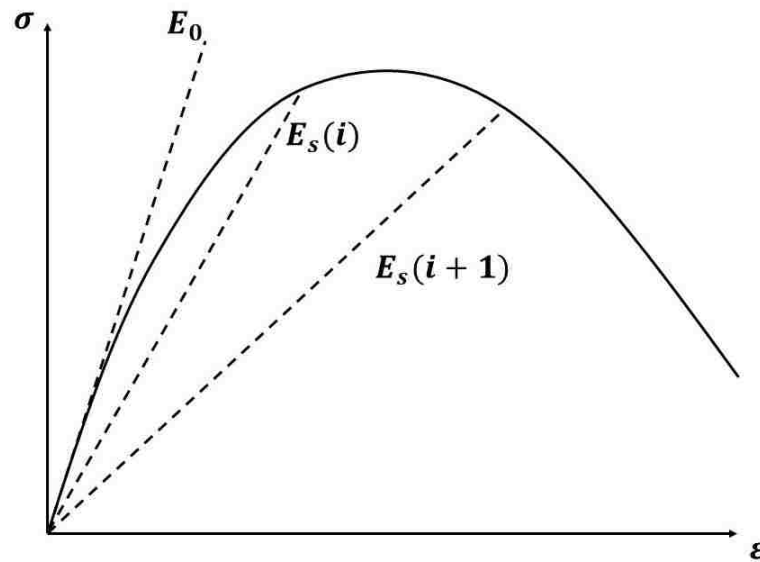
Figure 9: Secant modulus method for quantification of damage adapted from Xi Yunping and Nakhi Ammar, 2005.

In brittle materials there exists two generalized damage modes, which can be observed in Figure 10 for a standard cylindrical compression test. Type A damage consists of the opportunity for mode I, and possibly mode II, fractures leading to high strain-softening behavior as expansion of the specimen is allowed to occur. Type B consists of a more ductile failure as mode I fractures are restricted from occurring while under confinement and friction interactions of new crack surfaces begin to interact. (Mazars and Pijaudier-Cabot, 1989).
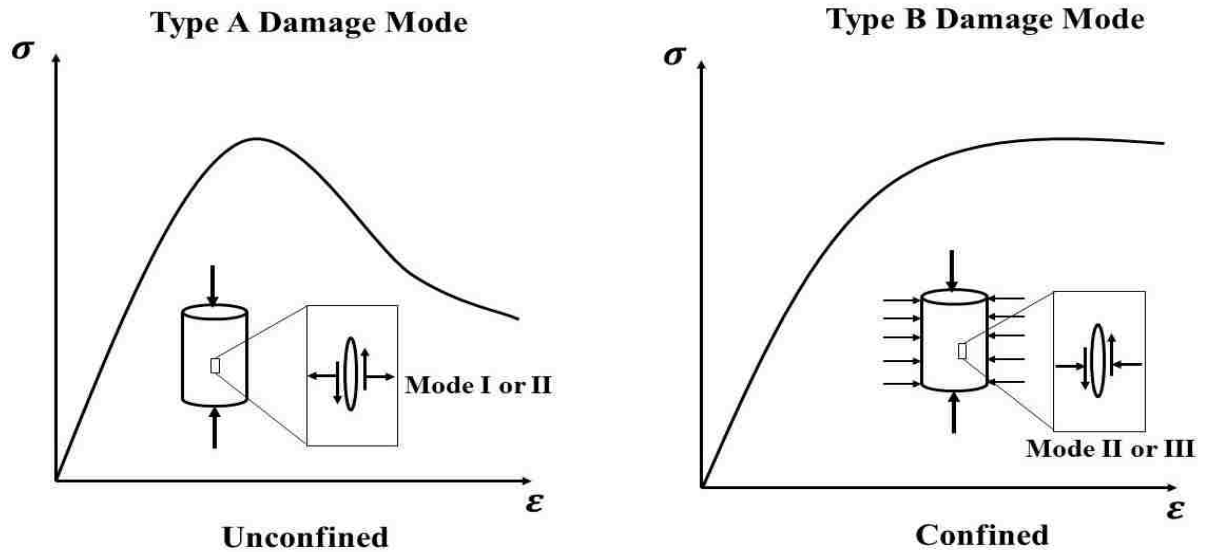
Figure 10: Generalized damage modes for brittle materials

Materials like concrete can also exhibit a third damage mode which consists mainly of the failure and consolidation of the cement matrix under heavy confinement pressures, displaying negative volumetric strains. Concrete damage is also unique in the observance that it can be understood as a composite material interaction consisting of aggregate, cement matrix, and the transition zone between the two where wall effects exist. (Maso, 1982). This zone is the weaker zone and is where damage is most likely to occur first. Figure 11 shows how the path of the fracture adjusts around the edges of the much stiffer aggregates following the arrangement of the weaker transition zones. It can be noted that in higher strength concrete the transition zone can become stronger than the stiffness of the aggregate resulting in fracture paths through the aggregate and much more brittle failures. (Yan et al., 2001). In concrete and other similar quasi-brittle materials, it is also important to note that ahead of the fracture processing zone, Δ, there is effects from microcracks which when neglected fail to capture a portion of the crack model where the bonding stress increases before dropping down to a reduced tensile strength. This phenomena results in a

21

modification to the initial assumptions made using the Dugdale model for concrete. (Shah et al., 1995).
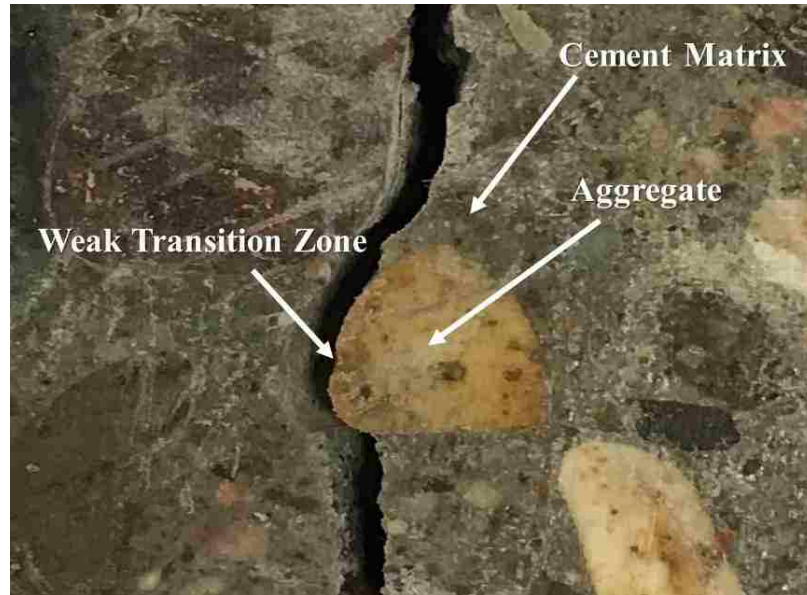
Figure 11: Components of concrete and path of fracture

Time and size effects also play an important role in the propagation of damage in brittle materials. Size effects manifest in the testing of brittle materials almost immediately and have been a huge concern in the geotechnical world for decades. (Walsh, 1976). The nature of grain sizes and mineral components of rock behave differently when existing in conjunction with more material. Stress diffusion, energy dissipation, and fracture interactions of varying size have all been shown to have an effect on the progression of damage in brittle materials. (Bažant, 2000). It has also been shown in several works that the rate of damage progression is dependent on several time related factors such as duration of stress states and strain rates used in testing. (Atkinson, 1984; Scholz, 1972). These factors need to be considered when developing experiments interested in looking at damage progression and detection.

2.2.2 Damage and fracture in Brazilian indirect tension test and drop tower impact

2.2.2.1 Brazilian indirect tension test

The Brazilian indirect tension test was developed by Carneiro and Akazawa in 1943 and is widely used in the geotechnical world to offer insight into the tensile behavior of brittle materials. (Li and Wong, 2013). The test allows for a relatively steady form of a mode I fracture and has been slightly modified by many to achieve critical fracture parameters and tensile properties of brittle materials. (Atkinson et al., 1982; Huang et al., 1996; Wang and Xing, 1999). The Brazilian disk test has also been standardized by ASTM, ISRM and others as a reliable test for retrieving tensile properties of concrete and other brittle materials. (ASTM C496, ISO 4105, BS 1881).

Conducting the standard Brazilian indirect tension test presents several issues which unnecessarily complicate the process of correlating damage and strength to apparent permeability changes. The flat plate Brazilian testing jaws have been shown by Erarslan and Williams, 2012 and others to cause issues with crushing failure and problems with central crack initiation. The assumption in the traditional analytical solution seen in Eq. 2-10 for the Brazilian disk test is that simple point loads stem from the jaws, but this is inaccurate as the load is more readily represented as a circumferential distributed load.

Eq. 2-10
$$\sigma_t = -\frac{2P}{\pi d t}$$

Where, σ_t is the tensile strength of the specimen, P is the maximum applied load, and d and t are the diameter and thickness of the specimen respectively.

Erarslan and Williams, 2012 have also shown that utilizing a loading head with an arc of 20-degrees sufficiently improves the ability to capture the indirect tensile strength and eliminates a significant amount of the problems seen when using the traditional Brazilian jaws.

The analytical solution developed by Hondros, 1959 for a distributed diametral compression load applied to a disk is used in analyzing the experimental results. The stresses within the disk can then be calculated using equations Eq. 2-11 to Eq. 2-13 and Figure 12 .
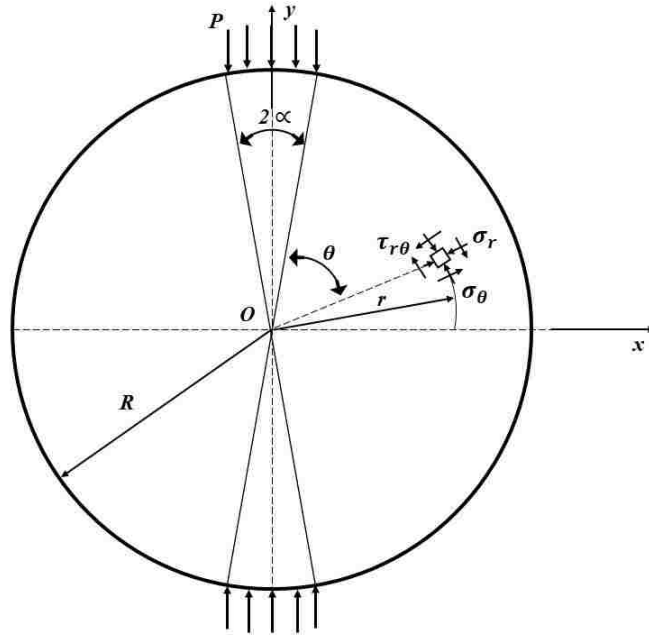
Figure 12: Analytical solution for indirect tensile strength (Hondros, 1959)

Eq. 2-11
$$\sigma_r = -\frac{2p}{\pi}\left\{\alpha + \sum_{n=1}^{n=\infty}\left[1 - \left(1 - \frac{1}{n}\right)\rho^2\right]\rho^{2n-2}sin2n\alpha cos2n\theta\right\}$$

Eq. 2-12
$$\sigma_\theta = -\frac{2p}{\pi}\left\{\alpha - \sum_{n=1}^{n=\infty}\left[1 - \left(1 + \frac{1}{n}\right)\rho^2\right]\rho^{2n-2}sin2n\alpha cos2n\theta\right\}$$

Eq. 2-13
$$\tau_{r\theta} = -\frac{2p}{\pi}\left\{\sum_{n=1}^{n=\infty}[1-\rho^2]\rho^{2n-2}\sin 2n\alpha \cos 2n\theta\right\}$$

Where p is the applied circumferential pressure, $\rho = r/R$, R is the radius of the disk, r and θ represent a point on the disk in polar coordinates and α is the half central angle of the distributed load. The negative sign is used to indicate that the generated stresses, $\boldsymbol{\sigma_r}$ and $\boldsymbol{\sigma_\theta}$, are in opposite directions to the applied stress p.

Despite some difficulties in the analysis of stresses in the disk, the Brazilian indirect tension test is still one of the most reliable and accessible tests to determining the tensile strength of brittle materials. (Zdenek et al., 1991).

2.2.2.2 Damage using localized high strain impact

A very limited amount of exploration has been made into the inducing of damage in brittle materials from low velocity impacts. When a brittle material is impacted with a mass at low velocity in a small region with sufficient thickness, the resultant damage induced is mainly facial, resulting in the formation of an impact depression where the material has been pulverized. The nuances of damage propagation and resultant crater formation have been explained by Evans et al., (1978) and were shown to have most of the energy absorbed through the creation of the impact craters when the impact is concentrated in a small area of a sufficiently thick and wide sample. When the threshold for the formation of damage has occurred cracks will occur radially in the directions of minimum potential energy, which are governed by material thickness, stiffnesses, faults and other barriers. Bowden and Field, (1964) also showed that the modes of fracture induced from an impact are dependent upon the shape and duration of the stress pulses and that the tensile stresses behind the Rayleigh wave front are mainly responsible for the formation of cracks.

Fracture toughness, elastic wave velocity and the distribution of surface cracks and imperfections were shown by Evans et al., 1980 to play a major role in the initiation of subsonic damage. The size and velocity of the impact projectile also clearly influence the initiation of damage. Most of the tests conducted by Evans et al.,1980 however were completed on specimens with a diameter at least 50 times greater than the impact diameter, to avoid complications from stress waves reflecting off sample boundaries.

The focus of the term damage in this work refers to the permanent change in a material due to internal stresses and strains. The Brazilian indirect tension test and drop tower impacts of concrete disks both consist of tensile failure mechanisms but have different modes of damage creation. In the Brazilian indirect tension test brittle materials are subject to stresses inducing mode I fractures, cracks develop from the creation of new surfaces stemming from stresses developing at edges of already existing microcracks and imperfections. Internal networks of microcracks can be interpreted according to the Griffith model as seen in Figure 13. Ellipses with a minor to major axis ratio approaching zero represent the existing cracks and describe the development of edge stresses, σ_G, as the minor axis of the ellipse lines up with the maximum stress. (Griffith, 1924). These fundamental cracks can coalesce at increasing levels of analysis and can constitute damage in the material. For concrete the Griffith model can only be used as an interpretative framework, as the Griffith model was developed for highly homogeneous brittle materials like glass.

$$\frac{a}{b} \cong 0$$
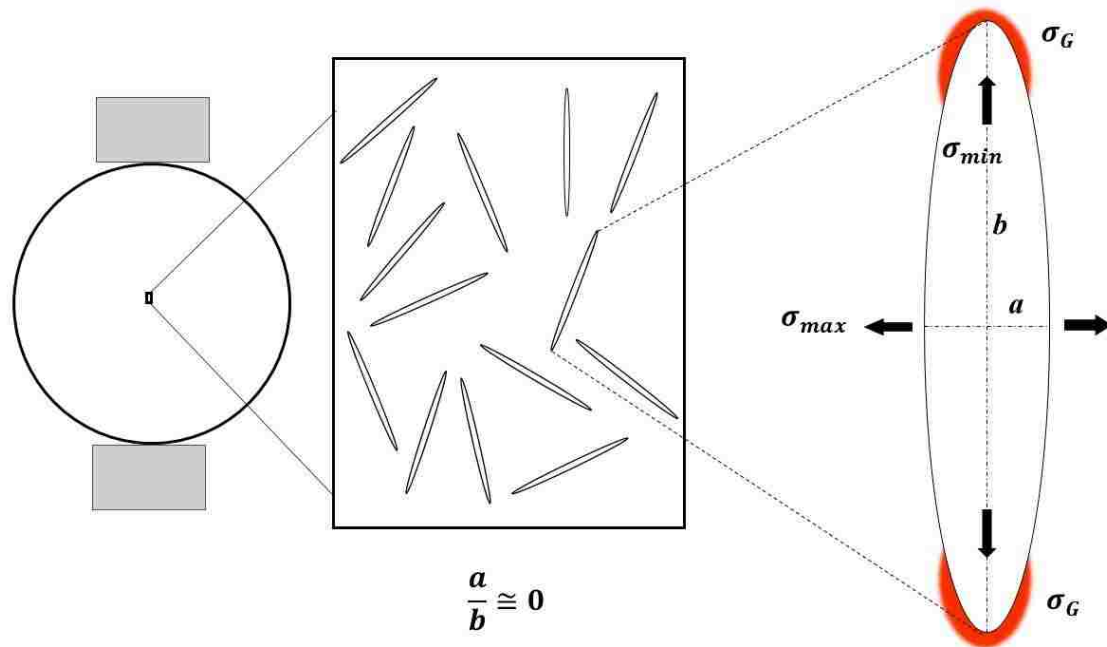
Figure 13: Griffith theory model of elliptical microcracks

In the high strain impact a localized area of damage occurs consisting of pulverized material and induced microcracks below the impact crater. This can lead to full hairline fractures if the energy of the impact is high enough and the respective material is weak enough. These two different methods illustrate that damage differs from one domain to another.

2.2.3 Damage Detection and Methods

The subtle changes that occur in brittle materials before failure can be detected by several methods that have been developed in different fields. Work done by Dai and Labuz, 1997; Holcomb and Costin, 1986; Landis and Baillon, 2002; Lockner, 1993 showed the reliability of acoustic emissions (AE) to capture the rapid release of strain energy present when damage occurs. Abeele et al., (2000) among others showed the use of nonlinear elastic wave spectroscopy (NEWS) to detect damage through changes in a materials fundamental

modes. Boller, (2000) also revealed that brittle damage on aircraft can be reasonably detected using piezoelectric sensors. These methods are all designed to detect damage in different types of materials and different resolutions. For this study concerned with potential permeability correlations, the following section describes the work related to damage detection and permeability.

2.2.3.1 Damage & Permeability

The growth and coalescence of microcracks in a brittle material has the potential to allow for the creation of paths of flow to be generated between cracked planes. Many researchers have attempted to relate permeability and damage growth using triaxial testing conditions. Homand-Etienne et al., (1998) and Souley et al., (2001) created models detailing the growth of crack lengths using permeability measurements in two different types of granite rock. A model correlating permeability to compressive stress induced fractures was also developed by Shao et al., (2005). Work done by Brace et al., (1968) showed the utility of a pressure pulse build-up test to measure permeability in Westerly granite. Others also used a pressure gradient and found that after being loaded from 75% to 95% of its ultimate capacity the permeability of Westerly granite increased 2 to 4 times its original value. (Zoback and Byerlee, 1975). It has also been found that confining pressure plays a large role in the resultant permeability that will be measured from a damaging specimen, as others have found the permeability change to be 3 to 4 orders of magnitude higher in other types of granite. ((Oda et al., 2002). Some of the first work on micromechanical analysis of microcracks was completed by Jiang et al., (2010), where they considered that the permeability in a triaxial compression test is affected by frictional sliding and roughness

of the crack surfaces. Others have noted that pore size distributions also affect permeability.

(Arson and Pereira, 2012).

An appropriate model attempting to capture permeability changes in materials like concrete and rock needs to account for initial matrix porosities, damage initiation effects, crack formations, crack growths, crack dilatancy and crack densities. For the early initiation of fractures in the Brazilian indirect tension test being used in this study it may be valuable to use the theories developed by Lomize, (1951). He used parallel glass plates to validate a theory that would become known as the cubic law. A simplified form of the cubic law, which relates crack width and permeability is presented in Eq. 2-1. Zhang, (2016) was able to show that the cubic law could be used effectively to capture post-peak permeability behavior in clay rocks undergoing excavations. This law is used in experimental work by Rusch et. al. (2018) to compile relevant work for the creation of FDEM model capabilities for the incorporation of the complexities of flow between cracks, we suggest this formula can be used as a good starting point for correlating permeability and fracture growth in the Brazilian indirect tension test.

Eq. 2-1 $$k = \frac{b^2}{12}$$

2.2.4 Damage in FDEM modeling

Modeling the separation of inherent discontinuities in nature is highly complicated as explained in section 2.2.1, making FDEM an ideal avenue to advance the nuances of modeling and understanding material damage progression. The FDEM code used in this study defines damage as a ratio of the separation between elements and the maximum

fracture aperture, δ_c as shown in Eq. 2-14 and Figure 14. As explained in section 2.2.1 the fracture processing zone is controlled by the heuristic parameters defined by Eq. 2-7 and determined using experimental methods. The evolution of damage in the model is therefore dependent upon the material softening calibration, mesh size, the calculated maximum fracture aperture, and the tensile and shear strength definitions of the material.
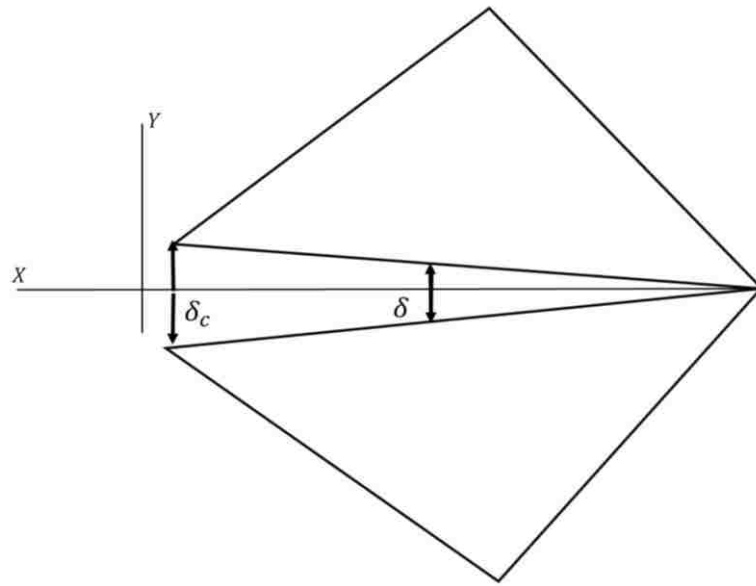
Figure 14: Numerical damage expressed as ratio of displacements between tetrahedral elements

Eq. 2-14
$$D = \frac{\delta}{\delta_c}$$

In order to obtain the maximum fracture aperture for tensile and shear separations Eq. 2-15 and Eq. 2-16 are used

Eq. 2-15
$$\delta_T = \frac{G_I}{f_t A_0}$$

Eq. 2-16
$$\delta_S = \frac{G_{II}}{f_s A_0}$$

Where,

Eq. 2-17
$$A_0 = \int_0^1 Z(x)\, dx; \quad x = \frac{\delta}{\delta_c}$$

$Z(x)$ is the heuristic softening curve and A_0 is the area of the normalized curve for the specific material model calibration. G_I, G_{II} are the specific energies per unit area for mode I and mode II separations, f_t, f_s are the tensile and shear strengths of the material and δ_T, δ_S are the resultant maximum separation values for tensile and shear respectively. (Osthus et al., 2018).

This numerical method allows for the observance of types of numerical damage that are occurring within the model. A fully tensile separation is represented by a factor of 1, while a 0 represents a full shear separation. Combined tensile shear separations are represented by a factor between 0 and 1, and are weighted according to the respective prevalence of the type of separation present.

CHAPTER 3 | METHODS

3.1 Experimental Methods

3.1.1 Materials

The specimens used in the experimentation for this work were all completed using standard ASTM testing method C469. Two main concrete specimen types were created: fine aggregate and coarse aggregate. For the finer aggregate specimens, the concrete was placed in 2" by 4" cylindrical molds, and for the coarser aggregate concrete was placed in 4" by 8" cylindrical molds. All of the samples were cured for 7 days in a hot water bath at a temperature of 50-degrees Celsius. The cylinders were then sliced into disk pieces using a stone cutter and were tested for material properties at 28 days of age. The thickness of the samples was test dependent but ranged from 1" to 2".

The Young's Modulus of elasticity for the specimens were calculated from the results of 5 experimental unconfined compression tests. The tests were conducted according to ASTM C469 and a displacement-controlled rate of 1mm/min was used. The resultant Young's Modulus was calculated using the average values from the 5 tests and Eq. 3-1, from ACI 318-08.

Eq. 3-1
$$E_c = 0.043 w_c^{1.5} \sqrt{f'_c}$$

Where, w_c is the density of the concrete and f'_c is the characteristic compressive strength.

For the disks used in the investigation into the rubber sleeve the cylinders were cut into 25.4 mm disks and tested after 28 days of age. For the sleeved specimens the rubber was molded around the steel loading heads and disks leaving a slight overhang of 18.5 mm of

rubber on one face for the attachment of a hose apparatus. The rubber is made of a two-part mixture used in industrial and casting applications. The mixture cures at room temperature into a urethane rubber having excellent dimensional stability and sufficient flexibility. The cured rubber sleeve has a thickness of 6.35 mm.

3.1.2 Preliminary Investigation: Use of a PMC rubber sleeve

A flexible urethane rubber sleeve was placed around the circumference of a concrete disk as shown in Figure 15. Several tests were conducted to investigate the behavior of the concrete disk specimens with and without a urethane rubber sleeve to understand the impact of the sleeve on the behavior of concrete subjected to indirect tensile testing.

Figure 15: Indirect tension with rubber sleeve

Ten sleeved and ten un-sleeved disk specimens having a diameter of 50.8 mm and a thickness of 25.4 mm were tested. The disk specimens used were of the finer aggregate

concrete type and prepared according to section 3.1.1. For both the sleeved and un-sleeved specimens the steel loading heads are in direct contact with the concrete specimen. The indirect tension tests were conducted with an Instron frame using a displacement-controlled loading with a rate of 0.25 mm/min.

3.1.3 Digital Image Correlation (DIC)

In order to achieve the more accurate displacement measurements from the Brazilian indirect tension tests, Digital Image Correlation (DIC) was used. The tests are recorded with a suitable high-quality image camera as shown in Figure 19. The images are then processed in a software called GOM Correlate, which is able to discretize the pixels of the images and track their movement from image to image given a measurement datum. Specimens are given a stochastic pattern as seen in Figure 16 to help create contrast between groups of pixels for the correlation process.

Figure 16: Specimen with stochastic pattern used for DIC

Using the DIC allows the tests to better capture the true deformation of the disk samples in both the vertical and lateral directions. Other methods, such as LVDT measures and strain gauges, proved too invasive and cumbersome to be used in the experimental set-up used.

3.1.4 Stiff Brazilian Indirect Tension Test Set-Up with Permeability Measures

To better capture the pre-peak accumulation of damage in concrete during the Brazilian indirect tension test and to allow for slower loading of the cracked concrete specimen a stiffness apparatus was constructed. The modified test is named here as the stiff Brazilian indirect tension test. The modified test is inspired by work done by Lenke and Gerstle, (2001), where a direct tension test of concrete was modified to observe crack propagation of concrete in direct tension by introducing steel rods to absorb more of the tension load when the concrete cylinder cracks. The proposed apparatus used in this work is modified to control compression in the Brazilian indirect tension test. The theory behind the modified test consists of treating the concrete disk and additional supports, represented by PVC pipes, as springs as shown in Figure 17. The support springs are then designed using Eq. 3-2 to Eq. 3-6 with an appropriate stiffness to absorb more load as the stiffness of the concrete specimen decreases with increasing damage as can be observed in the graph in Figure 18. This system allows for the near peak and post-peak regions of the test to be slowed down for observation and analysis.

Eq. 3-2
$$K = \frac{AE}{L}$$

Eq. 3-3
$$P = P_c + 2P_s$$

35

Eq. 3-4 $$P_s = K_s d_s$$

Eq. 3-5 $$P_c = K_c d_c$$

Eq. 3-6 $$d_s = d_c$$
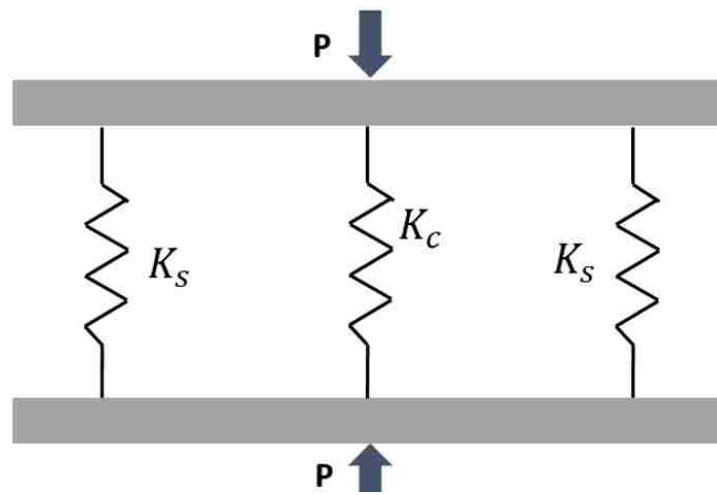
Figure 17: Spring depiction of modified Brazilian indirect tension test Rusch et. al., (2018)
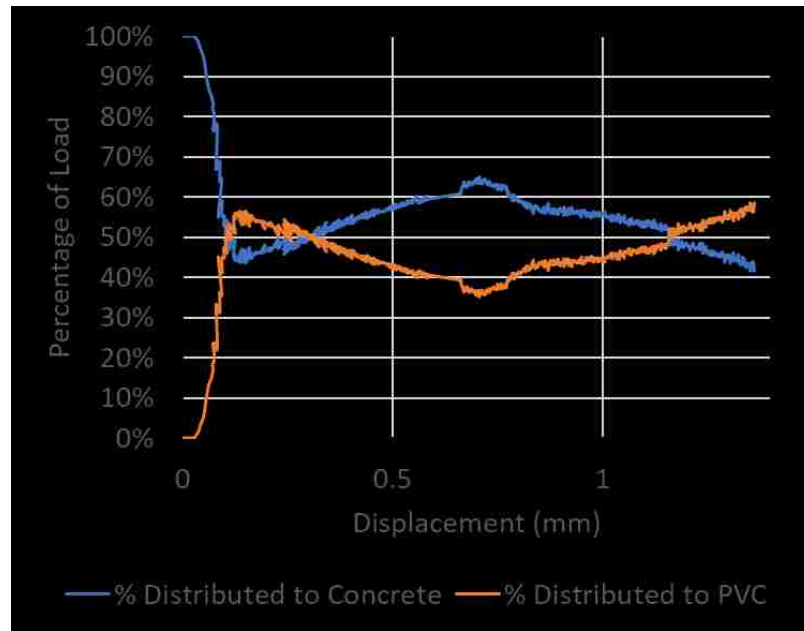
Figure 18: Stiff Brazilian indirect tension test load share principle (Rusch et. al, 2018)

This set-up has also been fitted to be used in conjunction with an apparent permeability apparatus developed by Rusch et. al. (2018). One face of the disk specimen is attached to a hose funnel and vacuum system as shown in Figure 19, while the other remains exposed to atmospheric air. The permeability is then determined through a series of flow meters, a differential pressure gauge, and volumetric tanks using principles of Darcy's law. The hope of this set-up is to measure the permeability of the concrete specimen as the stress level grows. The apparent permeability set-up and measuring system is described in Figure 20.
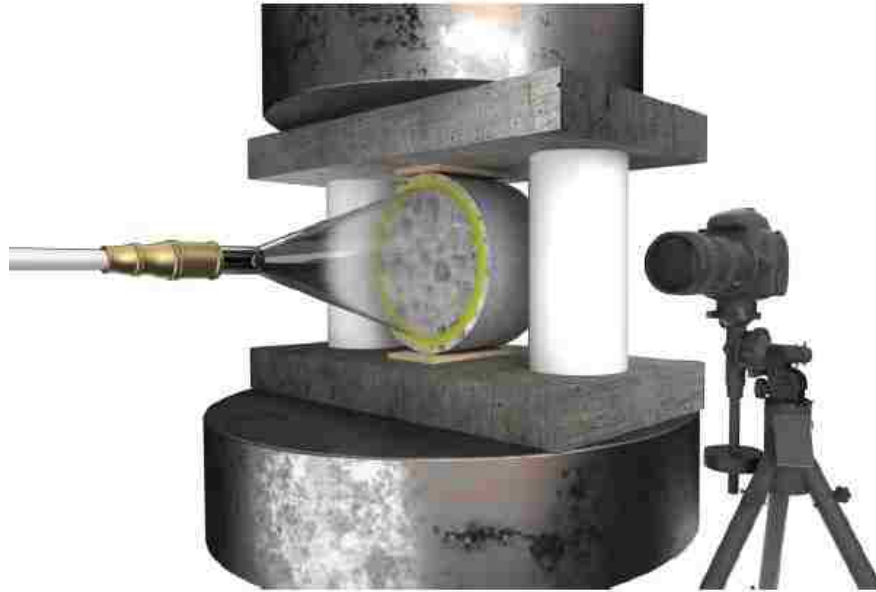
Figure 19: Stiff Brazilian indirect tension test with permeability measurements
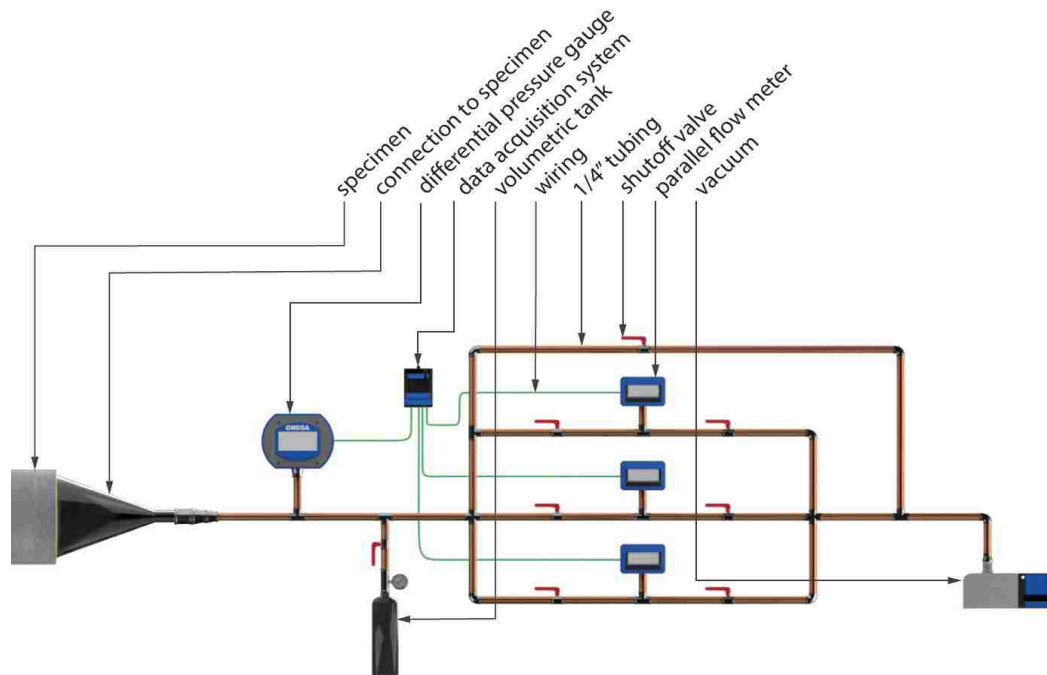
Figure 20: Permeability Apparatus Diagram

3.1.4.1 Stiff Brazilian Indirect Tension Test Procedure

The preparation of the concrete disks for these tests is described in section 3.1.1. The testing

of samples with the stiff Brazilian indirect tension test with permeability measurements to

be compared with the FDEM model are conducted according to the following procedure:

1. The disk specimen carefully has AT-200Y vacuum tape pressed around the circumference of one face, ensuring aggregate voids and notches on the edge are sufficiently covered or avoided.

2. The funnel of the apparent permeability measurement system is then carefully placed and pressed atop the AT-200Y vacuum tape.

3. The specimen is then carefully adjusted in the stiffness apparatus. The disk should be centered between the PVC pipes and centered in the middle of the plates, with the steel plates touching both PVC pipes and the disk specimen using thin strips of wood as necessary.

4. Once the disk is aligned properly and is restrained from twisting, the vacuum system can be turned on. The pressure gauge and funnel should be checked for any issues stemming from the taping of the funnel to the face as the negative pressure is allowed to build.

5. The camera and lighting for the DIC is set-up ensuring a level is used to keep camera parallel to specimen and stiffness apparatus and reducing any pivot angles of the camera's viewing angle.

6. The loading frame procedure is then specified, for these tests a load rate of 100N/s was used up to about 60% of expected maximum load, followed by a displacement-

control rate of 0.05mm/min. For tests with an existing hairline fracture only the displacement-control test protocol was used.

7. The DAQ systems for the flow meters and pressure gauges are set to record and an initial pressure drop is applied with a volumetric tank to later calculate the initial permeability of the specimen.

8. The test is then started, ensuring the camera is recording, taking note of the time of each data acquisition mechanism in relation to the others for use later in analysis.

9. Pressure drops are then conducted every 1.5-2 minutes for about 45 seconds to observe small changes in permeability.

10. Once the pressure drops past a critical value the system should be quickly switched to allow flow through the small, medium, and large flow meters.

11. The test is concluded when either the pressure and flows have equilibrated, or the displacement of interest has been reached.

3.1.5 Damage induced by low velocity impact

The investigation of pre-damaged specimens in a direction that is orthogonal to the load path of the Brazilian indirect tension test is of interest to simulate cases where damage from high-strain loads may occur. This damage scenario can be seen in many rock engineering applications where brittle materials are subject to impacts in directions perpendicular to in-situ stresses. To pre-damage concrete disk specimens an instrumented drop tower with a piezoelectric sensor impact rod as shown in Figure 21 was used. The specimens used in this study were impacted with a spherical rod that is about 8 times smaller than their diameter, clearly allowing for the effects of stress, damage, and energy waves to complicate

the analysis of the resultant impact damage, thus this method is only being used as a calibrated way to observe a pre-damaged disk specimen.
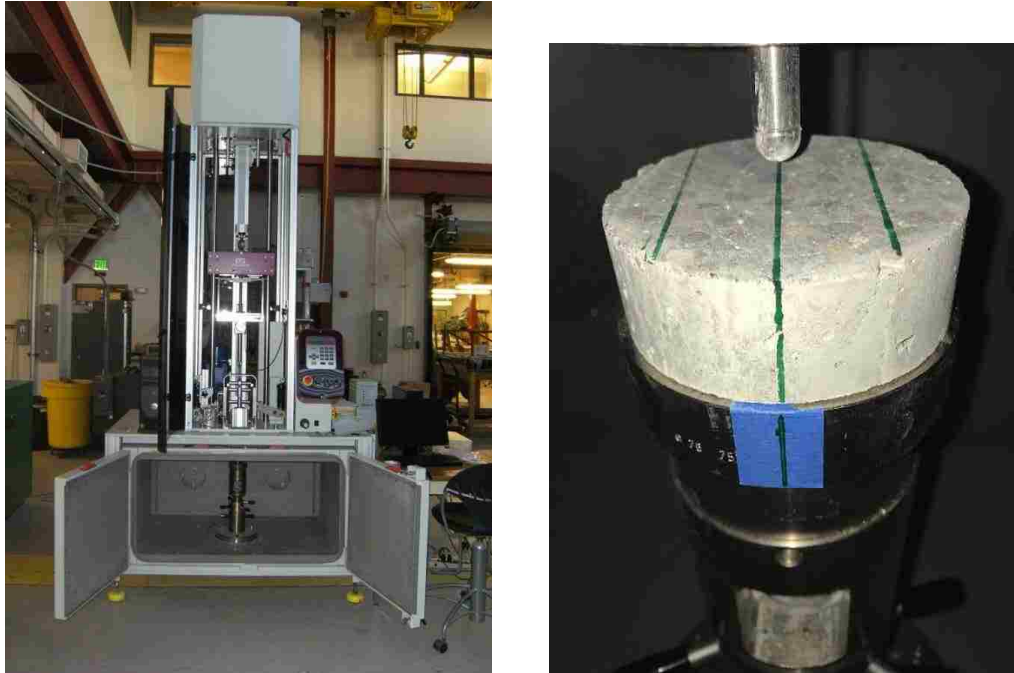
Figure 21: Impact Tower and rod sensor

As mentioned in section 2.2.3.2 the fracture paths of such an impact occur radially and follow paths of minimum potential energy, mostly due to variations in thickness and aggregate stiffnesses. As such, with concurrent results from initial impact investigations shown in section 4.2.2 , the set-up was modified with a restraint on the specimen as shown in Figure 22 to create a line of minimum potential energy, which can then later be used to orient the specimen in the indirect tension set-up for comparison. The line of minimum potential is created by restraining movement in one direction, forcing the tensile stresses induced from the impact to act along a single line.

Figure 22: Bar clamp for restraint of minimum potential line

The drop height of the mass was carefully calibrated to achieve minimal, yet substantive, damage in the samples. The use of specimens with a larger area results in a more successful sample size, as more energy is required to propagate the fractures fully, as inherently each specimen requires a unique amount of energy to initiate this critical amount of damage. Thus, samples with hairline fractures were able to be established. These samples were then taken through the procedure outlined in section 3.1.4.1 for comparison.

3.1.5.1 Dynamic Impact Procedure

Due to the nature of the high variability inherent in concrete and brittle materials, a large sample size of disk specimens were used to ensure several good specimens were available to go through the stiffness set-up and apparent permeability apparatus. The specimens were prepared as described in section 3.1.1 and were handled in accordance with the procedure below:

42

1. Specimens with the least amount of variation in thickness should be chosen, as it affects the final path of the fracture or internal damage. Thus, the dimensions of the sample are to be critically evaluated before the start of the test.

2. Using the apparent permeability measurement system, measure the permeability of the specimen before impact.

3. Chosen specimens are then carefully placed in the bar clamp, with the specimen being centered in between the clamping heads, the clamp is engaged to restrain the movement in that direction.

4. Carefully mark along the diameter line which is engaged with the clamps using a straight edge.

5. Place the specimen with the bar clamp in the chamber of the impact tower, using a system which supports the weight of the bar clamp as the specimen sits centered on the support of the impact tower.

6. Align the top face of the specimen with the datum of the impact rod, carefully ensuring the weight of the bar clamp is still supported by the chosen system and not affecting the movement of the specimen except as a restraint.

7. Close the impact tower doors and engage the machine by specifying the desired mass and drop height. A mass of 5.246 kg and a drop height of 250mm-260mm was used in these tests.

8. After impact retrieve specimen, disengage bar clamp and observe if there are any visible fractures.

9. If specimen has desired level of damage, based on visible fractures and apparent permeability measures, continue with the procedure outlined in section 3.1.4.1.

3.2 Numerical Methods

3.2.1 Geometry and Mesh

The geometry and mesh for each model were completed using Trelis version 16.4. Trelis is a pre-processor developed by Csimsoft and Sandia National Laboratory to tackle complex modeling problems, see Figure 23. A script for each model was created, with respective dynamic variable dimensions, to ease replicability and account for possible changes in dimensions.
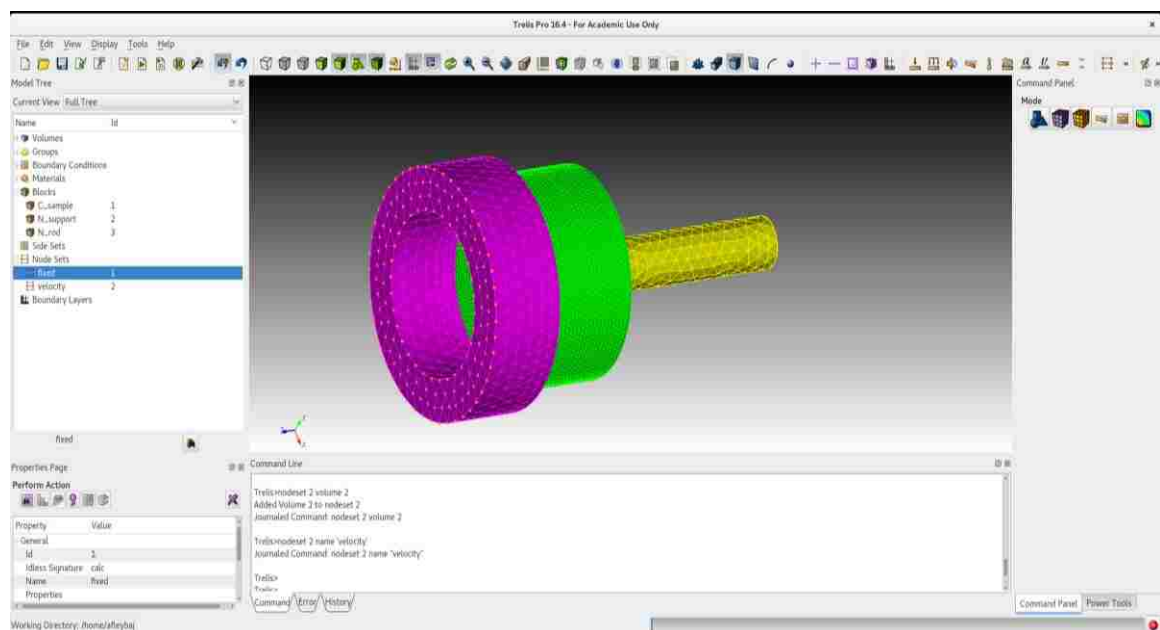
Figure 23: Trelis meshing software

In Trelis the material blocks and node sets are also designated and named within the model.

- Material blocks: Assigned to specified elements within geometric bodies of choice to later assign respective material properties.

- Node sets: groups of nodes which can be given different initial and boundary conditions and can be assigned to a single node, curves, surfaces, or volumes

44

Mesh size and scheme for each geometric body within the model are chosen to optimize replication and reduce computational power needed. As dictated by the solvers used in HOSS, the element shapes for all models are tetrahedrons, where the number of cohesion points per face can be specified depending on desired accuracy and objectives. After the geometry, mesh, blocks, and node sets have been created and verified the geometry and mesh are then exported into the common Abaqus '.inp' file format.

It is important to mention here that the solver within HOSS identifies material blocks named with a precursor "C" for cohesion (ie: "C_sample"), as blocks that can fracture. If the material block is given a name with any other letter (ie: "N_sample") the HOSS solver will treat the block as a pure FEM component.

3.2.2 Material Definition

3.2.2.1 Elastic-Plastic Properties

Defining the properties of each material is done according to theory developed by Munjiza et al., 2015 in *Large Strain Finite Element Method: A Practical Course*. Material property constants based on Munjiza constitutive laws are used to describe the relationship between stresses and strains within each element. These material properties are calculated in a script using Eq. 3-7 to Eq. 3-12.

$$\text{Eq. 3-7} \quad M_V = \frac{vE}{(1-v^2)}$$

$$\text{Eq. 3-8} \quad M_i = \frac{E}{(1+v)}$$

$$\text{Eq. 3-9} \quad M_{ij} = \frac{E}{(1+v)}$$

$$\text{Eq. 3-10} \quad m_V = 2h\sqrt{\rho M_V}$$

$$\text{Eq. 3-11} \quad m_i = 2h\sqrt{\rho M_i}$$

$$\text{Eq. 3-12} \quad m_{ij} = 2h\sqrt{\rho M_{ij}}$$

Where, M_V, M_i, and M_{ij} are the volumetric, orthogonal, and parallel Munjiza constants in the ith and jth directions, m_V, m_{ij}, and m_{ij} are the Munjiza viscosities, E is the Young's modulus, v is poisson's ratio, ρ is material density and h is the characteristic elemental length of the model, which is the characteristic length of the smallest element.

3.2.2.2 Material Interaction & Cohesion Properties

Material interactions in HOSS are defined in a script section called a <dyncell>. The contact, friction, and cohesion between two bodies are first designated to be considered in the model through an if statement. The essential parameters for each interaction that need to be defined in the model are detailed in the script and explained in Table 1.

Table 1: Material interaction parameters

Cell size (C)	Size of grid, critical to computation time $\approx 0.2h$ Where h is the characteristic length
Buffer zone	Buffer of grid cells $\approx 0.1C$
Points per face min	# of minimum cohesion points between elements
Coulomb friction (μ)	The coefficient of friction that exists between the two materials
Tensile & shear strengths (γ_T, γ_V)	The tensile and shear strengths of the cohesive bond
Young Modulus cohesion	The elastic behavior of the cohesion $\approx 100E$
Penalty	The penalty value for use in determination of element embedment repulsion $\approx 100E$
Maximum normal & shear displacement (δ_T, δ_S)	The maximum fracture aperture
Strength factors	The detailing of the heuristic softening curve within the model with a, b and c values

Bodies that are going to act as an FDEM solid require their own <dyncell> to define how the model should treat the body once elements have separated, with the cohesion being of critical importance. The strain softening portion of the model and fracture parameter are input here and are described in more detail in the literature review. Using Eq. 2-15 and Eq. 2-16 and substituting in the factors of the material determined through experimental methods, the maximum fracture aperture in tension and shear (δ_c) are calculated.

The specific surface energy for brittle rock and concrete can be experimentally determined through various methods. (Hillerborg et al., 1976). Wittmann et al., 2010 discuss several of the major concerns in retrieving specific energy values for concrete fracture growth. These include availability of tension testing capabilities and variations of the values due to

relative humidity values, where a wet concrete has a lower specific energy and a dry concrete has a higher specific energy value. The values for G_I and G_{II} are assumed to be 110 J/m^2 and 128 J/m^2 respectively from the work done by Wittmann et al., 2010. Additionally, $A_0 = 0.26$ for the concrete curve developed by Munjiza et al., 1999.

For each defined <dyncell>, HOSS outputs a file which records the force interactions between the two materials at each time step, this is very useful for many of the typical experiments which require force data.

3.2.3 Model Parameters & Boundary Conditions

The problem statement of the model is defined with the title of the model, its description, and several parameters dealing with the duration of the model, time step, and frequency of outputs. The time step is a critical component of the model and is estimated using Eq. 3-13. If the time step is not defined correctly the model will not run because of the explicit nature of the HOSS solvers. The number of cycles and stop time are then estimated depending on the goal of the model using the calculated time step. The message and data output frequencies are then calculated based on total model run time, optimizing data while considering post-processing ability.

$$\text{Eq. 3-13} \quad \Delta t = \frac{\alpha h}{\sqrt{\dfrac{E}{\rho}}}$$

The initial conditions and boundary conditions are assigned to the nodal groups that were first defined in the creation of the mesh. Through various series of if statements in each Euclidian direction, the rate, shape and duration of velocity impulses and fixed nodes is designated.

For all models completed in this study the dimensions chosen for distance, time and mass and the resultant units of importance are listed in Table 2 .

Distance	**1 *mm* (millimeter)**
Time	**1 *ms* (millisecond)**
Mass	**1 *kg* (kilogram)**
Resultant Units:	
Force	**1 *kN* (kilonewton)**
Pressure/Stress	**1 *GPa* (gigapascal)**
Energy	**1 *J* (joule)**
Density	**$1.00E+9 \frac{kg}{m^3}$**
Velocity	**$1 \frac{m}{s}$**

The last major component of the HOSS input deck that needs definition are the Message Passing Interface Domains or MPI Domains. This is how the various sections of the model are divided for computational processing. Each domain is handled by one computer processor. The domains allow for parsing of calculations and optimize computation time. MPI Domains are the essential component of models which use mass computer parallel processing. These domains are made using a geometric script and can be visualized in the post-processing software Paraview to ensure all components of the model are covered by a processor as seen in Figure 24.
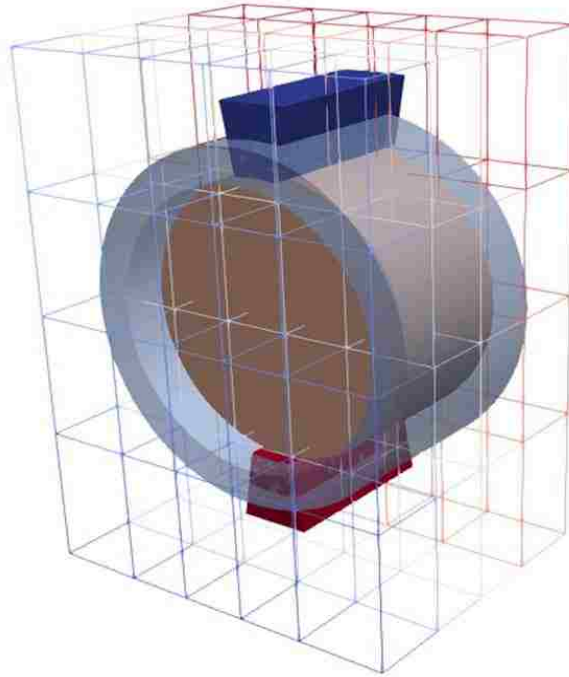
Figure 24: MPI domain configuration

Models can also be equipped with sensors which track velocity and displacement of a particular point within the model in each direction. The sensor is assigned by giving it coordinates that are covered by the geometry of at least one of the meshed bodies. The sensor then takes the average values for each of the nodes of the element that it is within, giving weight to nodes to which it is closer, these values are then written at the frequency specified and can be used to track displacements and velocities for analysis purposes.

Because FDEM simulations are still relatively computationally costly, attempting to replicate quasi-static tests can become cumbersome when it comes to simulation time. For most brittle materials and reasonable mesh sizes Eq. 3-13 results in a time step value that is between micro and milliseconds. For a test that is several minutes in length this can result in a reasonable simulation taking weeks to fully run. This time frame is unreasonable and

can be avoided by using a mass damping coefficient, calculated in Eq. 3-16. This β mass damping factor allows for the energy of the system to be reasonably reduced by applying a reduction at each node in the model. This allows for a much quicker displacement-controlled rate to be used. However, this factor should be used with great caution and the value given by Eq. 3-16 can be reduced significantly in the actual model.

Eq. 3-14
$$C = \sqrt{\frac{E}{\rho}}$$

Eq. 3-15
$$\Omega = \frac{\pi c}{h}$$

Eq. 3-16
$$\beta = 2\Omega$$

Where, β is the mass damping coefficient, C is the sound speed of the material.

3.2.4 Sleeved and un-sleeved Brazilian models

Models of the sleeved and un-sleeved experiments were created to investigate the effect of the rubber sleeve on the traditional indirect tension test. The specimen geometries had a 50.8 mm diameter and 25.4 mm thickness as in the samples in experimentation. Sensors were placed on top of the steel heads and on the sides of the specimens as seen in Figure 25 to capture the lateral displacement differences. The material properties used in these simulations are listed in Table 3, where E is the Young's modulus, ρ is the material density, and $\sigma_{T/V}$ are the tensile and shear strengths. The displacement-controlled test was simulated by specifying a downward velocity of 24 m/min on the top nodes of the top

loading head. A proportional mass damping coefficient was used to allow for the higher

loading rate, reducing computational time while maintaining quasi-static assumptions. The

concrete was defined with a FDEM mesh, while the rubber and steel heads were given a

purely FEM mesh. The concrete disk was comprised of 62,000 elements and the steel heads

and rubber utilized around 95,000 elements, using 80 MPI domains. The characteristic

length, *h*, of this model was 0.425 mm.
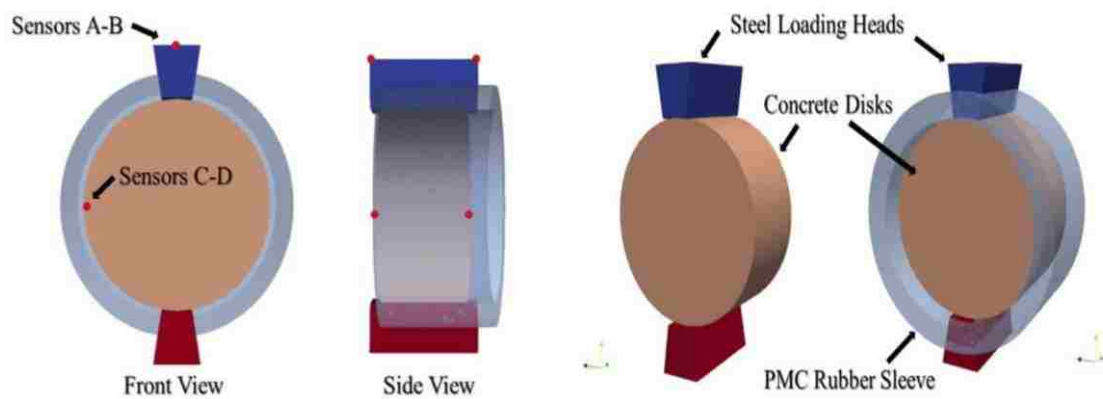
Figure 25: Sleeved and un-sleeved model setup

Table 3: Sleeved un-sleeved model properties

Material	Property	Value
Concrete	E (GPa)	10.0
	ρ (kg/m^3)	2340
	υ	0.15
	$\sigma_{T/V}$ (MPa)	3.4, 6.2
	G$_I$, G$_{II}$ (J/m^2)	110, 128
	δ_T, δ_S (mm)	0.02, 0.02
Steel	E (GPa)	200.0
	ρ (kg/m^3)	7800
	υ	0.3
Rubber	E (MPa)	1.72
	ρ (kg/m^3)	1040
	υ	0.48
	$\sigma_{T/V}$ (MPa)	5.17

3.2.5 Large aggregate traditional Brazilian model and mesh convergence study
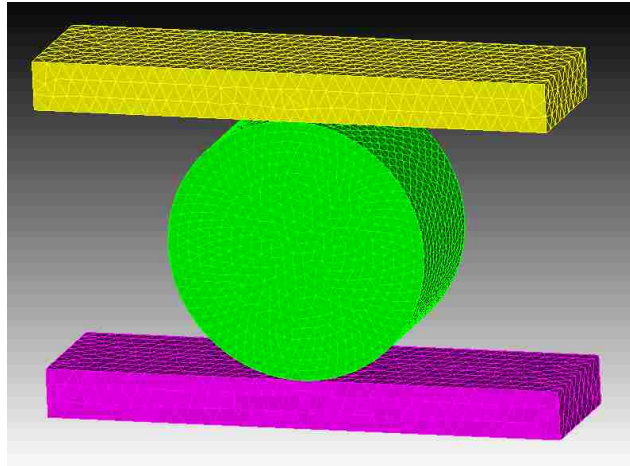
Figure 26: Traditional Brazilian model set-up

A traditional Brazilian model was created to be compared with the stiffened Brazilian model and to ensure the model is behaving properly according to experimental results obtained by Rusch, et. al. 2018. The model was constructed to mimic the experimental parameters used as seen in Figure 27. The experimental set-up consisted of a loading frame with simple parallel plates, with the sample set in between the plates with thin pieces of wood to help stabilize and prevent rotation of the sample.

Figure 27: Traditional Brazilian experimental set-up

The geometry of the model is seen in Figure 26 and consists of steel plates large enough to capture the same line of load seen in experimentation, with the concrete sample centered between the plates. It can be noticed that the model neglects the pieces of wood as there is no rotation in the perfect geometry of the model. Additionally, the wood pieces would simply complicate the behavior of the model as it is difficult to truly capture the material properties of the pieces and would require exceptionally small elements to replicate the thin pieces which would then control the time step of the whole model.
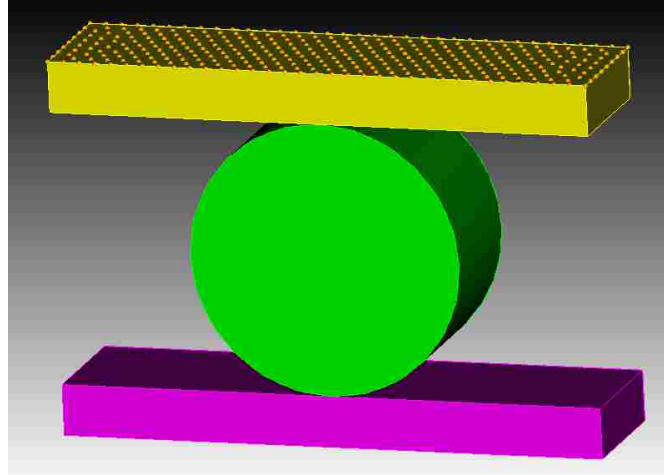
Figure 28: Top node velocity assignment

The top nodes on the top steel plate were assigned a velocity to represent the displacement-controlled load used in experimentation (Figure 28). The load used in experimentation was 0.05 mm/min, a very slow value as permeability measurements were taken during testing. A mass damping coefficient was also used here to offset the incredibly slow load rate in the model with a reasonable computation time. The modeled concrete specimen utilized 105,274 elements, a total of 117,258 elements were used in this model. For this model h = 0.9461276 mm, resulting in a cell size of around 0.19 mm. The material properties used in the model are in Table 4.

Table 4: Model Properties: Standard Brazilian & Mesh Convergence

Material	Property	Value
Concrete	E (GPa)	11
	ρ (kg/m^3)	2,347
	υ	0.17
	$\sigma_{T/V}$ (MPa)	5.5, 9.2
	G_I, G_{II} (J/m^2)	100, 128
	δ_T, δ_S (mm)	0.03, 0.03
Steel	E (GPa)	200.0
	ρ (kg/m^3)	8,000
	υ	0.3
Penalty	P (GPa)	3,000

This model also served as a datum for a mesh convergence study of the concrete disk, the results of which can be seen in section 4.3.2. A mesh convergence study is needed to understand the critical mesh size which sufficiently allows for the most accurate behavior replication while minimizing computational cost. Since the concrete disk is the only FDEM mesh used, only the mesh of the disk needed a convergence study as all other components were pure FEM meshes and were given sufficient size to allow for optimal computational usage and contact of integration points. The mesh sizes compared in the study are shown in Figure 29.
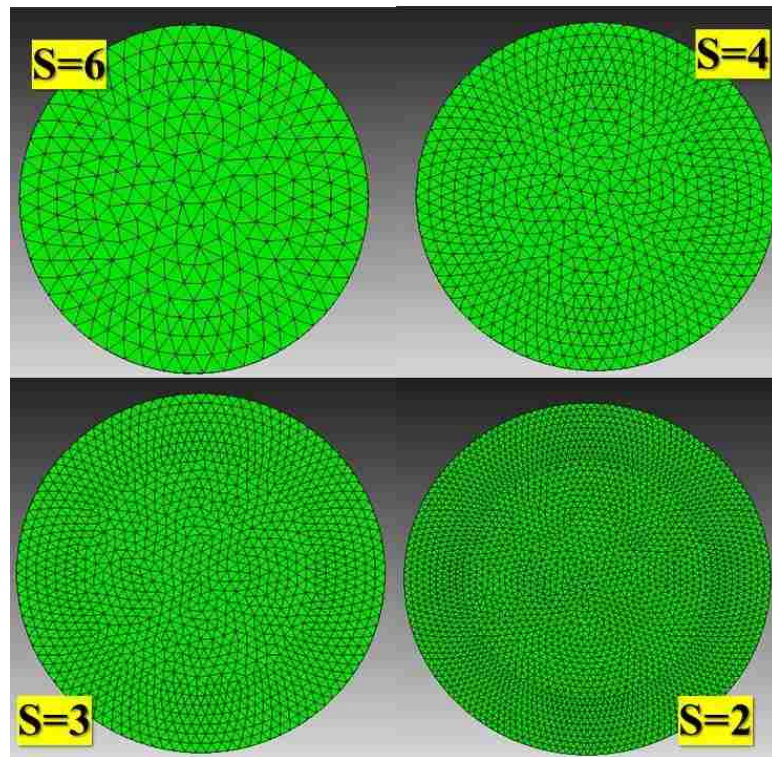
Figure 29:Mesh sizes in convergence study of concrete sample

The effects of the mass damping coefficient are also compared at different percent levels of the calculated value using Eq. 3-16. It has been suggested that approximately 10% of this calculated value should be used. The results of the comparison between no mass

damping coefficient, 10%, 50%, 100% and 200% of the calculated value are shown in section 4.2.3.

3.2.6 Stiffened Brazilian model

The stiffened Brazilian model was set-up as a perfect geometric representation of the experiment seen in Figure 18. Two hollow cylinders were added to the traditional Brazilian model spaced at 6" (152.4 mm) on center, Figure 30, to represent the added PVC pipes.
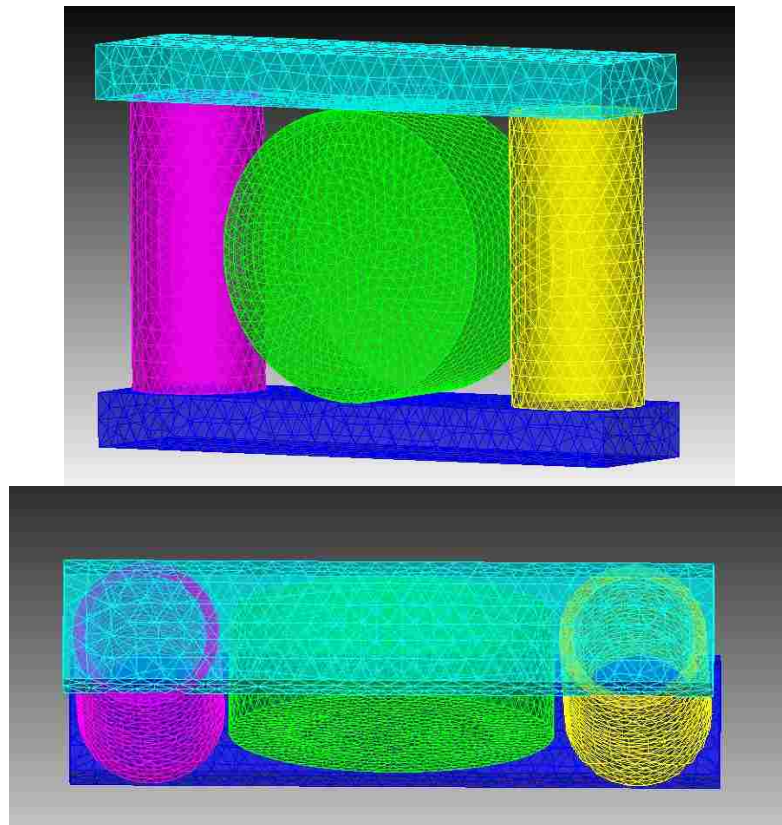
Figure 30: Stiffened Brazilian model set-up

The same nodal assignments of the top plate were used to replicate the displacement-controlled loading, and a mass damping coefficient of 10% the calculated value was used. The concrete specimen used 105,274 tetrahedrons, with a model total of 135,246 elements.

57

The characteristic length of this model was 0.9461276 mm, with a 0.19 mm cell size. The

concrete and steel properties for this model are listed in Table 5.

Table 5: Model Properties: Stiffened Brazilian

Material	Property	Value
Concrete	E (GPa)	11
	ρ (kg/m^3)	2,347
	υ	0.17
	$\sigma_{T/V}$ (MPa)	5.5, 9.2
	G$_I$, G$_{II}$ (J/m^2)	110, 128
	δ_T, δ_S (mm)	0.03, 0.03
Steel	E (GPa)	200.0
	ρ (kg/m^3)	8,000
	υ	0.3
PVC	E (GPa)	3.4
	ρ (kg/m^3)	1,400
	υ	0.40
Penalty	P (GPa)	3,000

3.2.7 Pre-damaged stiffened Brazilian model
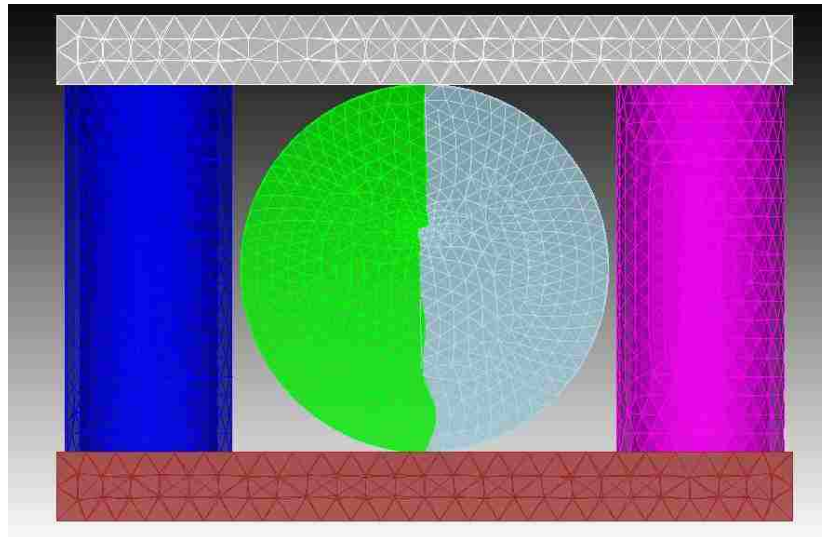
Figure 31: Pre-damaged stiffened Brazilian model

The pre-damaged model was created from results of the dynamic impact testing. Sample number 2 discussed in section 4.2.2 was used for replication in this model. The specimen before being placed in the stiffened Brazilian apparatus and after dynamic impact had the pattern of the hairline fracture photographed. The hairline fracture was then mapped using ImageJ software, with corresponding line segments as seen in Figure 32. The length of the segments were calibrated based on the diameter of the sample as seen in Figure 33, assuming a perfect diameter length of 101.6 mm for pattern replication in the model.
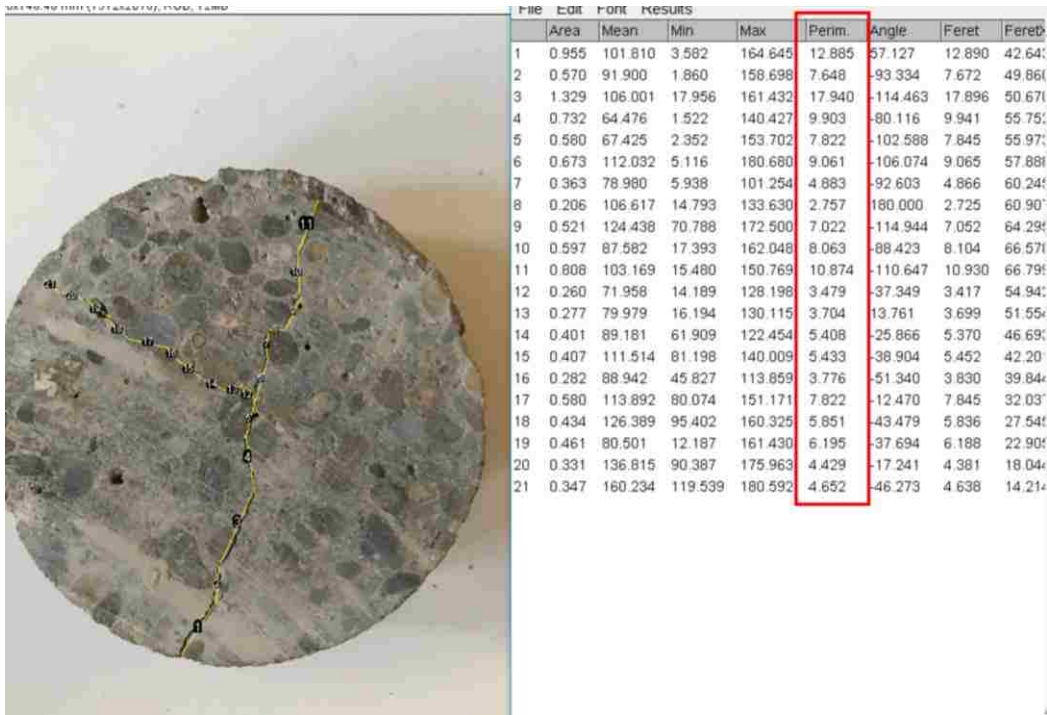
Figure 32: Mapping of fracture segments and lengths with ImageJ
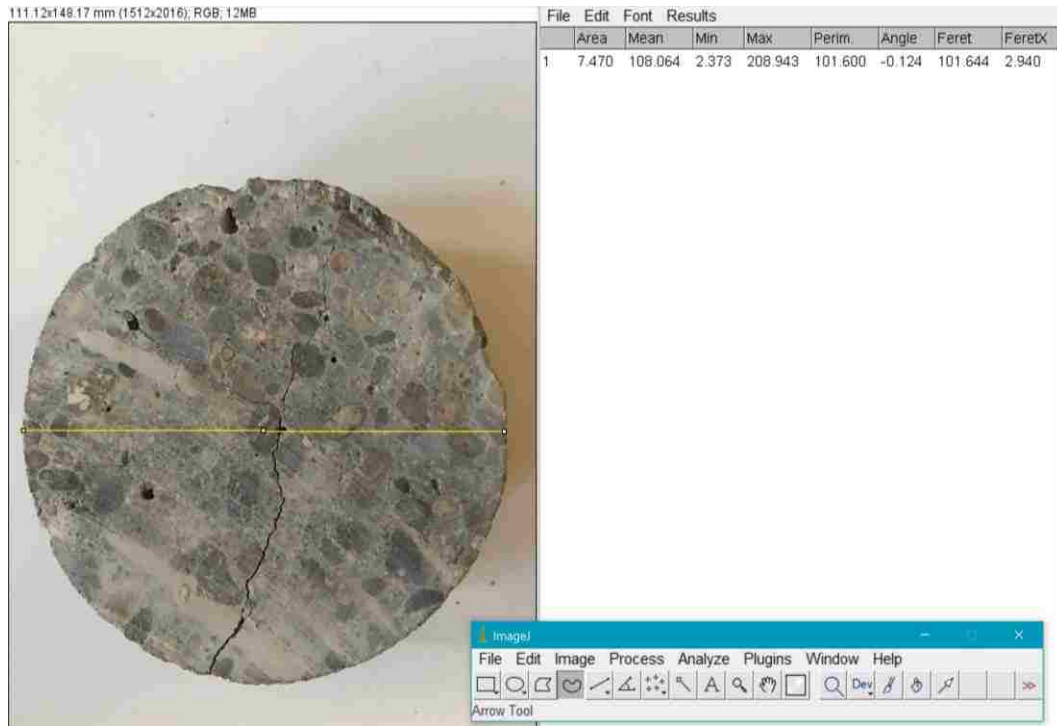
Figure 33: Diametric pixel calibration in ImageJ

The ImageJ software then outputs the x and y coordinates of the beginning and end of each line segment in reference to the upper righthand corner of the image. These values were then used to place vertex coordinates in the model space, thus mapping the pattern of the fracture into the geometry of the model. The resultant mapped fracture can be seen in Figure 34. It should be noted that only the main hairline fracture was replicated in the model, as the final orientation of the specimen in the stiffened Brazilian had the main fracture parallel to the line of load and governed the resultant failure.
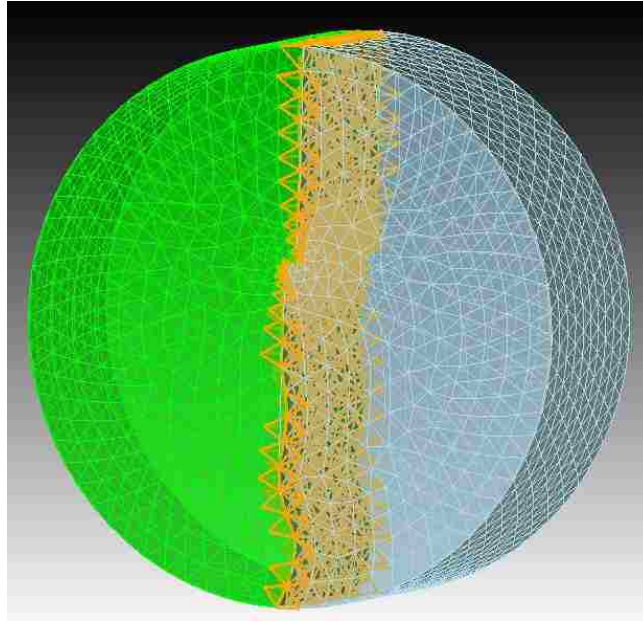
Figure 34: Tetrahedrons in sample body assigned to fracture

It was evident from the specimen after impact that the fracture had propagated throughout the thickness of the sample and in order to model the behavior of the fracture it was assumed that the pattern of the fracture was maintained throughout its thickness. The fracture was first defined by connecting the vertex locations derived using ImageJ with curve entities inside the Trelis software. The curve was then swept into a surface which then allowed for the separation of the sample body into two parts. After meshing, the tetrahedrons which had a face that was part of the surface of the fracture were assigned to a group and assigned a material block (**C_crack**), see Figure 34. Because the specimen had to be divided into two pieces each side had to be separately defined as its own material block (**C_sampleleft & C_sampleright**) as seen in Figure 35.

61
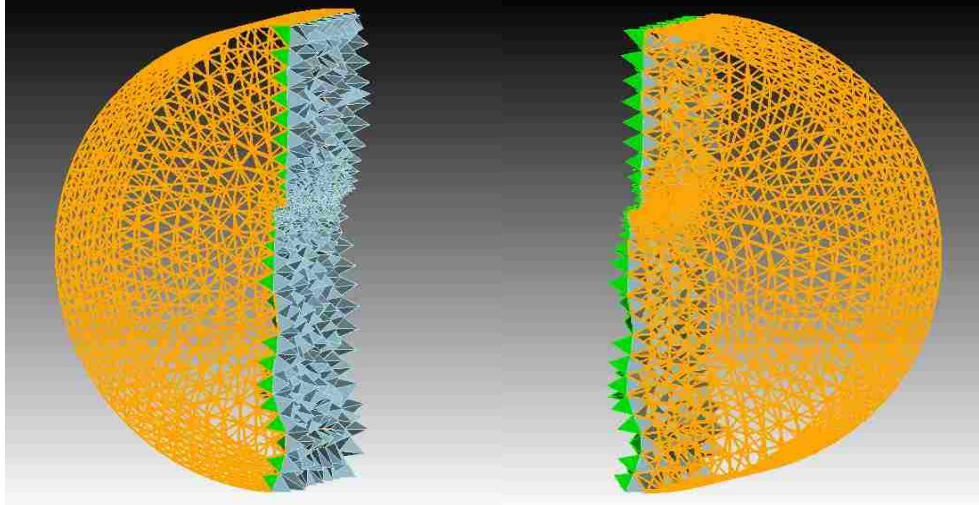
Figure 35: Body separation in pre-damaged model

The fracture was modeled this way to use the cohesion interaction capabilities present in

the FDEM platform HOSS. Each material body involved in the interaction is assigned

respective cohesion properties as discussed in section 2.2.1. The tetrahedrons belonging to

the normal parts of the concrete, both left and right, are assigned G1-G1 and G2-G2

cohesion interactions. The elements belonging to the fracture are assigned a G3-G3

interaction. All these interactions describe how the elements that are part of the same group

are to interact with one another. For the interactions between the elements belonging to the

fracture and the elements part of the left and right sides of the specimen, G1-G3, G3-G1,

G2-G3, and G3-G2 cohesion interactions are specified, where G1-G3 and G3-G1 are

similar in nature but are crucial in designating the nature of target and contactor elements

within the interaction. G1-G1 and G2-G2 interactions are assigned the normal cohesion

properties of the concrete used in both the traditional and stiffened Brazilian models. G1-

G3, G2-G3 and their respective converses are assigned similar cohesion properties, with

the exception of a reduced shear and tensile strength, 50% of the original used in the normal

concrete cohesion interactions. Lastly, the G3-G3 interactions, those of the fracture line

were given the same properties but with dramatically reduced shear and tensile strengths. A comparison of the percent of original tensile and shear strengths used for the cracked elements was made, the results of which can be seen in section 4.3.4. During the making of the geometry for this model it is important to ensure that all entities are properly merged and compressed, because if tetrahedrons from one group are overlapped with tetrahedrons from another group then the penalty term that exists between them will result in a repulsion between the two groups.

The material properties assigned to the various material blocks in this model are listed in Table 6. This model utilized 65,190 elements for the sample, 1,558 belonging to the fracture group, and a model total of 78,806 elements. The value of h was 1.00 mm with a cell size of 0.2 mm.

Table 6: Material Properties: Pre-damaged Stiffened Brazilian

Material	Property	Value
Concrete	E (GPa)	16
	ρ (kg/m^3)	2,347
	υ	0.17
	$\sigma_{T/V}$ (MPa)	5.5, 8.5
	G$_I$, G$_{II}$ (J/m^2)	110, 128
	δ_T, δ_S (mm)	0.03, 0.03
Crack	$\sigma_{T/V}$ (MPa)	0.55, 0.92
	G$_I$, G$_{II}$ (N/m)	110, 128
	δ_T, δ_S (mm)	0.44, 0.45
Steel	E (GPa)	200.0
	ρ (kg/m^3)	8,000
	υ	0.3
PVC	E (GPa)	3.4
	ρ (kg/m^3)	1,400
	υ	0.40
Penalty	P (GPa)	3,000

CHAPTER 4 | RESULTS AND DISCUSSION

4.1 Material Characterization Results

4.1.1 Fine Aggregate Specimens

The results of 5 unconfined compression tests for the fine aggregate specimens are listed in Table 7. The concrete properties listed in Table 8 were determined using ASTM standards from the results listed in Table 7.

Table 7: Results of unconfined compression tests of fine aggregate specimens

No.	Max Load (lb)	Max Stress (psi)	Max Stress (MPa)
1	19320	6149.75	22.40
2	11000	3501.41	24.14
3	7610	2422.34	16.70
4	9456	3009.94	20.75
5	9304	2961.56	20.42
Average	11338	3609.00	20.88

Table 8: Concrete properties (finer aggregate)

Young's Modulus, E (Gpa)	20 (Eq. 3-1)
Compressive Strength, (Mpa)	20.88
w/c ratio	0.45

A grain size distribution was completed with the finer aggregate to aid in the determination of the size of the mesh in the model for this more homogenous concrete profile. The maximum aggregate size used in this mix was 4.75 mm or below the standard No. 4 sieve. The grain size distribution in terms of percent passing and percent retained are in Figure 36 and Figure 37. The properties of the aggregate based on the D_{10}, D_{30}, D_{60} values are listed in Table 9.
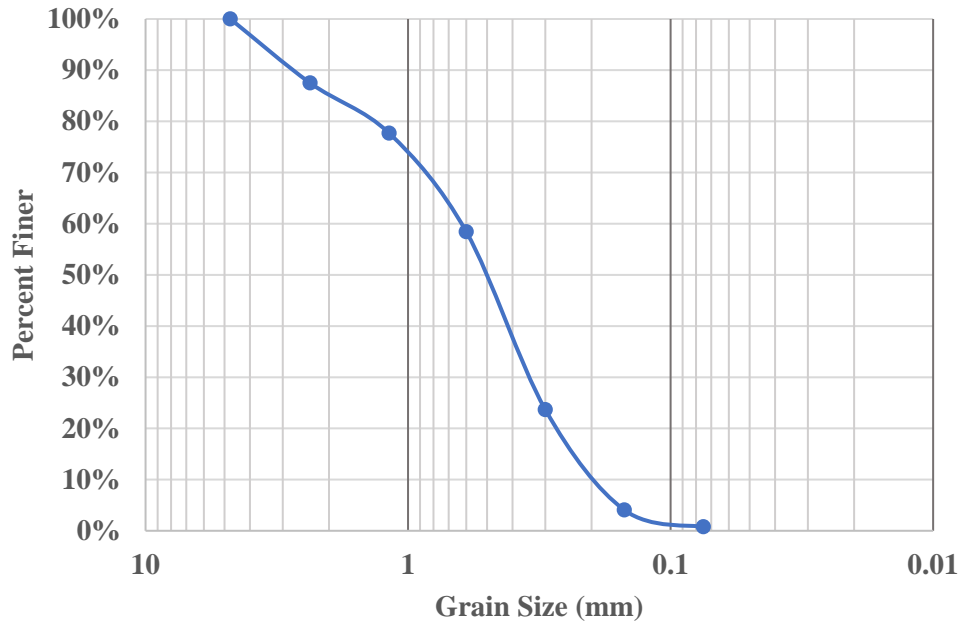
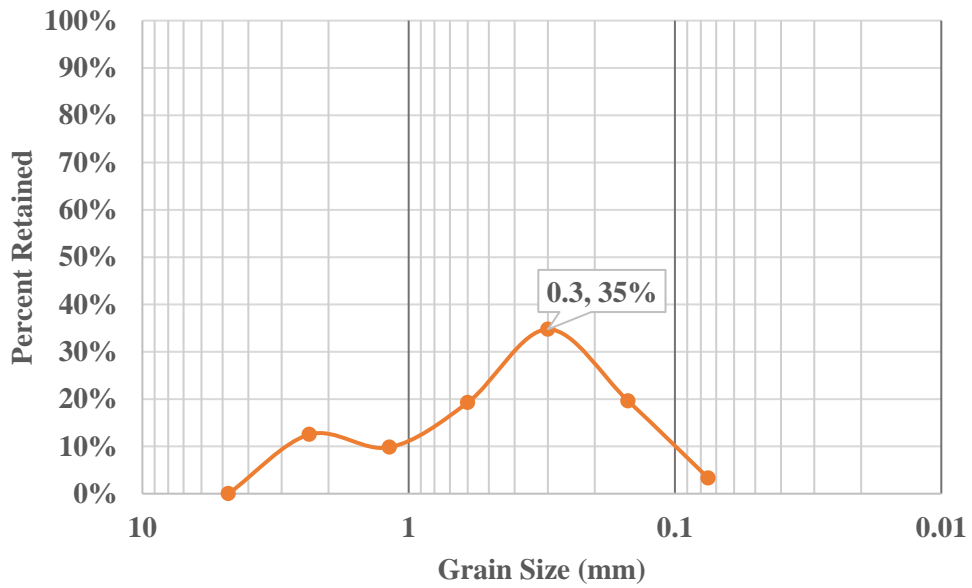**Figure 36: Grain size distribution of aggregate used (percent finer)**

Figure 37: Grain size distribution of aggregate used (percent retained)

Table 9: Fine aggregate properties

Aggregate Parameter	Value
Effective size, D_{10} (mm)	0.20
D_{30} (mm)	0.35
D_{60} (mm)	0.65
Uniformity coefficient, C_U	3.25
Curvature coefficient, C_C	0.27

The finer aggregate, having a uniformity coefficient of around 3, is a fairly uniform soil. This can also be observed in the percent retained graph, where 35% of the mass belongs to grain sizes between 0.3mm to 0.6mm. The size of the mesh within the FDEM model for the fine aggregate specimens was optimized to utilize the least number of elements in the sample, to preserve reasonable computation time and power, while maintaining a characteristic length in this range to allow the fracture replications to occur on a comparable scale in the model. The resultant optimum characteristic length used in the model for the fine aggregate concrete specimens was around 0.34 mm.

4.1.2 Coarse Aggregate Specimens

The results of 5 unconfined compression tests for the coarse aggregate specimens are listed in Table 10. The resultant material properties of the coarse concrete are listed in Table 11 and were calculated with the results from Table 10 and ASTM methods.

Table 10: Results of unconfined compression tests for coarse aggregate concrete

Specimen no.	Peak Load (lb)	Peak Stress (psi)	Peak Stress (Mpa)
1	60560	4819.21	33.23
2	61900	4925.85	33.96
3	60240	4793.75	33.05
4	50020	3980.47	27.44
5	50670	4032.19	27.80
Average	56678	4510.29	31.10

Table 11: Concrete properties of disk specimens (coarser aggregate)

Young's Modulus, E (Gpa)	26.9 (Eq. 3-1)
Compressive Strength, (Mpa)	31.10
w/c ratio	0.45

4.2 Experimental Results

4.2.1 Sleeved & un-sleeved Brazilian results

The results of the sleeved and un-sleeved Brazilian indirect tension tests using 20-degree steel loading arcs of the fine aggregate concrete samples are seen in Figure 38 to Figure 40. The vertical load displacement profile of the un-sleeved specimen is seen in Figure 38 where a relative stiffness is seen up to failure followed by a relatively ductile failure for brittle materials but typical in small diameter disk specimens in the Brazilian. (Zdenek et al., 1991).
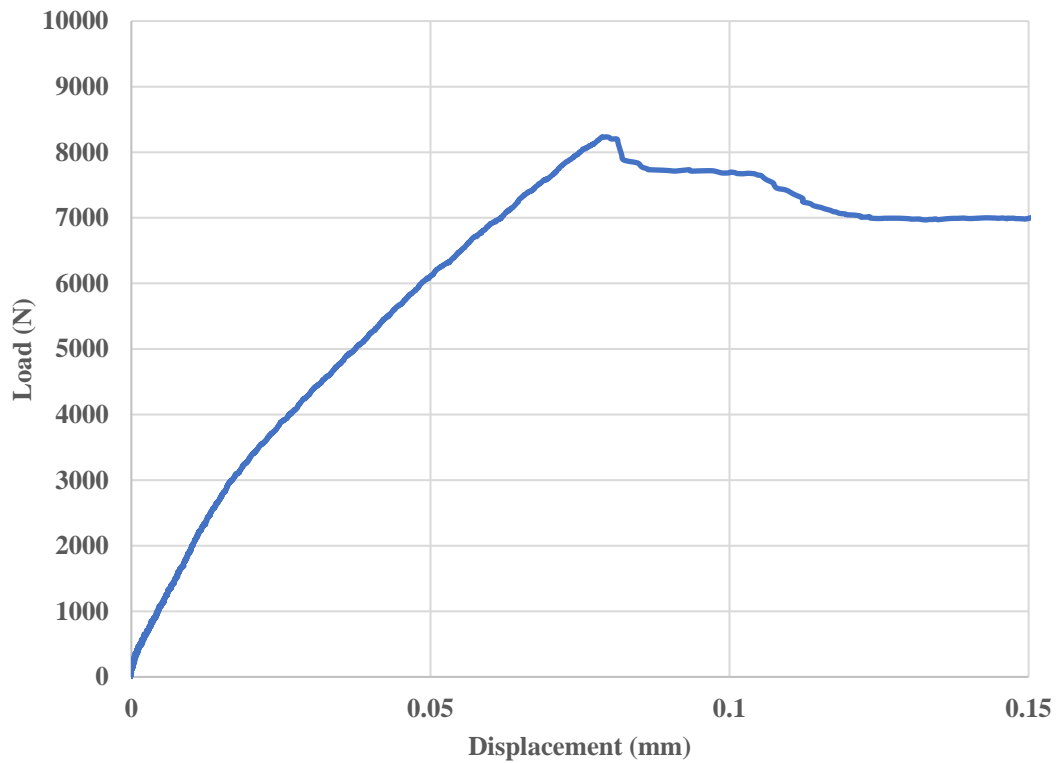
Figure 38: Profile result of un-sleeved specimen load displacement

The vertical load displacement profile of the sleeved specimen is seen in Figure 39, exhibiting a clearer stiffness and a relatively ductile failure for a brittle material due to the smaller size of the disk specimen. It can be noticed that in the sleeved profile there is a lot more non-linearity before the peak load. This may be due to subtle confinement effects at failure, where the rubber sleeve is keeping the disk intact for a longer period of time.
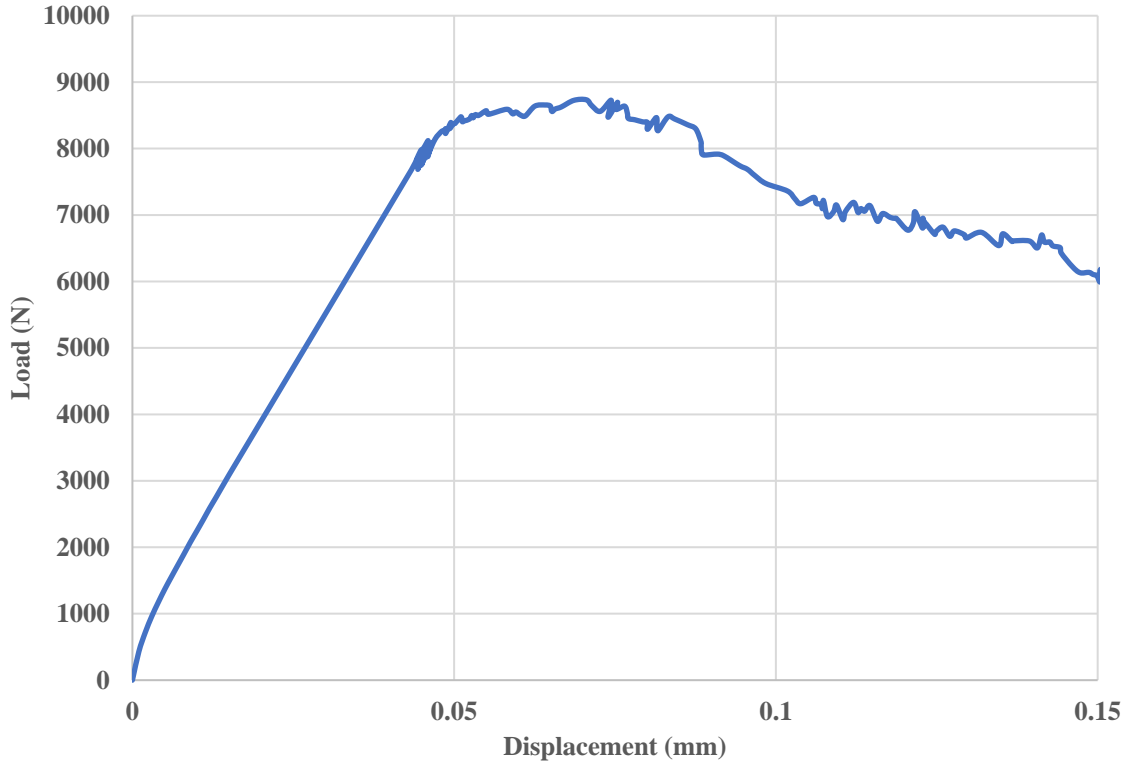
Figure 39: Profile result of sleeved specimen load displacement

Figure 40 shows the results of a statistical analysis completed for the ten sleeved and un-sleeved standard Brazilian indirect tension tests. The sleeved specimens exhibited an average tensile strength capacity that is 13.4% lower than the specimens that were un-sleeved. These results catalyzed the need to use the FDEM platform to investigate this phenomenon further.
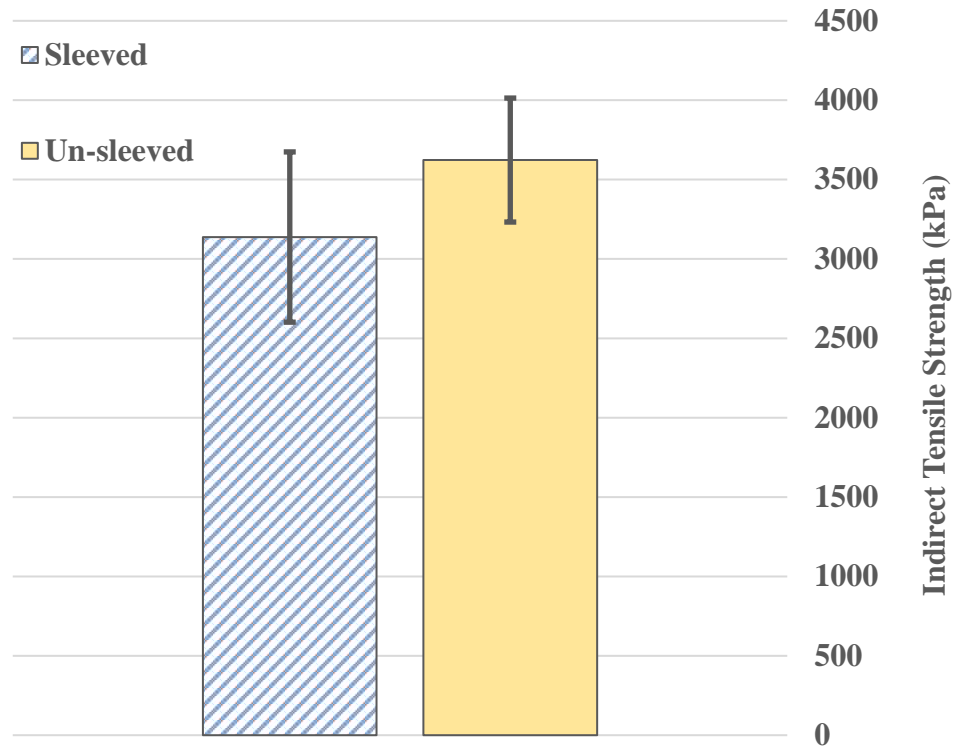
Figure 40: Comparative results of sleeved vs. un-sleeved indirect tensile strengths

4.2.2 Dynamic Impact Results

To utilize a pre-damaged specimen from the drop tower in the stiffened Brazilian set-up it is important to know what the orientation of potential fracture paths and damage are. If the main damage in the set-up is oriented perpendicular to the line of load in the Brazilian indirect tension test, then the cracks will be compressed and will not result in any easily identified change. If the main damage is mostly parallel to the line of load, then the mechanics of the Brazilian indirect tension test will have shifted as the integral part of the specimen which takes the most tensile stresses has been sufficiently weakened.

Initially, it was thought that a pattern of crack orientation could potentially be identified from the drop tower set-up being used. From the literature discussed in section 2.2.3.2 it was suggested that the crack orientations will vary radially in a random fashion, however

70

this is still not well understood so a datum was arranged in the drop tower to attempt to detect if a pattern might emerge as seen in Figure 41. Several vertical lines were drawn on the face of the specimen across the diameter to be lined up with a reference on the machine support. If a pattern emerges it will be seen in reference to these datum lines.
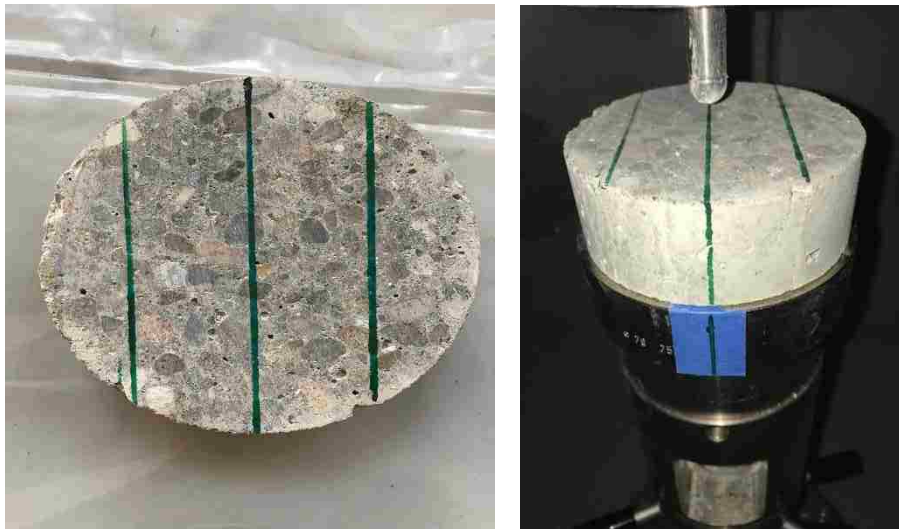
Figure 41: Set-up to determine fracture orientation

The results of this analysis can be seen in Figure 42. It is evident that there is no clear pattern of radial cracks that emerge from the drop tower impact utilized. There is no way to guarantee that any damage that is not evident to the eye would propagate in a direction that can then later be oriented in the stiffened Brazilian properly.
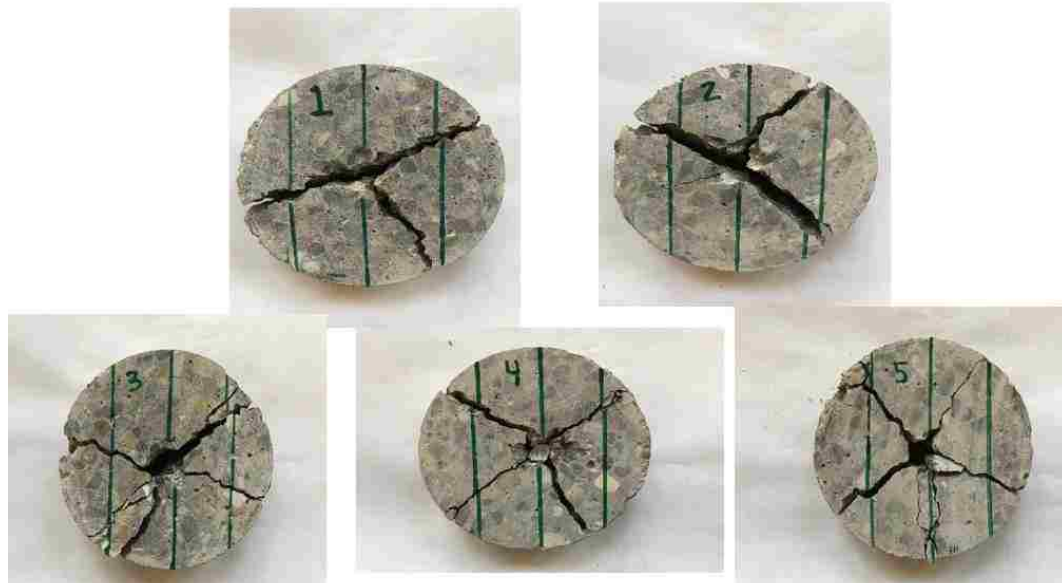
Figure 42: Radial crack orientation results from drop tower impact

Because of the results of this analysis it was determined that introducing a line of minimum potential by restraining on side of the disk specimen could be utilized. Restraining the movement of one side of the disk allows the creation of damage to be able to be assumed to occur in the direction of the restraint. This is because as the specimen is impacted the energy of the expanding specimen is directed away from the restraint, resulting in tensile stresses orthogonal to the restraint direction. The disk was restrained using a bar clamp and as can be seen in Figure 43 the fracture is allowed to propagate in the direction of the restraint. There is a small force that is applied as a result of the bar clamp, but is not high enough to dramatically impact the major factors of the drop test, as it can be seen in Figure 43 that other cracks are still allowed to propagate in other lines of minimum potential due to thickness variances, aggregates and other factors.

Figure 43: Minimum potential line with resultant fracture line

A total of 5 specimens were tested after a calibration based on drop height to induce a substantive amount of damage in the specimens. The piezoelectric sensor results of the 5 specimens from the impact drop tower can be seen in Figure 44 to Figure 48.
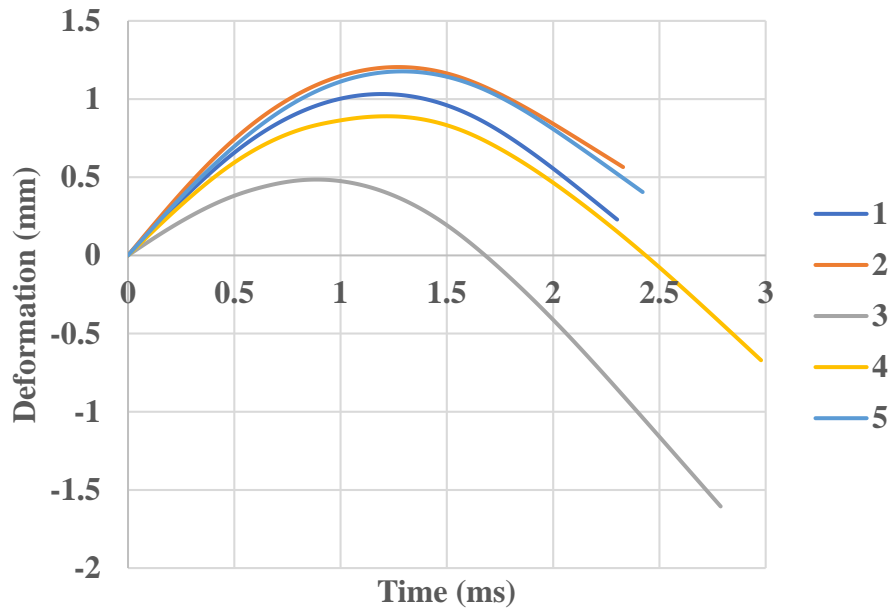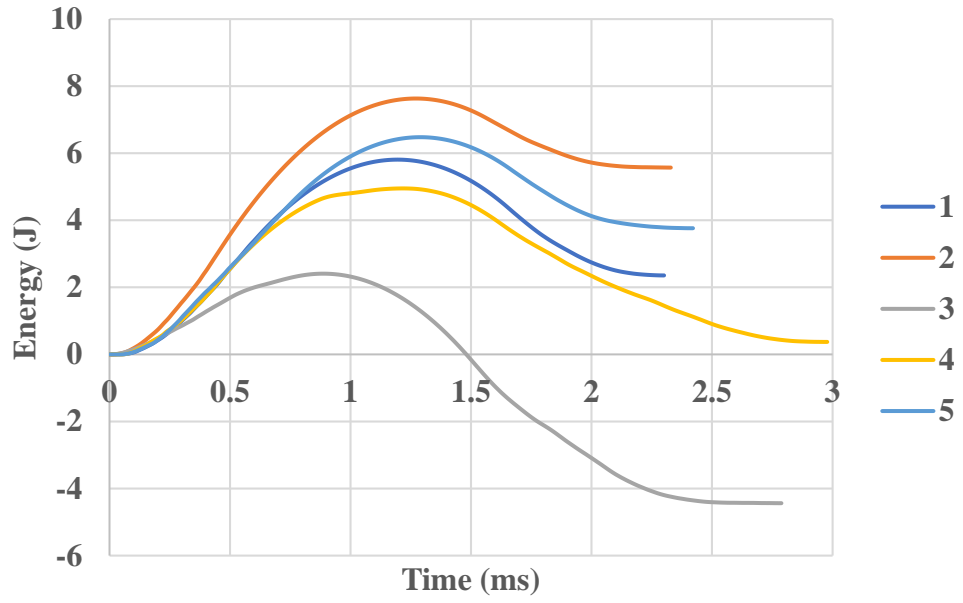

Figure 44: Facial impact deformation time history

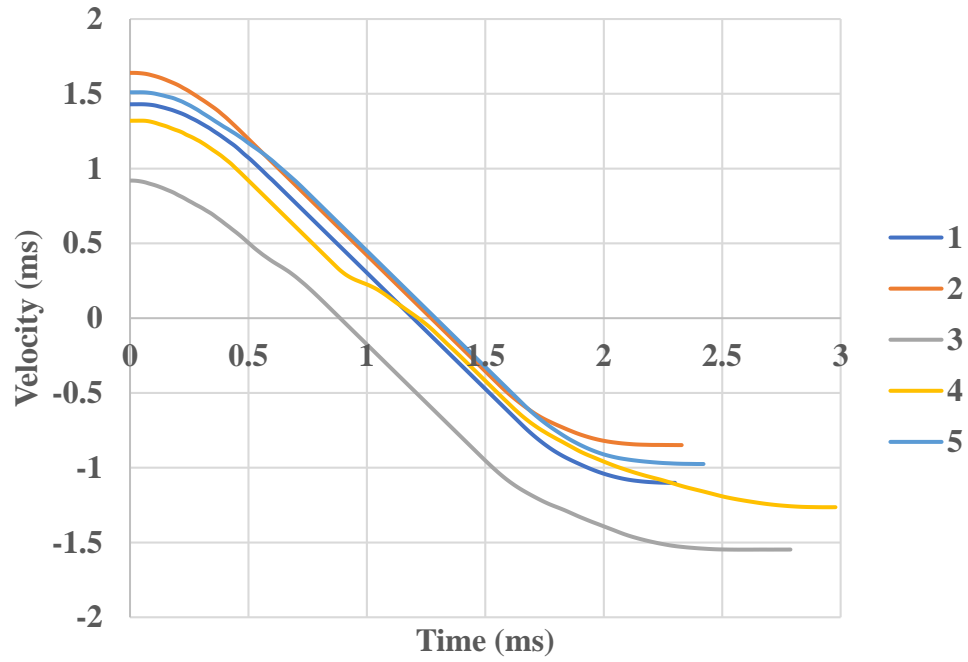**Figure 45: Impact energy time history**

Figure 46: Impact of rod velocity time history

74

As can be seen form the graphs of deformation, energy, and velocity time histories there are two specimens which exhibited substantially different behavior. Specimen 3 and 4 exhibited hairline fractures after impact and are also the two samples which exhibited differing behavior in their respective time histories. The sensor used to capture these particular time histories is a piezoelectric meter that is attached to the head of the impacting rod. Thus, these time histories seem to mainly be capturing the behavior that is exhibited in the facial impact itself. The specimens which exhibited hairline fractures show less energy than those that did not, suggesting that a certain amount of the potential energy from the drop height and mass is going elsewhere than in the process which the piezoelectric meter is capturing. This same principle is observed in the deformation and velocity time histories, where a heavy amount of rebound is observed in the deformation time histories indicating again that more energy went elsewhere than went into the creation of an impact crater.

Before and after impact the apparent permeability of the samples was measured using the system described in section 3.1.3, and the results can be seen in Figure 47. The two samples which exhibited hairline fractures showed several orders of magnitude greater permeability than before they were impacted. Those that did not have hairline fractures did not exhibit any significant change in permeability. This suggests that unless a hairline fracture is present, there is no significant change in permeability that can be detected using this measurement system.
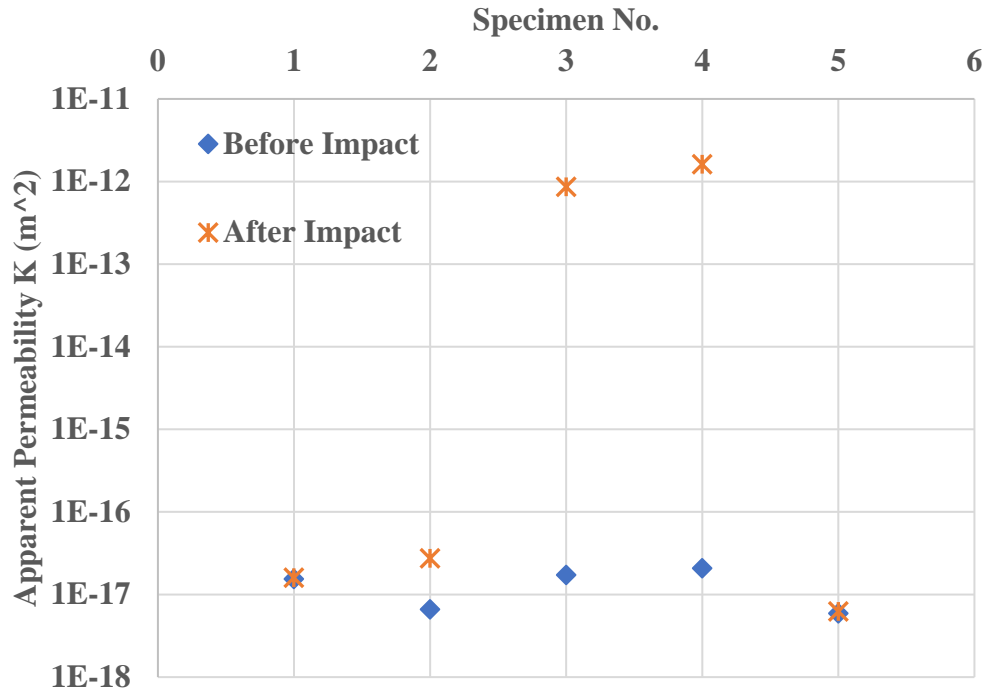
Figure 47: Apparent permeability results before and after impact

All 5 impacted (1-5) specimens and a specimen which was not impacted were submitted to the stiff Brazilian indirect tension test. Table 12 lists the results of the corresponding peak load and their fracture status, NVF stands for no visible fracture and VF stands for visible fracture. Specimen 3 is pictured in Figure 48 exhibiting a resultant hairline fracture on the front and back of the specimen. Specimen 3 is the sample used in the pre-damaged stiffened Brazilian modeling efforts as well as the sample results shown in section 4.2.3.

Table 12: Comparative results of impacted concrete disks in the stiff BITT

Specimen	Fracture Status	Peak Load (N)
Non -impacted	--------------	26402
1	NVF	2320
2	NVF	2735
3	VF	10078
4	VF	1174
5	NVF	2473

Figure 48: Specimen No. 3 resultant hairline fracture

4.2.3 Results of pre-damaged stiff Brazilian indirect tension test

The results of specimen No. 3 in the stiff Brazilian indirect tension test can be seen in Figure 49 to Figure 51. The crack propagation before and after the test can be observed in Figure 49. The initial fracture line induced from the drop tower impact appears to be one single fracture. The sample after the stiff Brazilian indirect tension test shows the increased width of that fracture line, but also displays a second fracture line which emerges from the bottom and doesn't appear to connect to the initial fracture line from the surface images available. It is possible that the fractures connected internally.

Figure 49: Pre-damaged specimen at beginning and end of test

The vertical load displacement profile of this pre-damaged specimen is shown in Figure 50. There is an apparent non-linear stiffness, a result of the changing stiffness of the sample as the crack continues to open. The decline in load begins to occur at a vertical displacement of about 0.15 mm, which could be explained by the full progression of the second fracture line which appeared during testing.
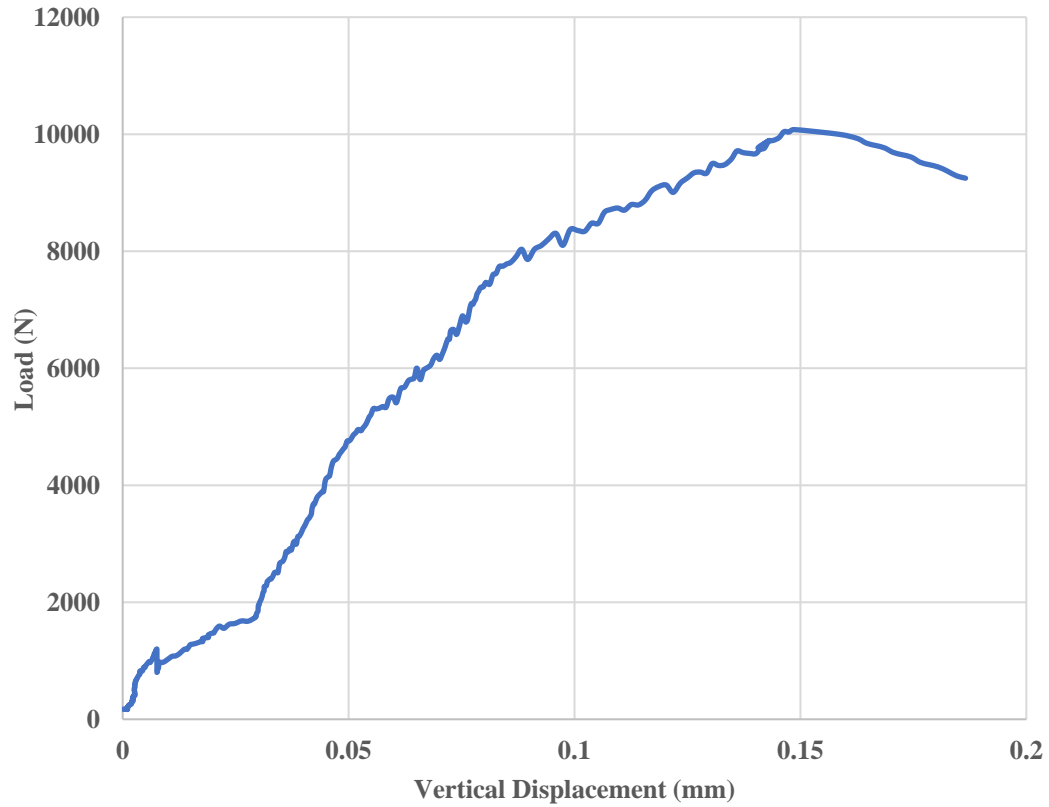
Figure 50: Vertical load displacement of pre-damaged stiff BITT

The relative crack opening displacement (ΔCOD) against load profile is shown in Figure 51. The results show a resistance of the sample to lateral opening until about 2 kN, followed by increased opening with increasing load until about 0.1 mm when the load begins to decrease. This profile seems to indicate that the initial crack induced by impact required additional stresses to fully propagate.
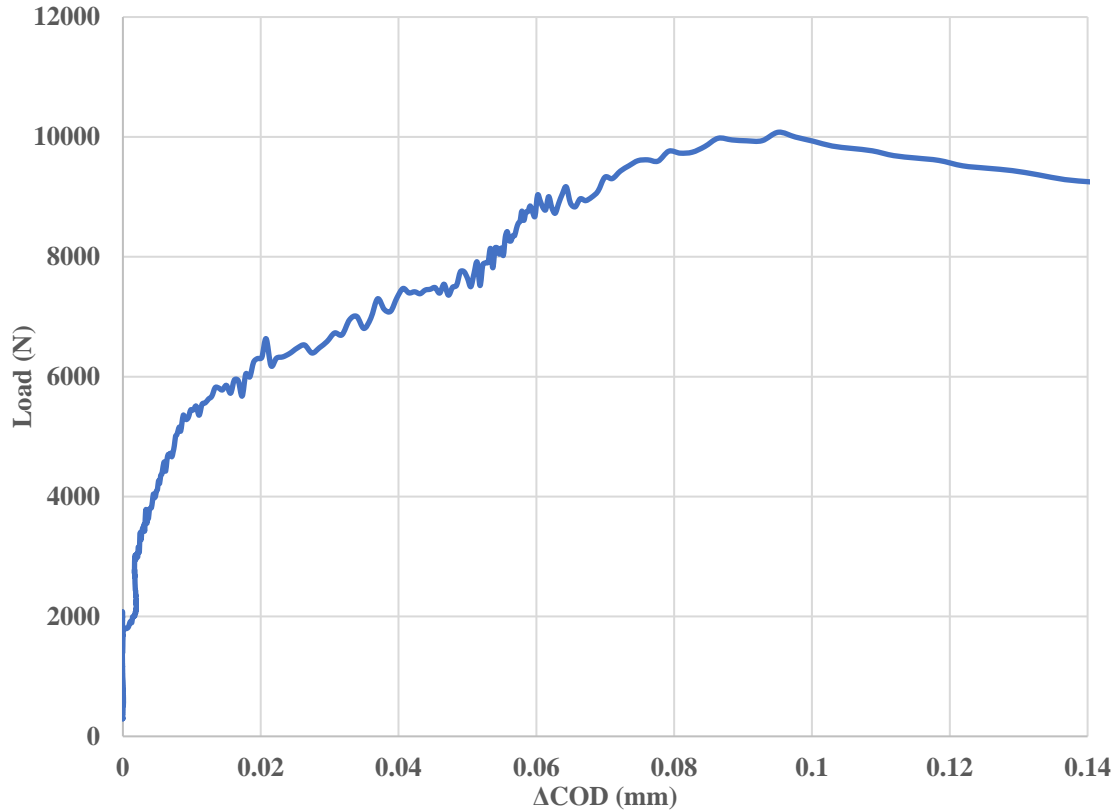
Figure 51: COD of pre-damaged stiff BITT

4.3 Numerical Results

4.3.1 Sleeved and un-sleeved results

The results of the FDEM modeling of the sleeved and un-sleeved standard Brazilian indirect tension tests are shown in Figure 52 to Figure 54. The validation of the model for the un-sleeved standard Brazilian indirect tension test is shown in the vertical load displacement profiles shown in Figure 52 and Figure 53. The elastoplastic portion of the load displacement curve, where damage has occurred, and the magnitude of the peak were the critical aspects the simulation needed to replicate. The behavior of the simulation adequately matches the behavior observed in experiments in these critical areas in both the

sleeved and un-sleeved cases. Figure 54 confirms the brittle failure of the model is consistent with the experimental results of the sleeved specimen by comparison of the resultant fracture pattern of the specimen.
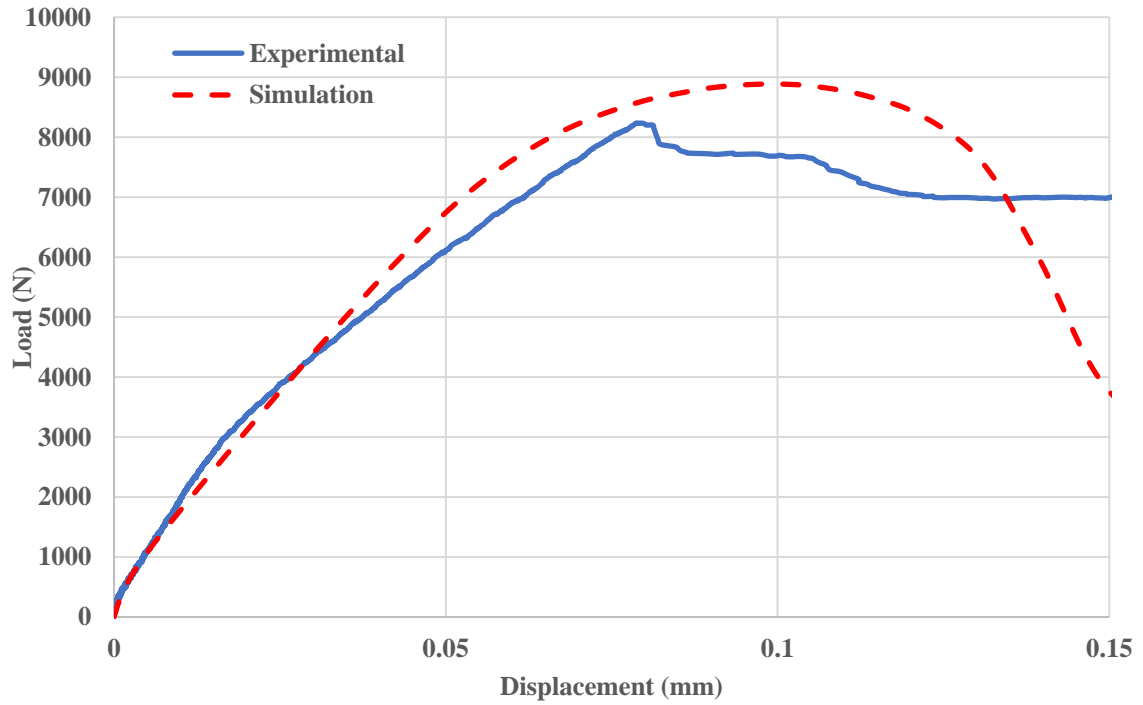

Figure 52: Model results of un-sleeved standard BITT
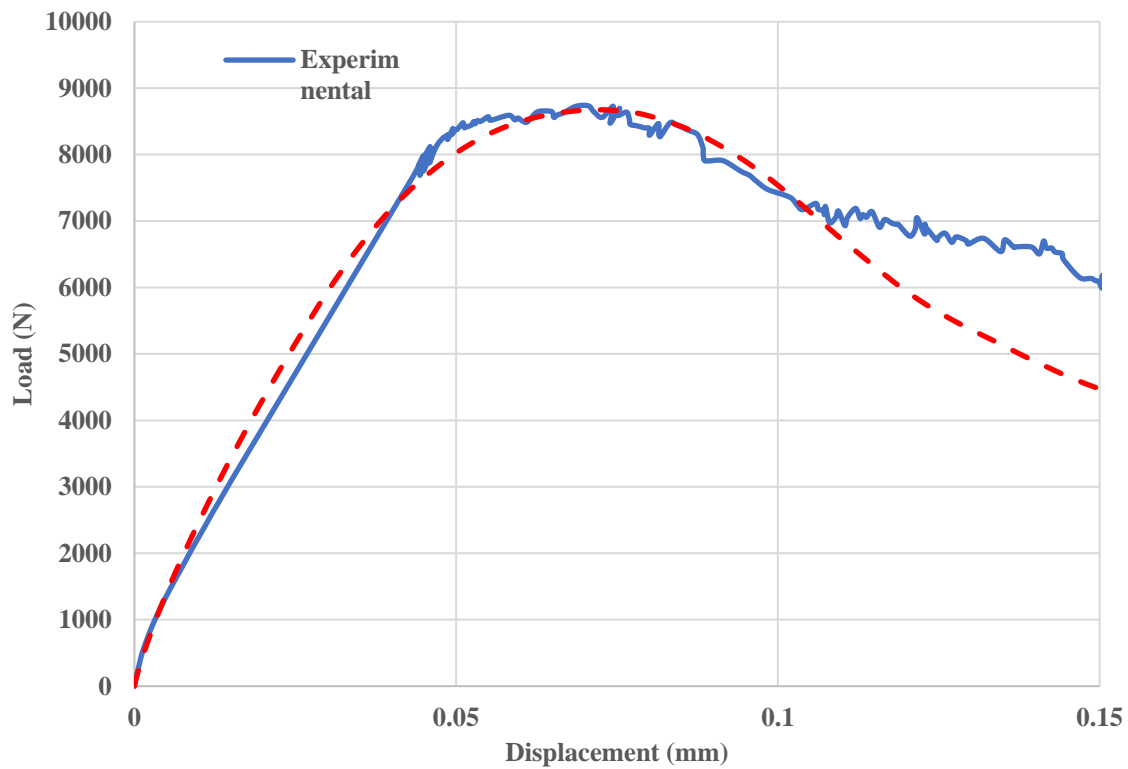
Figure 53: Model results of sleeved standard BITT
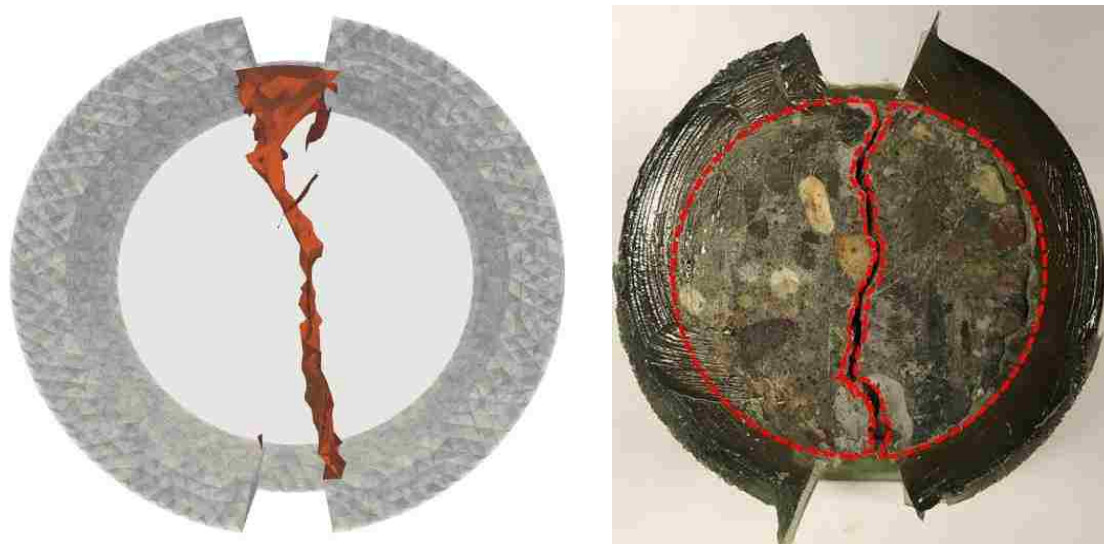
Figure 54: Validation of sleeved model fracture pattern

The results of the differences between the sleeved and un-sleeved lateral displacements against simulation time are shown in Figure 55. It can be observed that the sleeved specimen exhibits increased lateral displacement of the tracked nodes in the model when compared to the un-sleeved model. The sleeved specimen resulted in around 0.002mm more lateral displacement during the same duration. This increased lateral displacement is believed to be a result of the strength of the bond between the rubber and the concrete sample. The rubber has a much lower stiffness and results in greater lateral deformation along the diameter of the specimen. The bond between the concrete and rubber has enough strength for this added deformation to contribute to the added deformation seen in the concrete specimens.
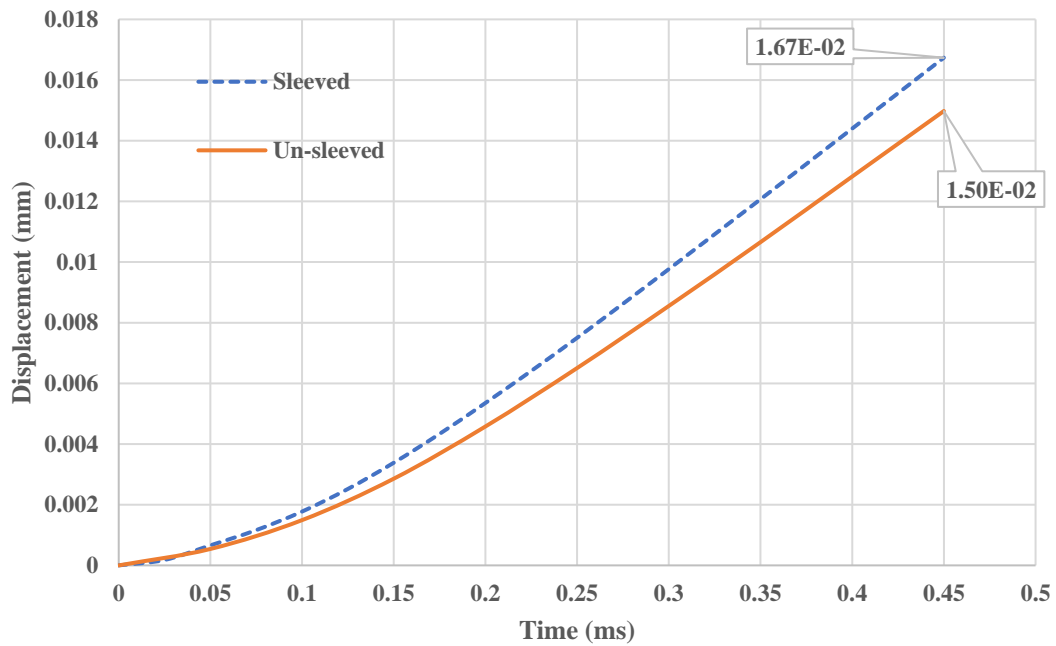
Figure 55: Comparison of lateral displacements of disk sensors C-D in model

From the stress profiles of the sleeved and un-sleeved models observed in Figure 56 this increased lateral deformation results in the attaining of the peak stress sooner in the sleeved model. The sleeved specimen is subjected to the increased stress at an earlier time, resulting in an overall decrease in the peak load also observed in the experimental results. This decrease in peak load in the model is around 6.6%, while the experimental is at 13.4%. This suggest that there may be additional factors which could be contributing to the change of the fundamental mechanics of the indirect tension test due to the use of a rubber sleeve. That is why the decision was made to evaluate other options for fitting the Brazilian indirect tension test for permeability measurements. It is important to either maintain the known mechanics of the standard Brazilian indirect tension test or to be able to evaluate with confidence the damage processes that are occurring. The rubber sleeve seems to be adding unnecessary complications for the purposes of the broader goal of the project.
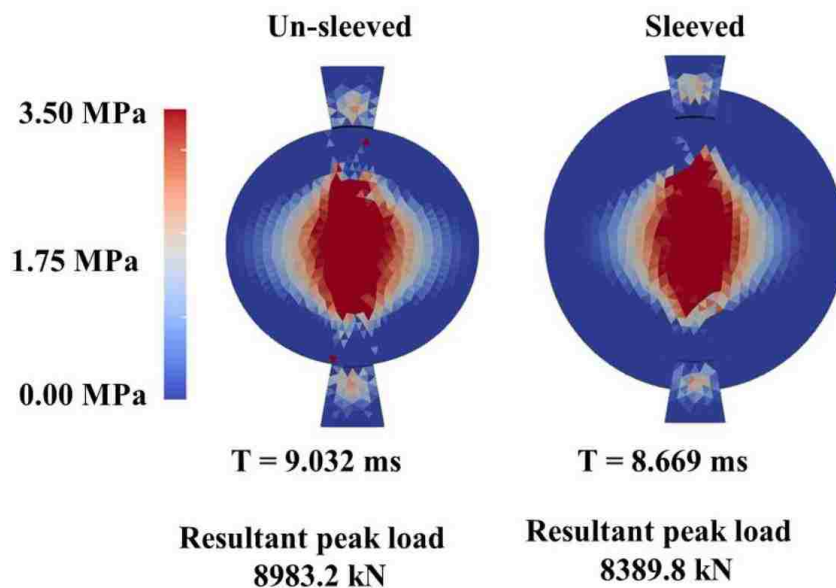
Figure 56: Stress profiles in model of sleeved vs un-sleeved disk specimens

4.3.2 Standard Brazilian indirect tension tests and mesh convergence

The experimental results of the standard Brazilian indirect tension test using the 4"
diameter, 2" thick concrete disk specimens obtained by Rusch et. al., (2018) are shown in
Figure 57 and Figure 58. Curve S4 was chosen to validate the model as it represents a
median of the stiffnesses present in the results.
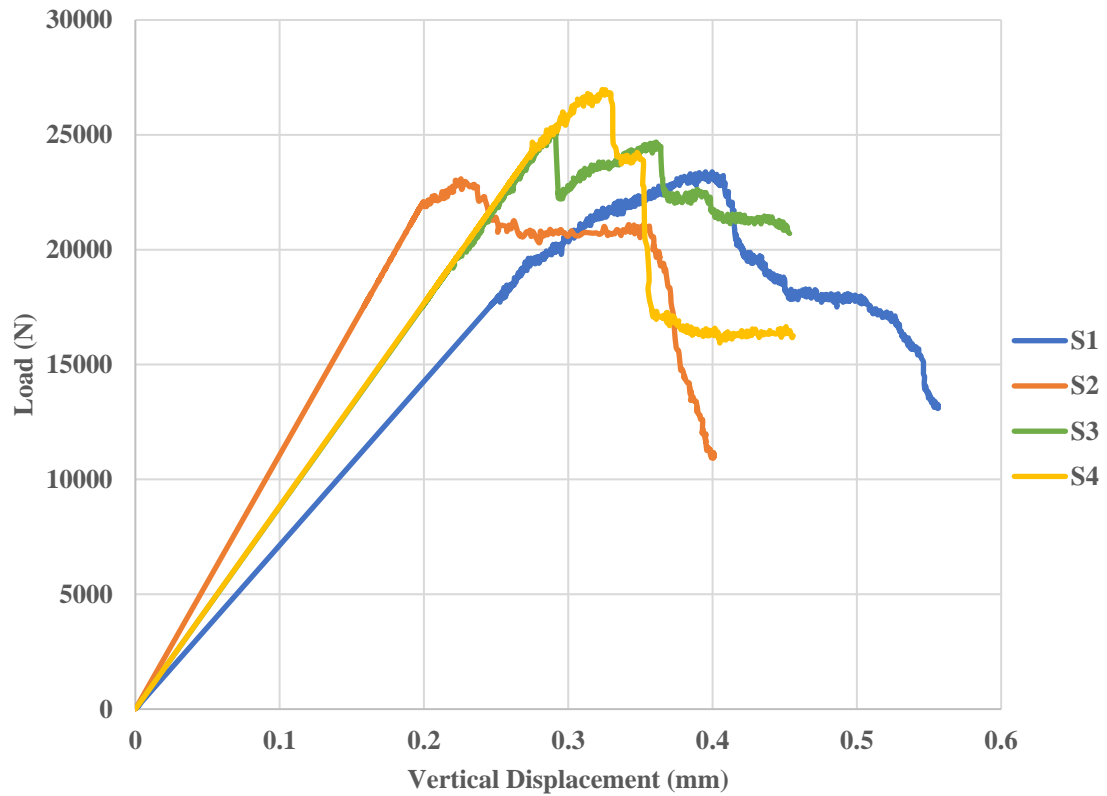
Figure 57: Vertical experimental results of standard BITT (Rusch et. al., 2018)
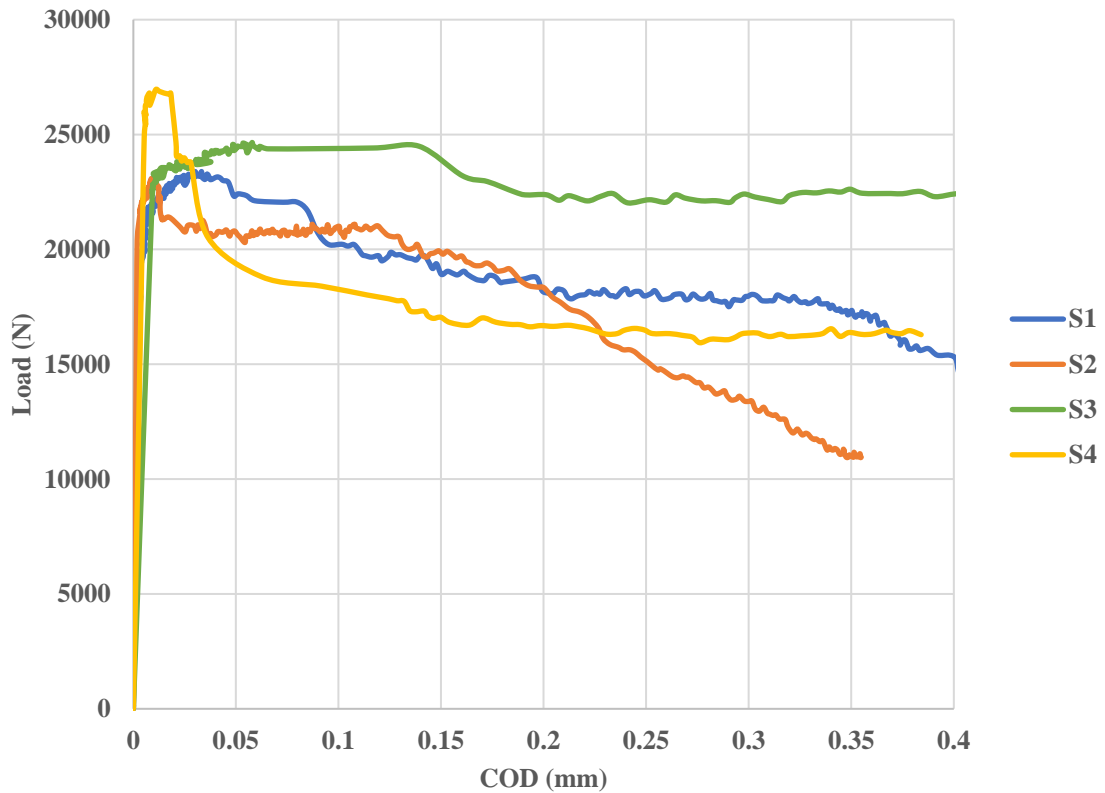
Figure 58: COD experimental results of standard BITT (Rusch et. al., 2018)

The vertical load displacement profile of the model for the standard Brazilian indirect tension test can be observed in Figure 59. The model adequately captures the elastic region and resultant magnitude of the peak load seen in experimentation. The model shows a more significant drop in load after failure than the experimental, this behavior may be explained from the use of the wood at the supports in experimentation. The wood pieces act to keep the now fractured specimens together at the contact points, where they can support the greater load as two separate column like pieces. The model which does not contain the wood sees more significant drop in load as the pieces of the disk are allowed to fully separate.
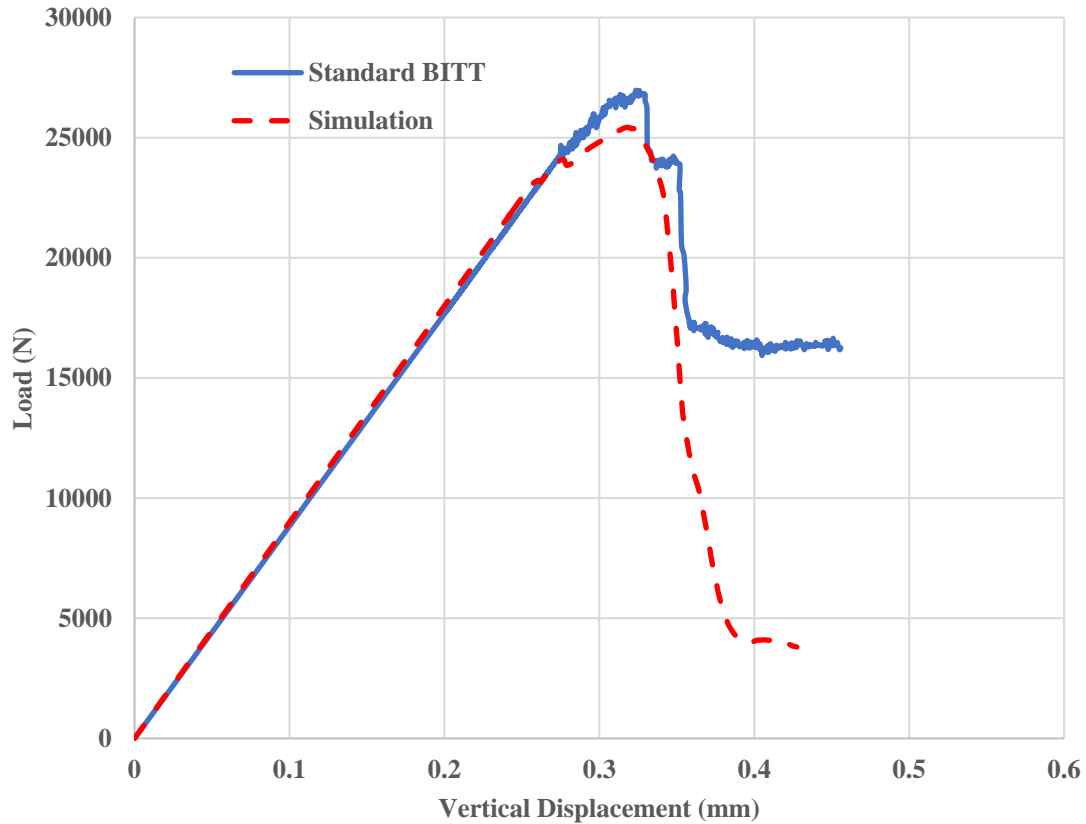
Figure 59: Model result of vertical load displacement standard BITT

In the profile of COD against load for the simulation compared to experimental, Figure 60, the simulation captures well the elastic portion before damage and fractures have begun to form. The model observes a greater drop in load after failure than the experimental. This again can be contributed to the factors stated above for the vertical load displacement comparison. There also may be some factors stemming from the initial difference in load rates used between the model and the experimental even with the mass damping factor, which will need further investigation for modeling of experiments with exceptionally slow load and displacement rates.
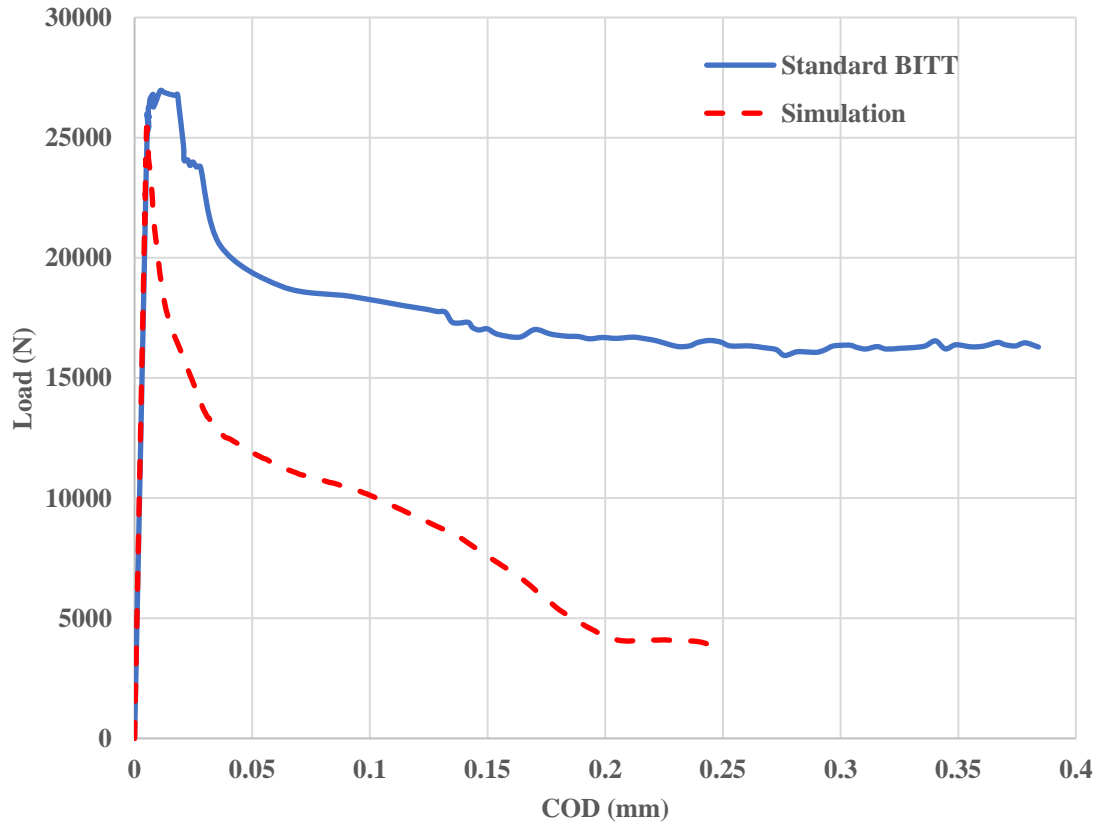
Figure 60: Model result of COD vs load standard BITT

Figure 61 and Figure 62 show the peak stress profiles of the concrete disk in the model. In

Figure 61 the stress profile that is expected from the standard Brazilian indirect tension test

in the x-direction is present, with tensile stresses present in the middle region of the sample

and compression near the contact points. As can be seen when looking at the x-direction

stress profile muted from compressive stresses, two areas within the sample appear to be

subject to heightened tensile stresses. These pockets of stress appear to occur at the junction

between the areas of compressive and tensile stresses within the sample. The elliptical

shape of the developed stress profile may be a factor in the development of these areas.

The stresses in the y-direction observed in Figure 62 display the expected pattern for the

Brazilian indirect tension test, with compressive stresses developing in the middle of the specimen, transferring the load from the top plate to the bottom plate.
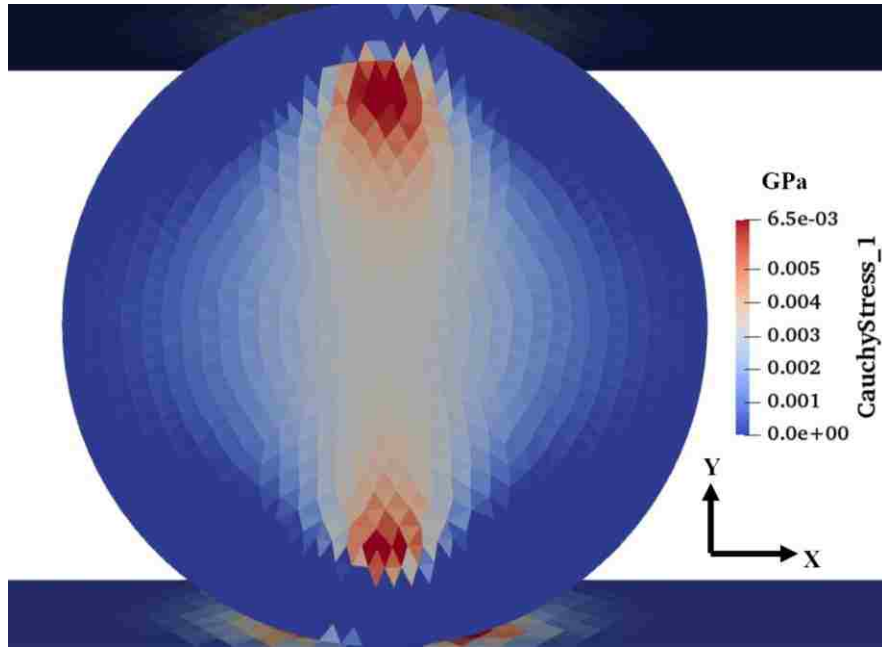
Figure 61: Model tensile stress profile in the x-direction standard BITT
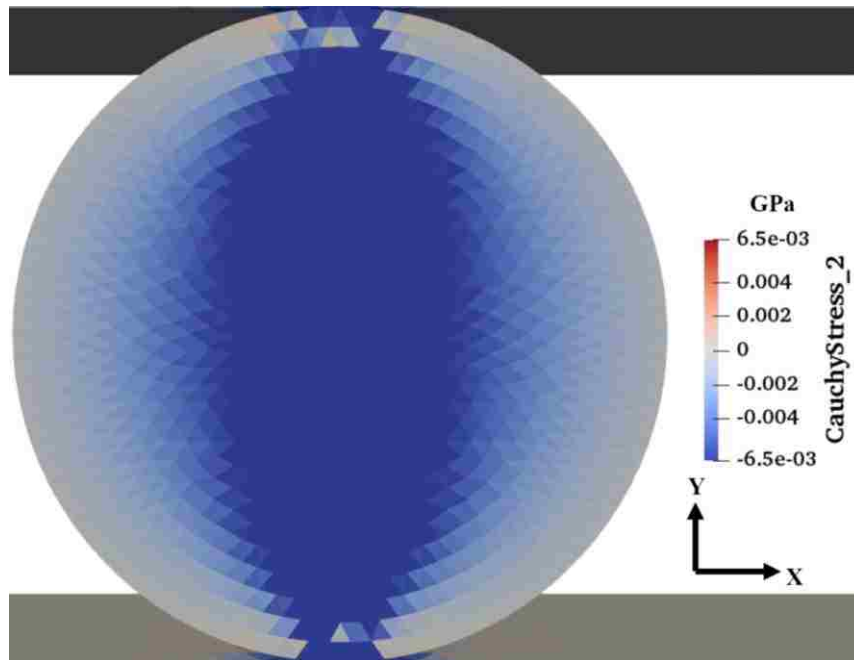
Figure 62: Model stress profile in the y-direction standard BITT

The development of tetrahedral separations within the standard Brazilian indirect tension test within the model are shown in Figure 63 and Figure 64. The magnitude of the damage progression can be observed in Figure 63 and the type, tensile or shear, can be observed in Figure 64. From these figures it can be seen that the initial separations, or damage, begin to occur at a low level at the top and bottom of the specimen. These initial separations occurring near the top and bottom can be seen to be mainly shear separations. As the fracture begins to propagate, from the top to the bottom, the separations begin to become mainly tensile separations. The resultant damage is tensile separations in the center along the fracture line, with combined and shear separations near the contact points.
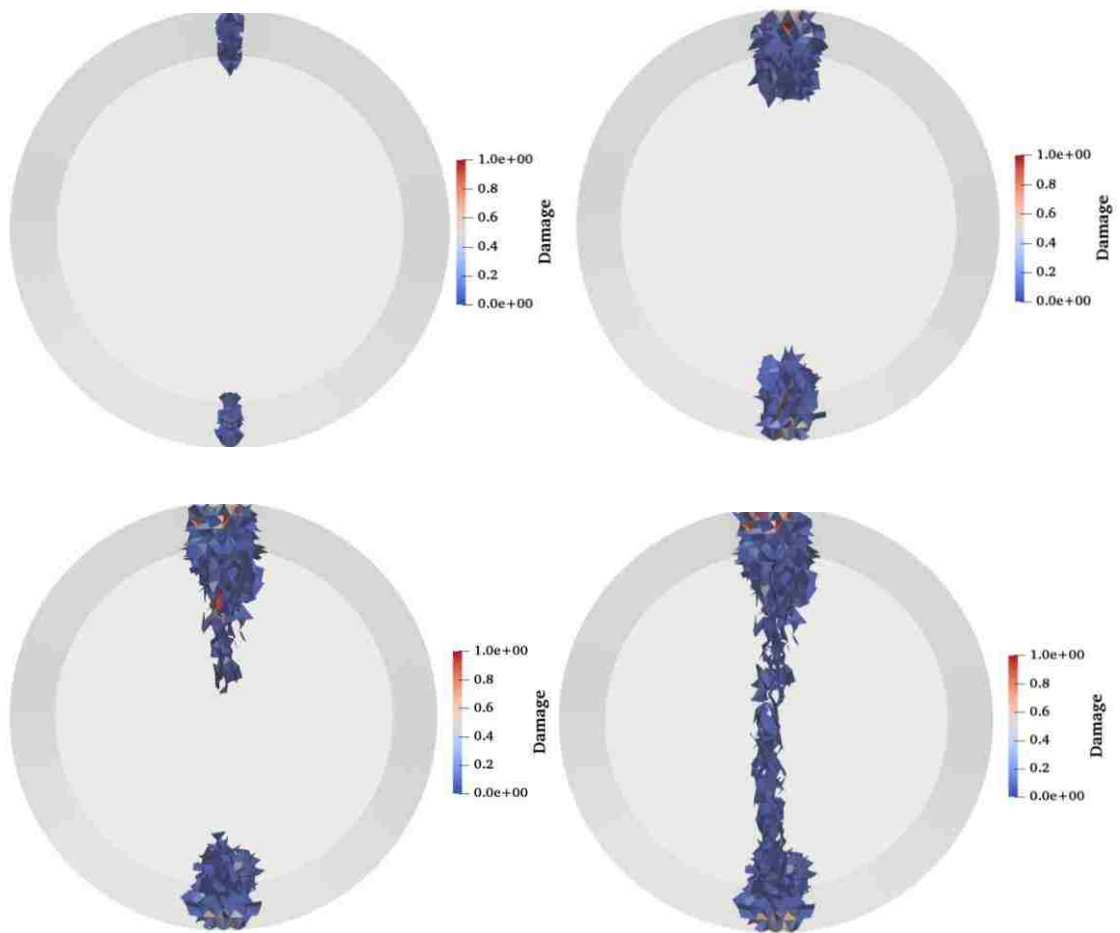
Figure 63: Model damage magnitude progression standard BITT
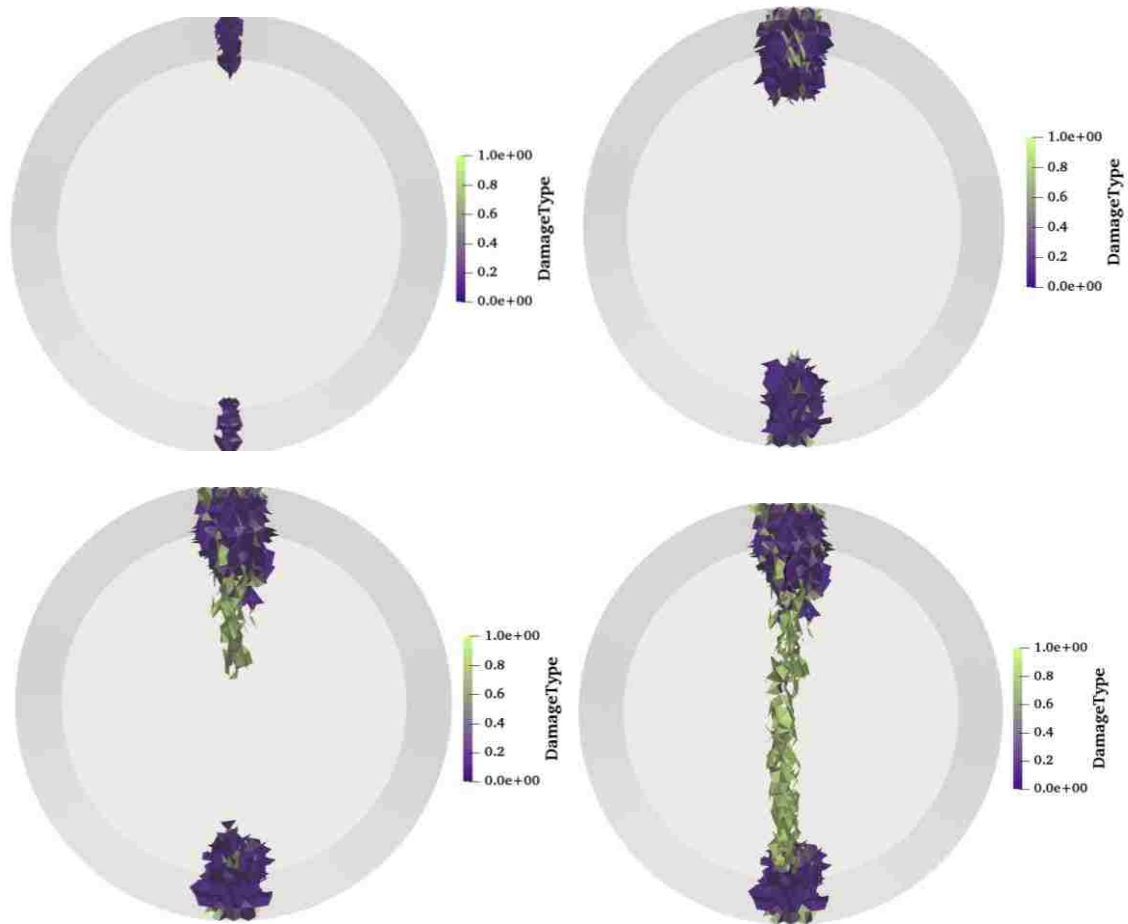
Figure 64: Model damage type progression standard BITT

The results of the mesh convergence study completed with the standard Brazilian indirect tension test are shown in Figure 65. It can be seen that as more tetrahedrons are used to model the sample the stiffnesses and peaks converge. To illustrate the principle of computational proficiencies Table 13 shows the number of processors and computation times needed for each mesh size used in this study. The stiffness of the standard Brazilian clearly converges at a mesh size of 4 and the peak loads reach a 5% convergence quickly at a size of 6. For the simulations in this study a mesh size of 3.5 was used, to have a reasonable computational time and to be within the converged sizes.

Table 13: Mesh convergence study computational proficiency of sizes

Mesh Size	No. of elements	Computational processors needed	Simulation time
6	49,508	84	4 hours
4	98,255	210	8 hours
3	193,449	320	12 hours
2	581,240	512	16+ hours
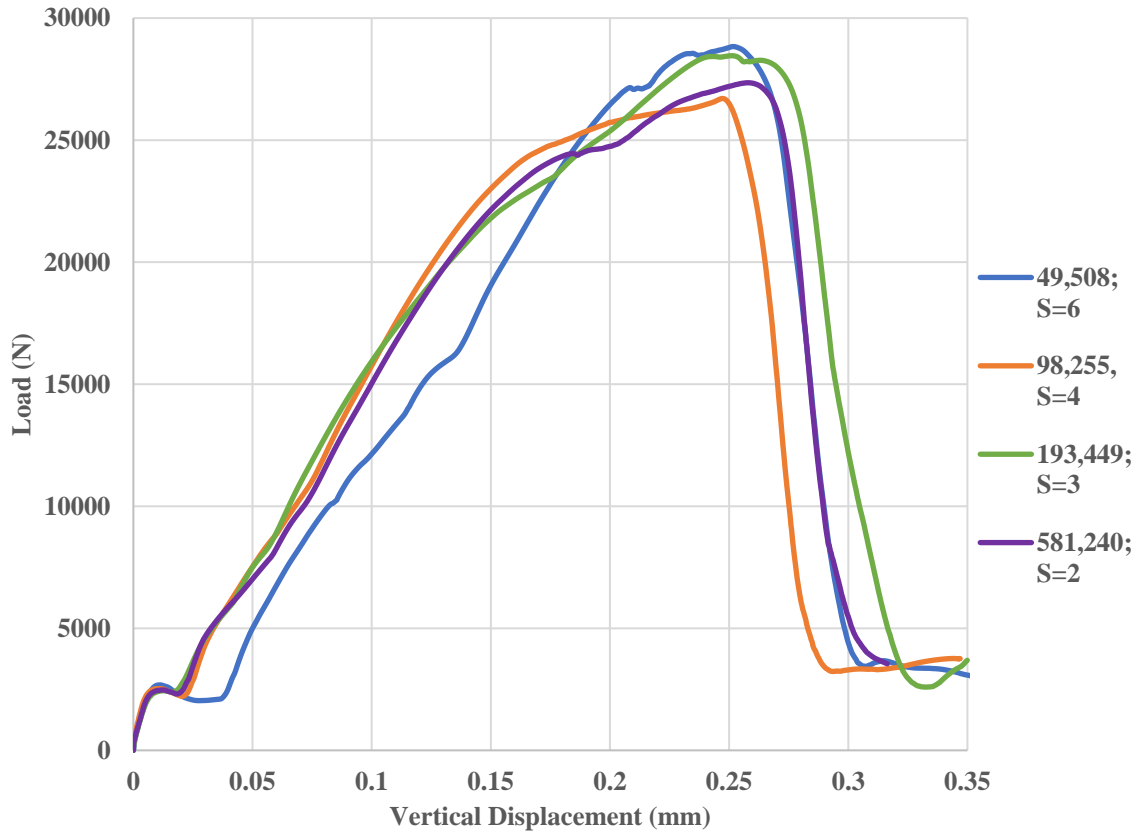
Figure 65: Results of mesh convergence study

The results of the investigation into the effects of the mass damping factor on the standard Brazilian indirect tension test are shown in Figure 66. Using no mass damping factor shows a large effect on the linearity of the elastic region, where energy impulses are allowed to complicate the simulation and result in a wavy effect in the elastic zone. Using a value of 10% to 100% of the calculated value (Eq. 3-16) shows a clear smoothing of these energy "waves". Using a value in this range also shows only a slight deviation from the peak load

and the effect doesn't have a huge effect on the overall shape of the curve. When using a value twice the calculated value the elastic region is stiffened, and the peak load occurs at a significantly lower vertical displacement and the shape of the curve is dramatically affected. For the models used in this work, a value of 10% was used for the mass damping factor to achieve the smoothing of the resultant curves.
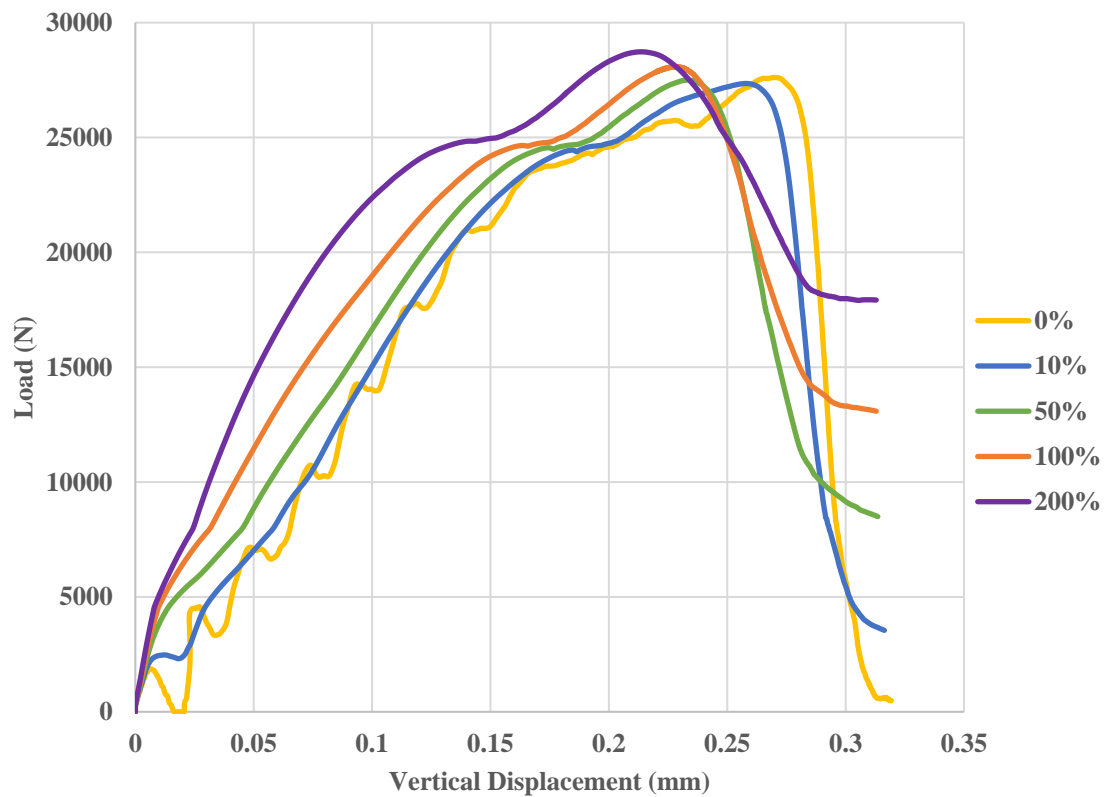
Figure 66: Results of mass damping coefficient study

4.3.3 Stiff Brazilian indirect tension test numerical results

The experimental results completed by Rusch et. al., (2018) on the stiff Brazilian indirect tension test are shown in Figure 67 and Figure 68. The profile of vertical displacement against load shows behavior that is indistinguishable from the standard Brazilian indirect tension test. The COD vs load also shows behavior that is in line with a standard Brazilian indirect tension test with a disk specimen diameter in this size range. Some of the elastic region in the experimental results of the COD vs load may be subject to noise from factors affecting the analysis of images during the DIC process.
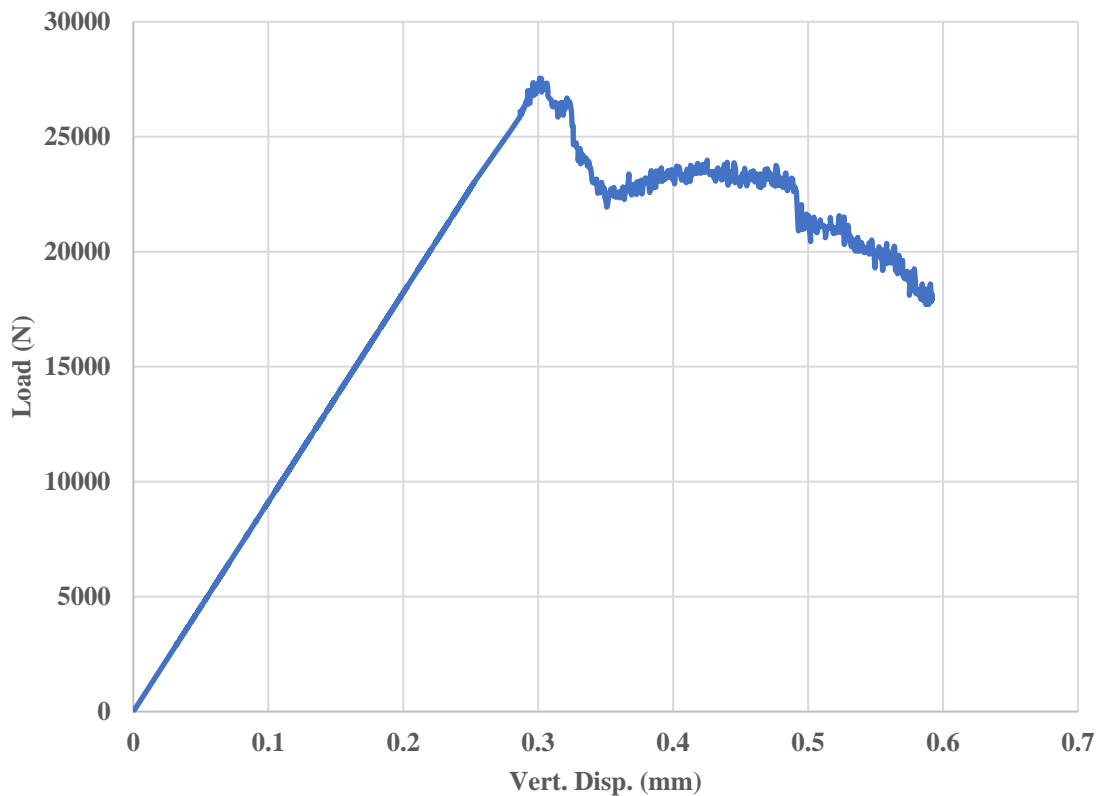
Figure 67: Vertical experimental results of stiff BITT (Rusch et. al., 2018)
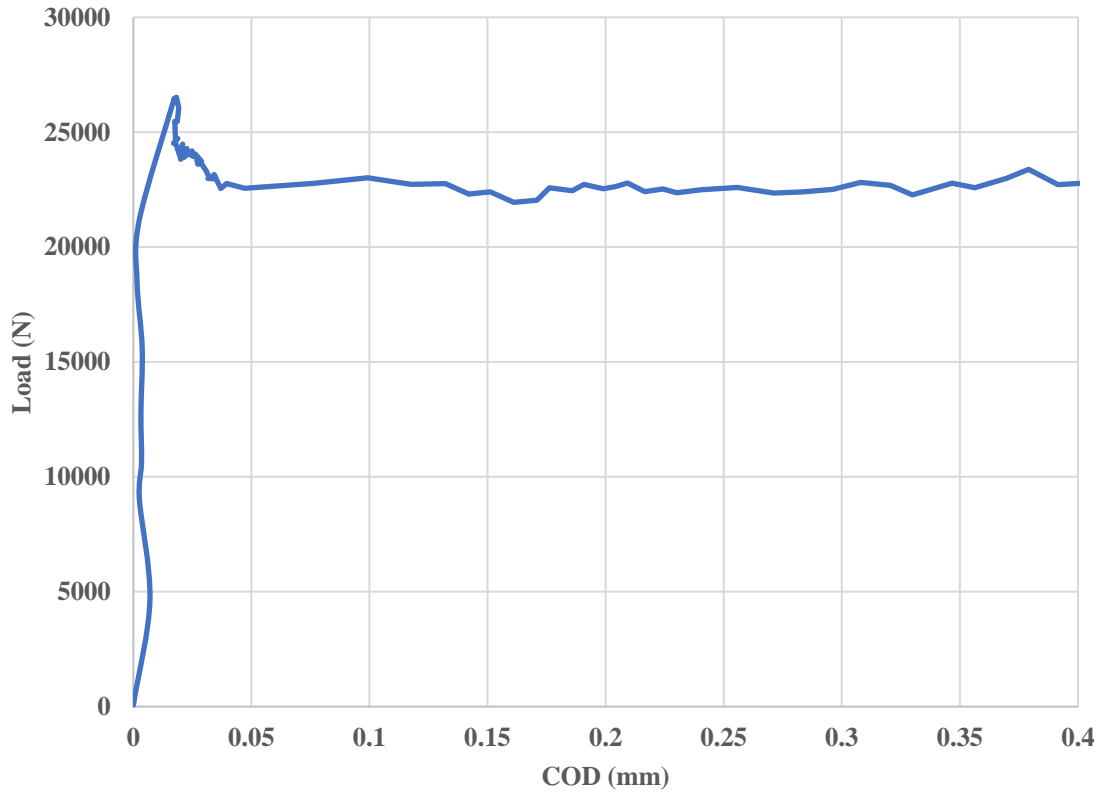
Figure 68: COD experimental results stiff BITT (Rusch et. al. 2018)

The model results of the stiff Brazilian indirect tension test are shown in Figure 69 to Figure 74. The vertical load displacement profile of the simulation observed in Figure 69 shows the model with a comparable stiffness and peak magnitude with what was seen in the experimental results. As with the standard Brazilian indirect tension test, the model of the stiff Brazilian indirect tension shows a more significant drop in load after failure than is seen in the experimental results. Again, the use of the wood at the contact points is one explanation for the discrepancy. The slow loading rate used in experimentation may also be contributing to the phenomena in which after failure the separated pieces are able to sustain the load.
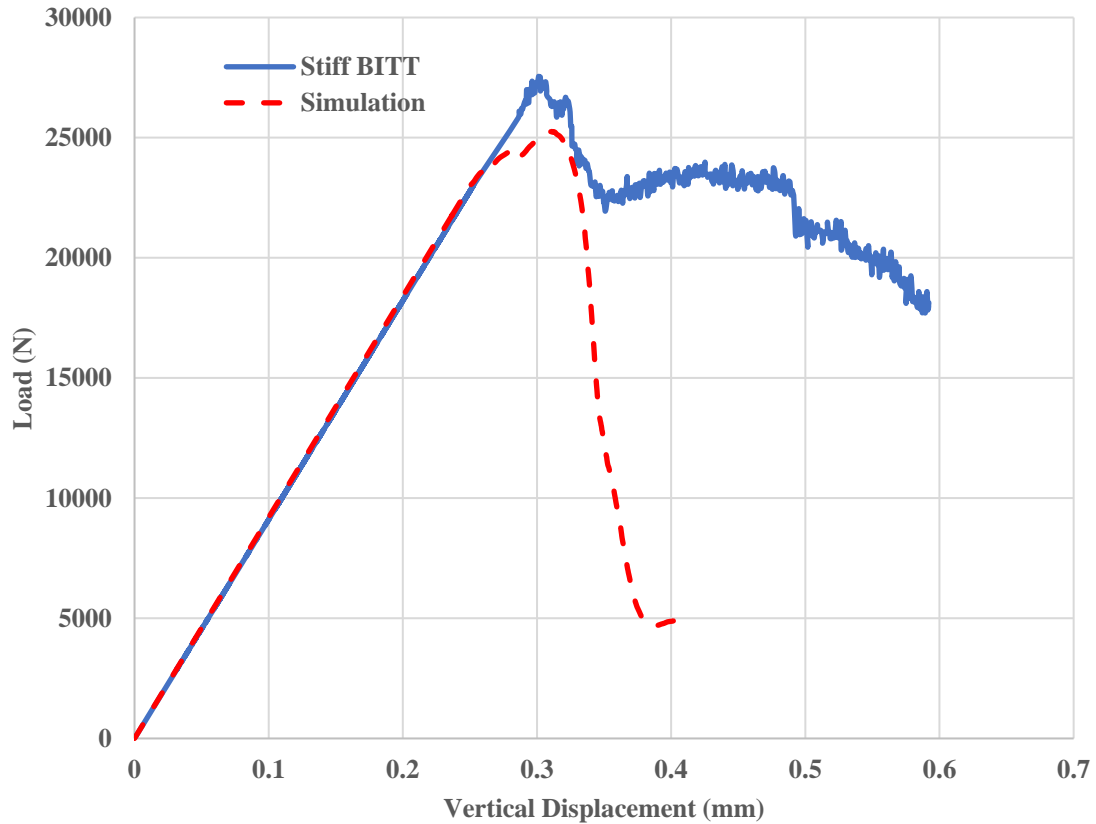
Figure 69: Model result of vertical load displacement stiff BITT

The COD versus load in the model as observed in Figure 70 appears to capture the overall stiffness of the lateral deformation before a fracture begins to propagate. The model results again display a more significant drop in load just after failure, which can be contributed to similar factors affecting the standard Brazilian indirect tension test results. The broken pieces of the disk under a slow load rate being kept together at the contact points with the wood supports in experimentation are able to sustain load while continuing to open at the center. The simulation sees more drop in load as the pieces quickly separate and are not able to uphold the load as two new separate pieces.

96
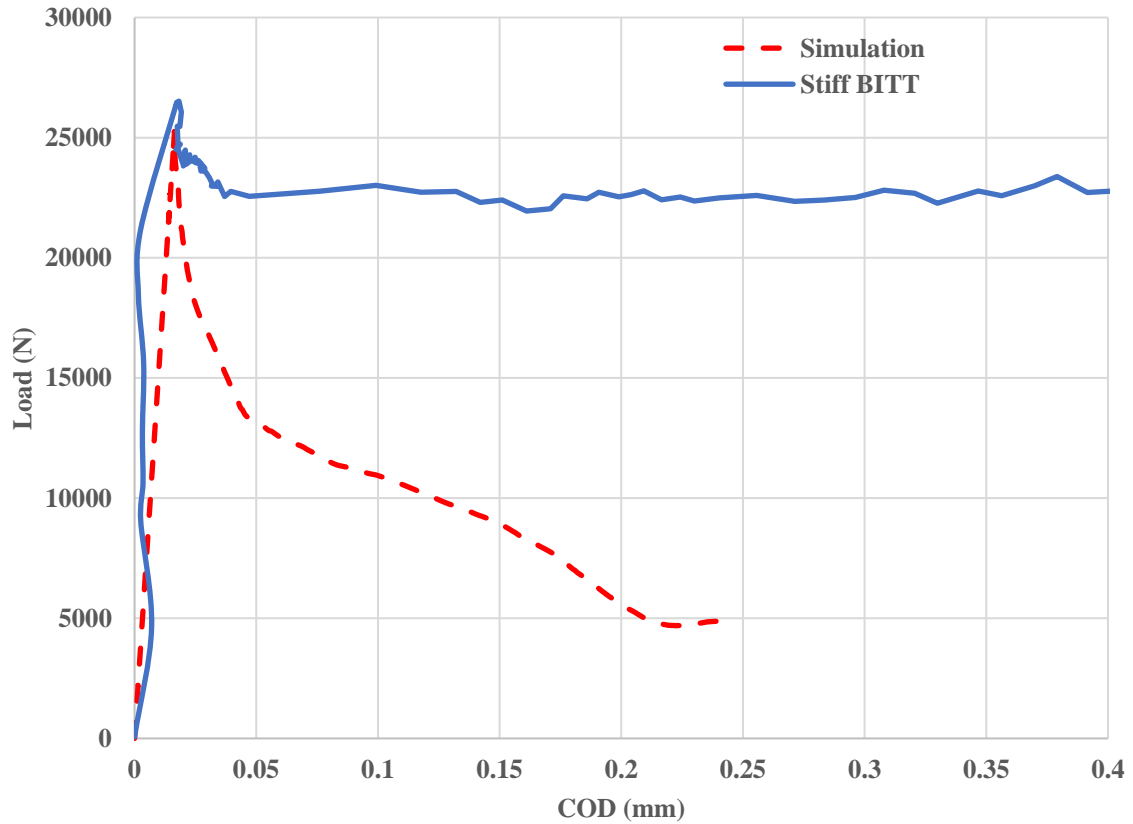
Figure 70: Model results COD vs load stiff BITT

The peak tensile stress profile in the x-direction shown in Figure 71 shows a similar profile as seen in the standard Brazilian indirect tension test. When viewing the tensile stresses, the same stress concentrations appear at the boundaries where compressive and tensile stresses meet within the sample. The stress profile in the y-direction, Figure 72, also shows the same column of compressive stresses in the center of the sample where the load is transferred between the two plates as seen in the standard Brazilian indirect tension test.
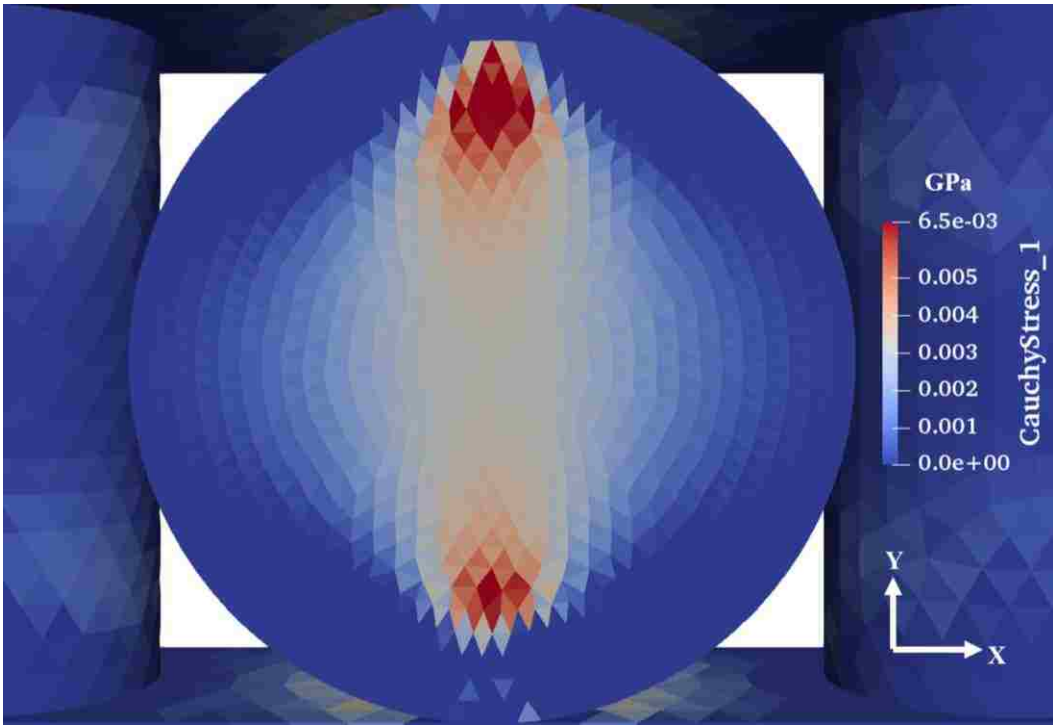
Figure 71:Model tensile stress profile in the x-direction stiff BITT
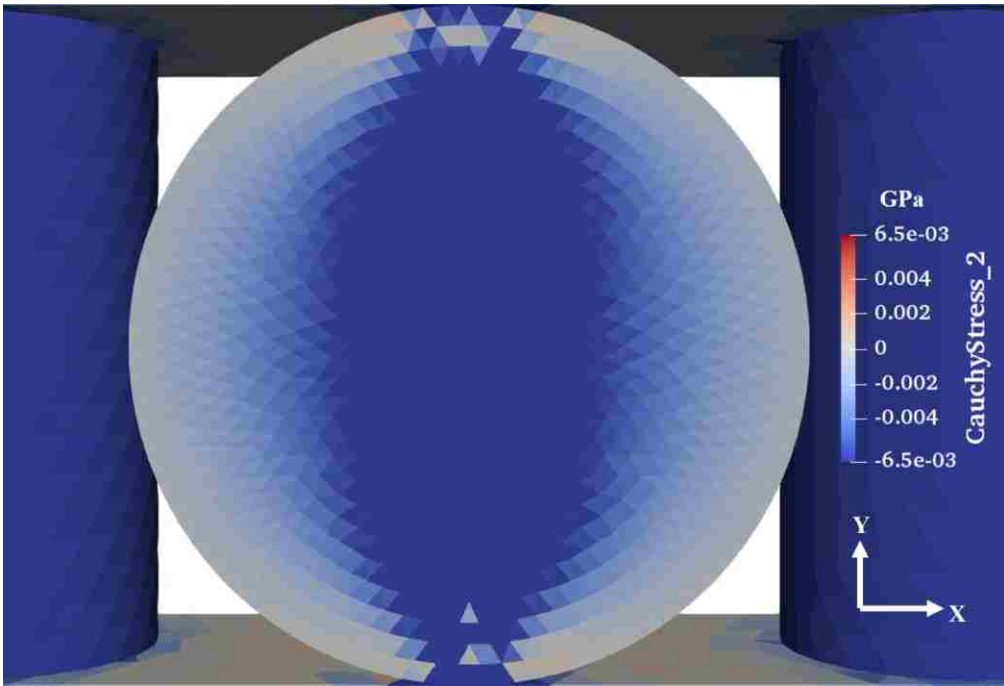
Figure 72: Model stress profile in the y-direction stiff BITT

The progression of damage, separation between elements, in the model can be seen in Figure 73 and Figure 74. The magnitude of the progression shows the damage starting at

the contact points developing from the top and stemming down to the bottom. The model also shows the damage at the contact points begin as mainly shear separations and develops into tensile separations as it branches down to the bottom of the sample. This damage progression is similar to what is seen in the standard Brazilian indirect tension model results.
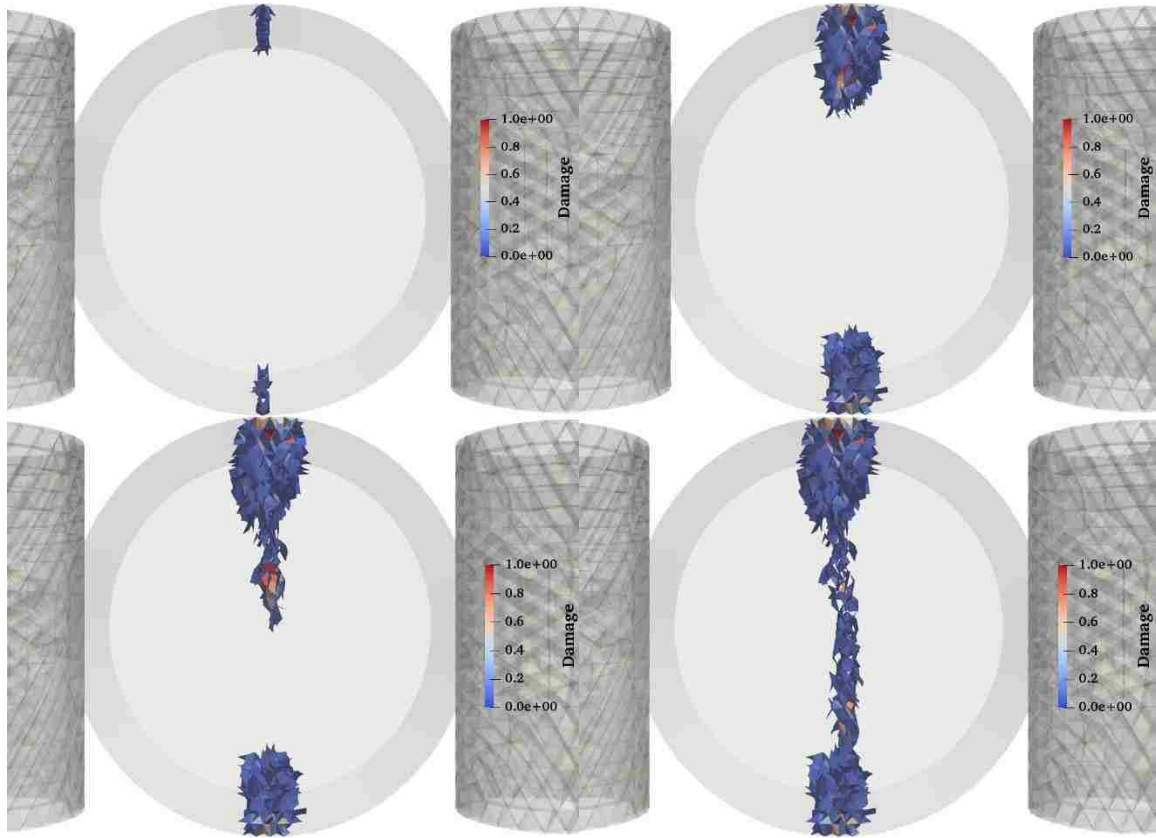
Figure 73: Model damage magnitude progression stiff BITT

Figure 74: Model damage type progression stiff BITT

These model results from the stiff Brazilian indirect tension test match closely with those observed in the model results for the standard Brazilian indirect tension test. The choice to use a curve from the standard Brazilian indirect tension test experimental results which matched closely to the stiff Brazilian indirect tension test experimental results likely contributed to this similarity as the same properties for the concrete tensile and shear strength were chosen for both models. Additionally, the mechanics principles observed within the disk are the same. The main difference between the two simulations is the total processing time. The standard Brazilian indirect tension test takes around 8 hours to

complete with the mesh size chosen, while the stiff Brazilian indirect tension test takes around 16 hours to complete with the same mesh size. Although the stiff Brazilian indirect tension test model uses more elements to represent the PVC supports than the standard Brazilian indirect tension test model, the additional elements are not significant enough to double the processing time. The added simulation time can be explained by the original principle for which the stiff Brazilian indirect tension test was designed, to slow the observance of the failure of the concrete disk. The standard Brazilian indirect tension test model shows the damage progression from initial to full fracture takes a simulation time of around 1.99ms while the stiff Brazilian indirect tension test model damage progression occurs in around 2.8ms. This time difference can amount to critical seconds added to the experimental Brazilian indirect tension test which can allow for more permeability measurements to be made.

Figure 75 shows the model results of the load share between the concrete disk and the PVC supports. The results show that the PVC with the input elastic modulus and resultant stiffness holds around 30% of the load, while the concrete disk holds around 70% of the load, these results are consistent with what is seen in experimental results seen by Rusch et.al., (2018). Initially, the PVC catches the load first and as the concrete disk receives load, the load share ebbs between the two and the concrete begins to hold a higher and higher portion. As the elastic portion of the test fully onsets the load share evens out at a 70/30 distribution. At the onset of damage and stiffness changes in the sample the PVC begins to take on more percentage of the load and the percent to the concrete decreases.
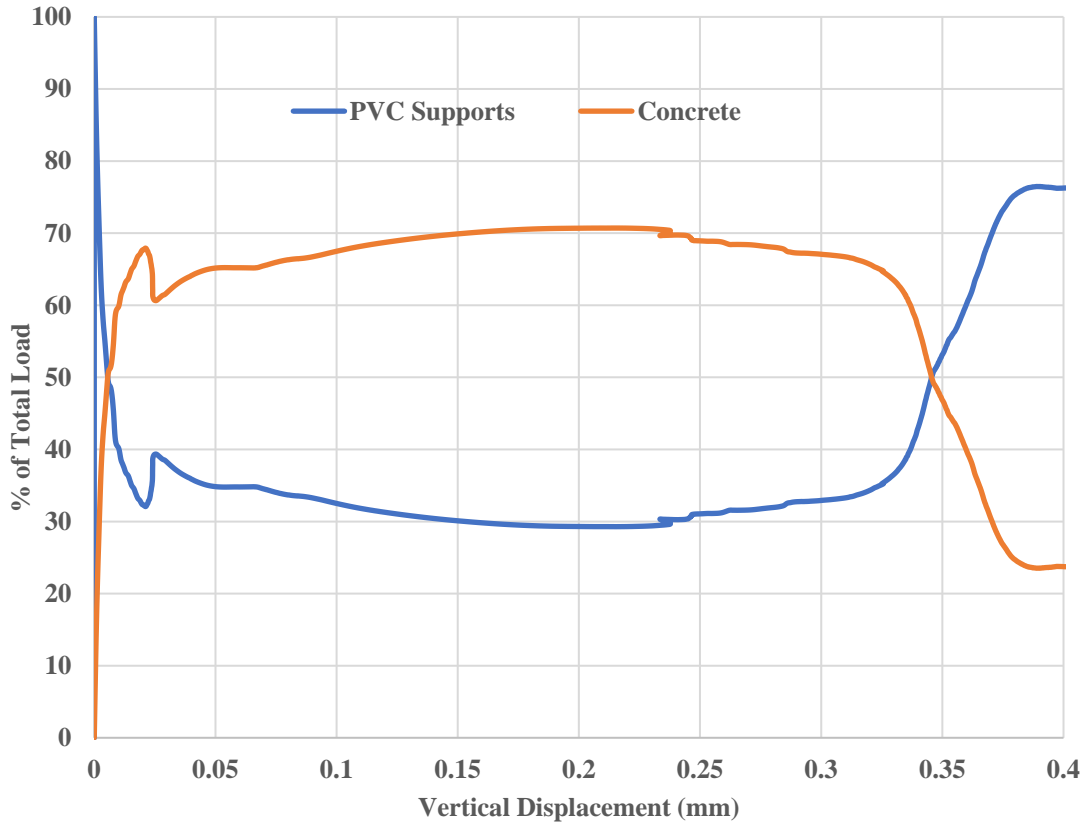
Figure 75: Model results of load share between concrete disk and PVC supports

4.3.4 Pre-damaged stiff Brazilin indirect tension test model results

The simulation results from the pre-damaged stiff Brazilian indirect tension test are shown in Figure 76 to Figure 82. The profile of vertical load displacement in the simulation captures the overall non-linear phenomena seen in the experimental results. This non-linear stiffness is followed by a drop-in load, which again is more significant than what is seen in experimentation. The experiment again utilized the wood pieces and the slow load rate which can help explain the less significant drop in load seen in experimentation. Additionally, in this sample there was a second fracture line which developed at the bottom

of the sample which could have also contributed to the difference. The peak load seen in

the model matches well with what is observed in experimentation and occurs at a similar

vertical displacement despite being modeled with only one main fracture line.
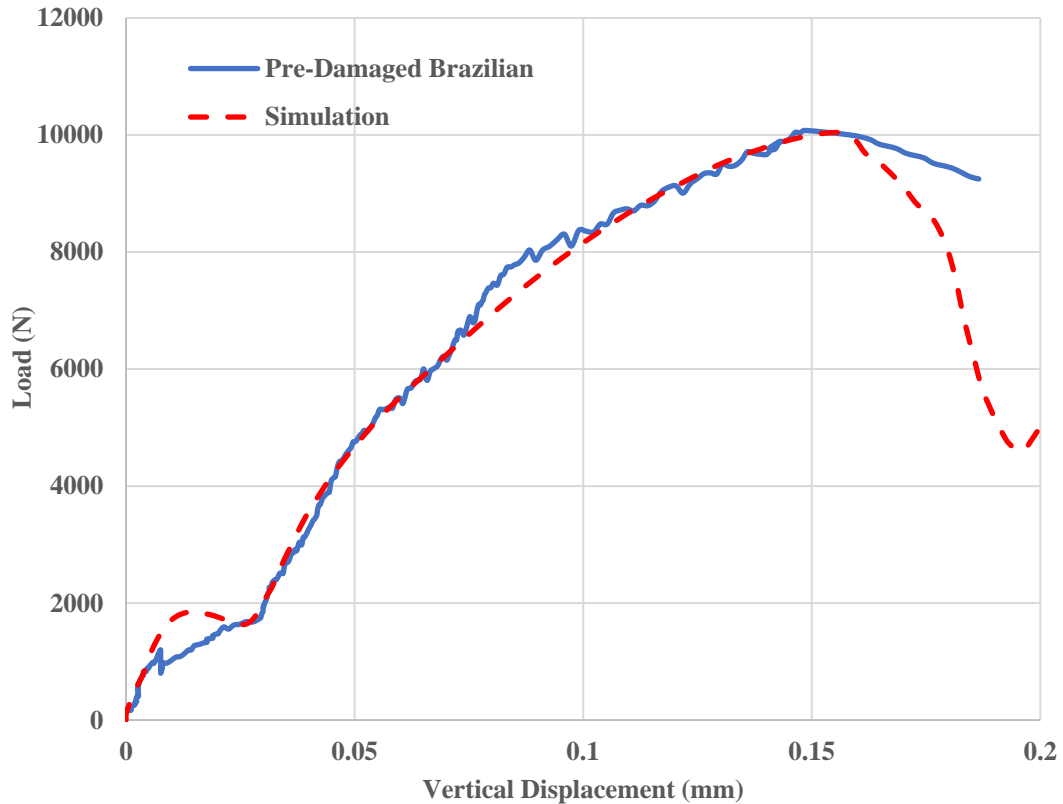
Figure 76: Model result of vertical displacement pre-damaged SBITT

The COD vs load profile of the pre-damaged model shown in Figure 77 shows good

agreement with the experimental results. The simulation captures the initial linear lateral

stiffness before a non-linear opening and separation at around 2 kN. The model then shows

continued opening with increasing load until around 10kN, where the model begins to drop

in load significantly as the cohesion between the two sample pieces has reached a critical

point. In experimentation the load drops less significantly after having reached a peak load.

This can be explained by the initiation of critical fractures having initiated within the

sample at the stress level associated with the load within the sample. Again, in experimentation the slow load rate and wooden contacts may be a large factor contributing to the more sustained load after critical this critical load.
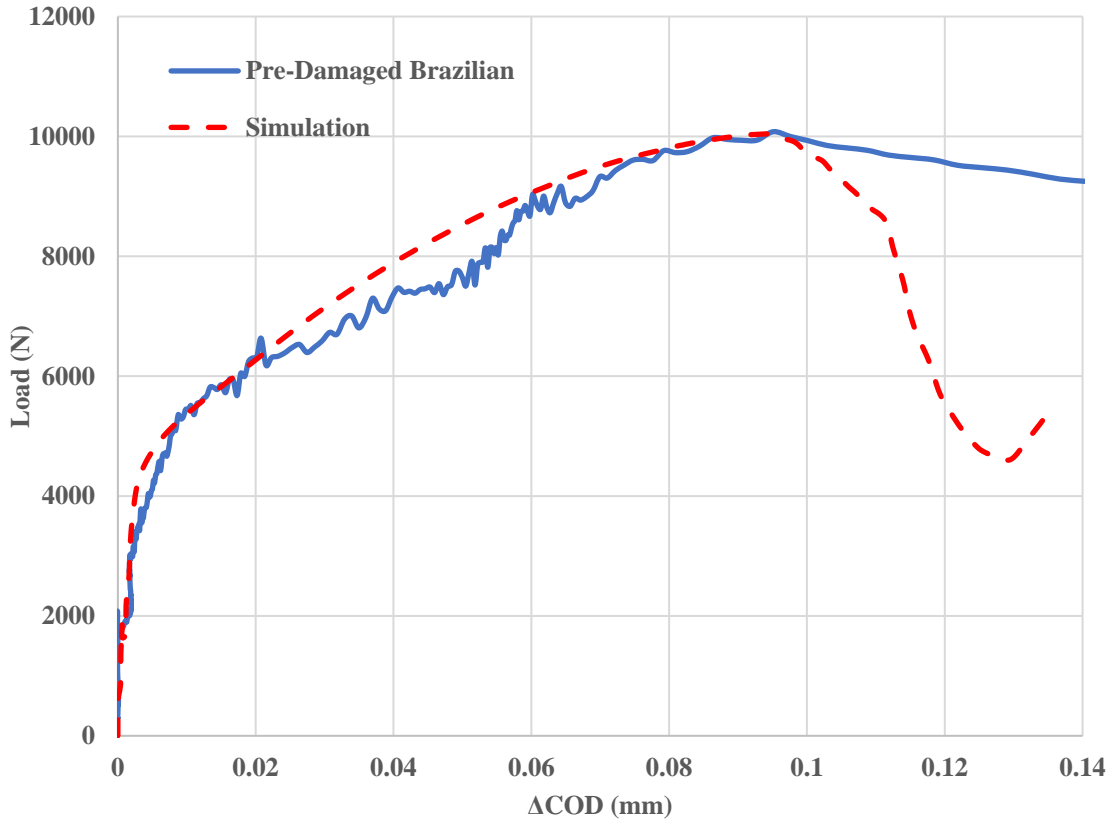
Figure 77: Model result of change in COD pre-damaged SBITT

The pre-damaged tensile stress profile in the x-direction can be seen in Figure 76. The sample shows a similar stress shape as shown in both the standard and stiff Brazilian indirect tension test models, although at an expected much lower stress level. The tensile strength assigned to the fracture group within the model again is 10% of the strength assigned to the concrete specimen halves of 5.5 MPa. It can be observed that again two critical areas of stress appear at the boundary between the tensile and compressive stresses within the sample.
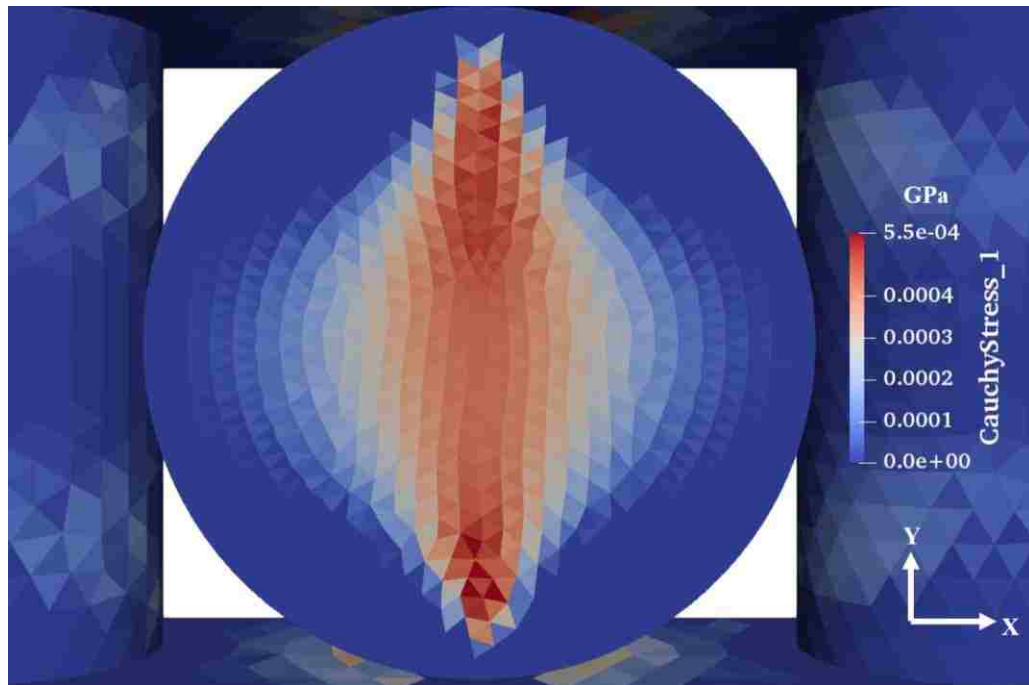
Figure 78: Model result tensile stress profile in x-direction pre-damaged stiff BITT

In the y-direction the compressive stresses develop within the sample in a similar fashion as observed in the other two models, apart from concentrations of compressive stresses at certain areas within the sample. These concentrations are likely due to the shape of the fracture and the corresponding interaction of the two halves of the disk as the load is transferred between the plates. Figure 79 shows the before and after cohesion separation of the elements belonging to the cracked group of the stresses in the y-direction. It can be observed that after full separation the two pieces begin to act independently, with the right half taking more load. The pieces are also subject to tensile stresses along the circumference and compressive stresses along the fracture line. This stress profile of the two separated pieces may be an indication of how the specimens hold a higher load when displaced at a slower rate and kept from easily separating at the contact points.
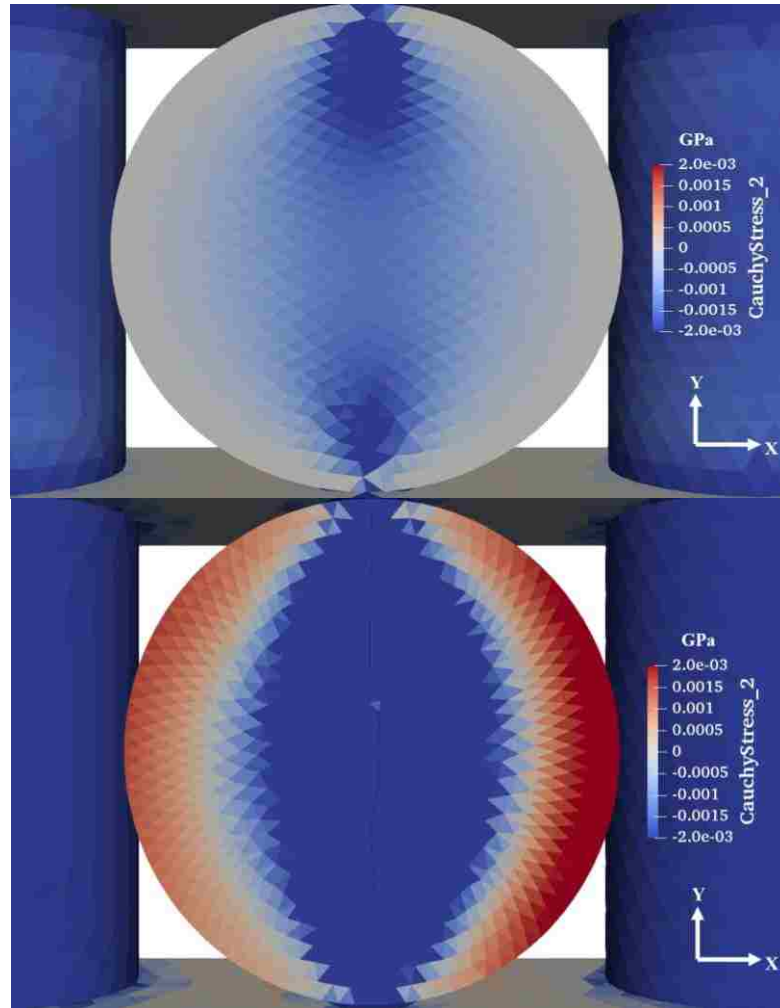
Figure 79: Model result stress profiles in y-direction before and after separation

The progression of damage in the pre-damaged model is shown in Figure 80 to Figure 82. The magnitude of the progression shows initial separations occurring near the contact points with a quick progression into the already existing fracture line, followed by additional separations occurring at the contact points. From Figure 82, a side view of the damage type progression, it can be observed that the initial separations and those near the contact points are due to shear, while tensile separations characterize the fracture line.

106
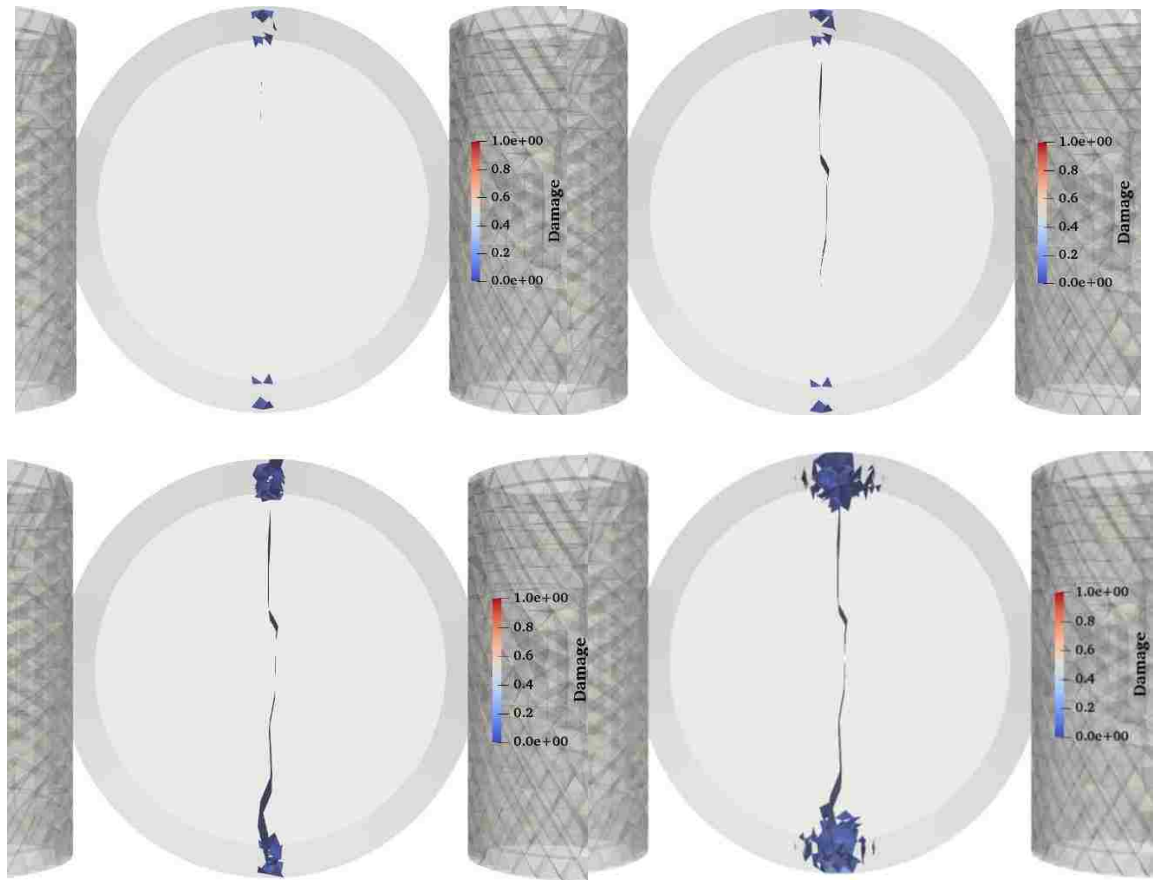
Figure 80: Progression of damage magnitude in pre-damaged model front-view
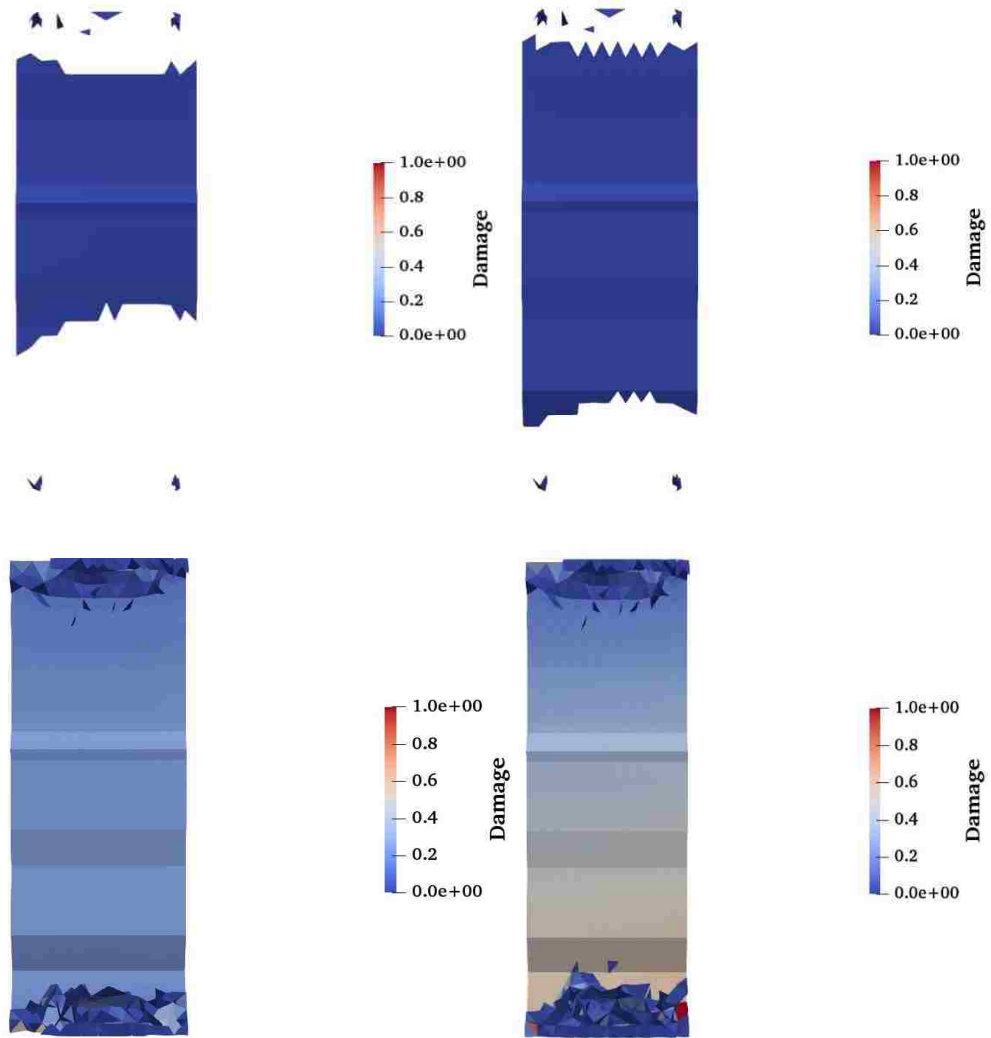
Figure 81: Model damage magnitude progression pre-damaged stiff BITT side-view
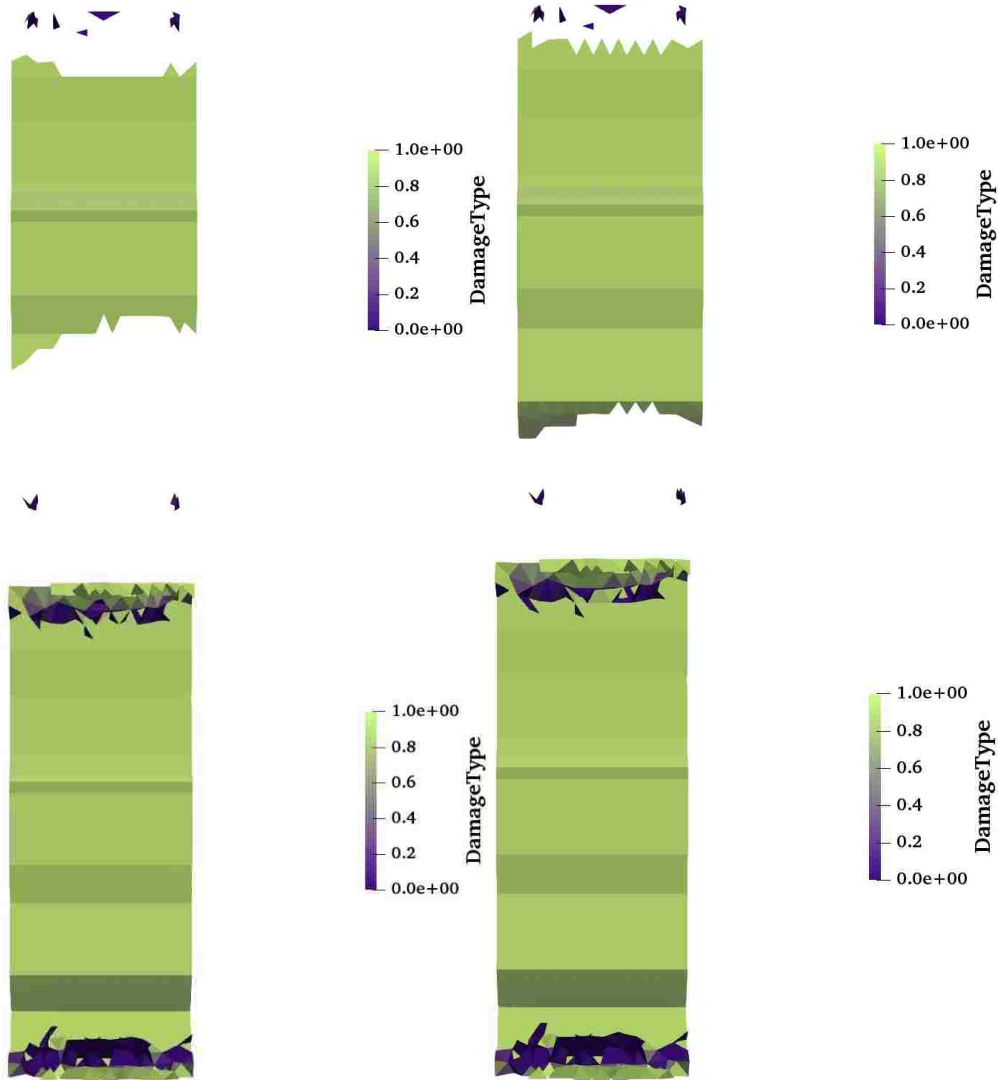
Figure 82: model damage type progression pre-damaged stiff BITT side-view

The results of the investigation into the percentage of tensile and shear strength belonging to the elements in the cracked group are shown in Figure 83 and Figure 84. The vertical load displacements, Figure 83, and the COD vs load, Figure 84, both show similar differences between the percentages used. All percentages observe similar shape behavior and tendencies. However, as the percentage is decreased the peak load reduces and the vertical displacement at the time of peak load decrease. The COD of the peak load also reduces as you decrease the percentage of strengths used.
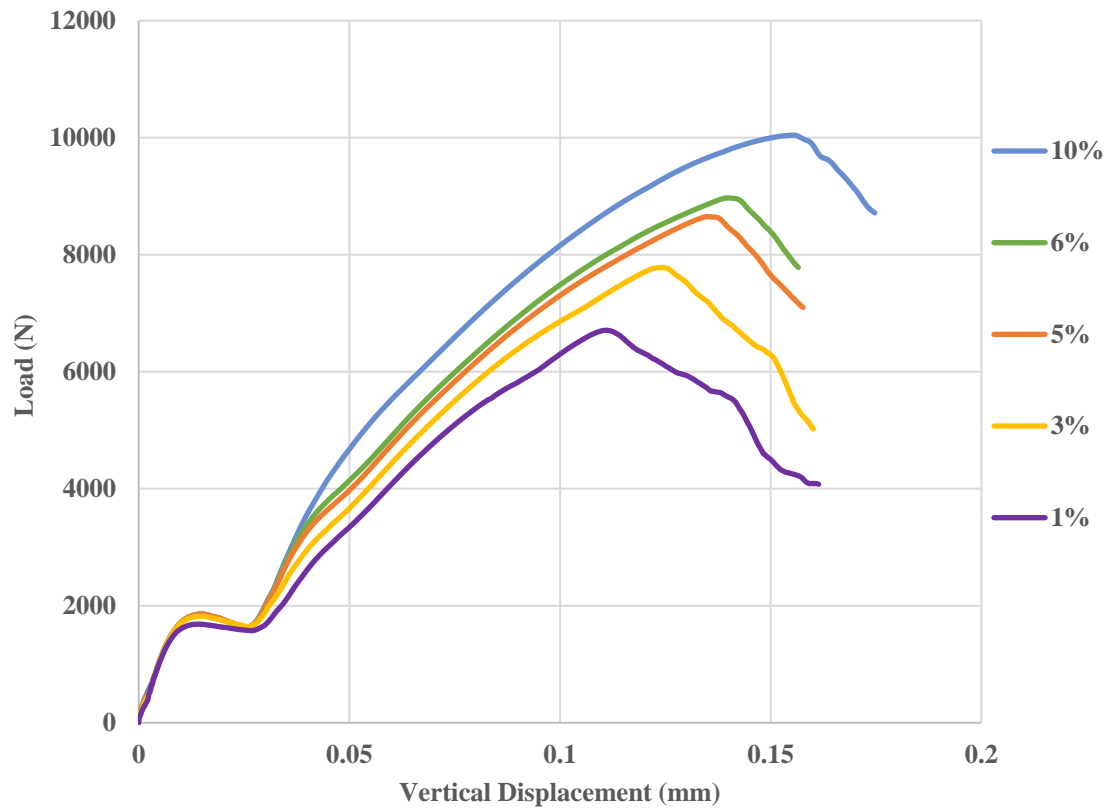
Figure 83: Results of tensile and shear strength comparison: Vertical load displacement
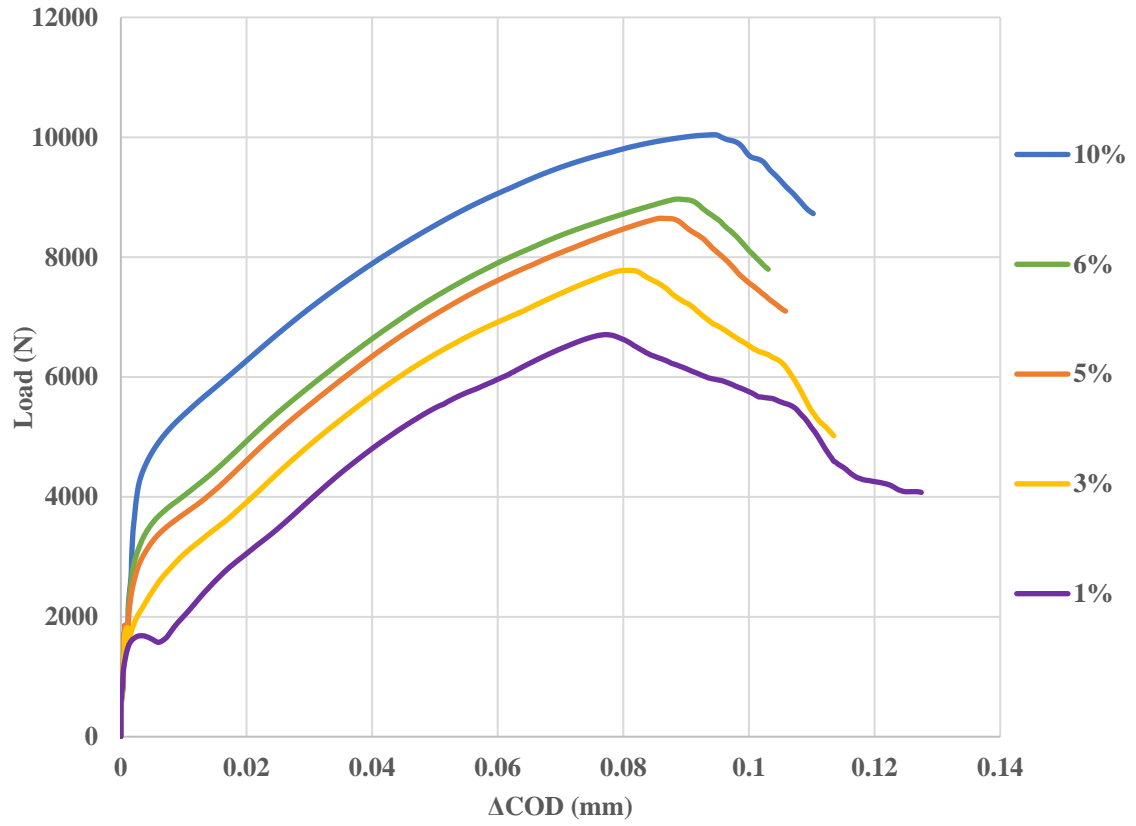
Figure 84: Results of tensile and shear strength comparison: COD

CHAPTER 5 | CONCLUSIONS

5.1 Conclusions

An in-depth investigation was made into the damage mechanisms present in the standard Brazilian indirect tension test and modifications made using the stiff Brazilian indirect tension test set-up using FDEM and parallel computing methods. Validation and investigation into a pre-damaged specimen and a preliminary study into the effects of a proposed circumferential rubber sleeve were also made. The main conclusions put forth as a result of these investigations are stated below:

- The effect of the rubber sleeve on the Brazilian indirect tension test resulted in behaviors which added further complications to the correlation process. The use of the circumferential rubber sleeve was suspended in favor of other seemingly less intrusive options.

- The methodology behind the stiff Brazilian indirect tension test set-up was validated. The model and experimental results being in good agreement show that the principle behind the set-up is valid. With the validated model the relationship between stiffnesses of the support system and disk sample can be calibrated to achieve desired load shares. The system shows potential to slightly slow down damage progression. It's not clear from this sample size what the exact time addition would be or if the system would have any meaningful effect on more homogeneous materials like granite which tend to have even more sudden failures while the effect may be amplified in concrete with larger aggregates.

112

- According to the progression of damage seen in all 3 models the use of the cubic law doesn't appear to be a valid assumption for the initial occurrences of damage. If the stiff Brazilian indirect tension test achieved an ideal delayed damage progression, according to the results of the models the parallel plate theory should not be assumed, instead a method using fracture or separation densities would be more representative for these early stages of interest. After a full fracture has formed, then the cubic law assumptions can be used as a starting point if the sample exhibits one main fracture line. These results indicate that the permeability set-up needs to capture initial matrix and pore permeability, intermediate damage progressions which may or may not exhibit changes in permeability, and post peak hydraulic aperture widening.

- This study also validates the use of HOSS as a competent FDEM platform for future investigations into further modifications that may be made to the Brazilian indirect tension test. It also shows the ability of this FDEM method to simulate existing damage and fractures within a sample and the resulting behavior.

5.2 Limitations of Study & Future Work

The limitations present within this study stem from both experimental and numerical confines. In experimentation the ability to properly capture displacements in the vertical and horizontal directions during the Brazilian indirect tension test are cumbersome, especially with the use of an attached system on one face to capture flow and permeability

changes. Using DIC is the less intrusive option but still presents difficulties in analysis. During testing there are small rotations of the sample, which effect the total displacement measures made by tracking the movement of a group of pixels. Additionally, great care needs to be taken when analyzing the displacement of the sample to ensure that the true displacement is recorded and not the simply the movement of the pixels. These effects will increase the overall displacements seen in the experimental results. Additionally, the effect of the wood bearing strips needs further investigation. There may also be effects from the method chosen for monitoring permeability changes, where one face may be being constrained by the use of AT-200Y vacuum tape and funnel attachment. The specimen size chosen may also have an effect and may not be the ideal size to represent a good datum for interpretations to large lithologies of rock and concrete structures. It is also known that humidity and temperature effect the tensile strength of concrete and rock as does the procedure behind the molding and curing of the concrete. (Minh Phong Luong, 1990). These considerations were not considered in the present study, however the nature of the FDEM code used allows for dynamic input of the tensile and shear strengths and softening behavior which can be experimentally calibrated to fit differing experimental results.

Within the FDEM code used one main limitation is the inability to modestly use slow loading rates. The viable solutions to this are currently addressed by using either the mass damping factor as explained or having simulations which can take several weeks to complete. For developing experimentation, it is not ideal to use a model which may take a substantial amount of time necessary to give meaningful interpretive results. It is also not known what the full of effect of the mass damping factor entails. The brief study indicates that the effect, when using around 10%-100% the calculated value, is limited to smoothing

out the elastic and peak region of the curve. It is not known whether a correlation can be made for the mass damping factor to known loading rates in experimentation and so it cannot be stated with certainty that the model is exhibiting the exact loading rate. However, the validated model results show good agreement with the behavior seen in experimentation using a 10% value of the calculated mass damping factor. Additionally, the model is representing a homogeneous material before fracture occurs and does not take into account the aggregate variations present in concrete.

It should also be noted that the damage model used in this study does not consider the more nuanced fracture mechanics unique to concrete and other quasi-brittle materials. The model uses an approach which assumes a direct material tensile strength as observed in materials like steel. However, concrete tensile strength depends on many factors including mechanism, humidity, density, and curing processes. Because of these factors the material specific energy, G_I, will be unique to each portion of the specimen and results in concrete exhibiting a wide range of values. Additionally, the common methods used to determine a relative value for the tensile strength of concrete depend on the purpose for the value including modulus of rupture, determined through bending, direct tension, and indirect tension in the form of the Brazilian indirect tension test. (Minh Phong Luong, 1990). Even with an idealized direct tension test the factors of density, curing procedure and humidity all become more apparent. (Kim and Reda Taha, 2014). In this study a value for tensile and shear strength was chosen to adequately exhibit the peak load seen in experimentation within the model.

Future experimental work can include the use of acoustic emissions to audibly track the early onset damage currently not visible with DIC or permeability measures. Investigation

115

into the damage progression exhibited within disk specimens subject to different loading rates, boundary conditions and specimen sizes would also aid in creating a map for future damage correlations with permeability. Future investigations using FDEM can include the introduction of various fractures throughout the disk specimen at varying densities to observe effects on damage progression as well as observing the effects of displacement rate, boundary conditions and specimen size.

The fluid solver being developed within the FDEM platform HOSS will need to calibrate within the damage model the separation at which a difference in flow is to be allowed. The solver may also need to consider overall densities of damage rather than single elemental separations. For the Brazilian indirect tension test the model will need to account for initial matrix permeabilities, initial damage progressions for which the cubic law may not suffice, and the permeability associated with hydraulic fracture apertures and widening.

REFERENCES

Abeele, K.E.-A.V.D., Johnson, P.A., and Sutin, A. (2000). Nonlinear Elastic Wave Spectroscopy (NEWS) Techniques to Discern Material Damage, Part I: Nonlinear Wave Modulation Spectroscopy (NWMS). Res. Nondestruct. Eval. *12*, 17–30.

Arson, C., and Pereira, J.-M. (2012). Influence of damage on pore size distribution and permeability of rocks. Int. J. Numer. Anal. Methods Geomech. *37*, 810–831.

Atkinson, B. (1984). Subcritical crack growth in geological materials. J. Geophys. Res. Solid Earth *89*, 4077–4114.

Atkinson, C., Smelser, R.E., and Sanchez, J. (1982). Combined mode fracture via the cracked Brazilian disk test. Int. J. Fract. *18*, 279–291.

Bažant, Z.P. (2000). Size effect. Int. J. Solids Struct. *37*, 69–80.

Bažant, Z.P. (2002). Concrete fracture models: testing and practice. Eng. Fract. Mech. *69*, 165–205.

Bernabé, Y., Mok, U., and Evans, B. (2003). Permeability-porosity Relationships in Rocks Subjected to Various Evolution Processes. Pure Appl. Geophys. *160*, 937–960.

Boller, C. (2000). Next generation structural health monitoring and its integration into aircraft design. Int. J. Syst. Sci. *31*, 1333–1349.

Bowden, F.P., and Field, J.E. (1964). The brittle fracture of solids by liquid impact, by solid impact, and by shock. Proc R Soc Lond A *282*, 331–352.

Brace, W.F., Walsh, J.B., and Frangos, W.T. (1968). Permeability of granite under high pressure. J. Geophys. Res. *73*, 2225–2236.

Cervera, M., and Chiumenti, M. Smeared crack approach: back to the original track. Int. J. Numer. Anal. Methods Geomech. *30*, 1173–1199.

Chaboche, J.L. (1988). Continuum Damage Mechanics: Part II—Damage Growth, Crack Initiation, and Crack Growth. J. Appl. Mech. *55*, 65–72.

Cundall, P.A. (1988a). Computer Simulations of Dense Sphere Assemblies. In Studies in Applied Mechanics, M. Satake, and J.T. Jenkins, eds. (Elsevier), pp. 113–123.

Cundall, P.A. (1988b). Formulation of a three-dimensional distinct element model—Part I. A scheme to detect and represent contacts in a system composed of many polyhedral blocks. Int. J. Rock Mech. Min. Sci. Geomech. Abstr. *25*, 107–116.

Dai S. T., and Labuz J. F. (1997). Damage and Failure Analysis of Brittle Materials by Acoustic Emission. J. Mater. Civ. Eng. *9*, 200–205.

Erarslan, N., and Williams, D.J. (2012). Experimental, numerical and analytical studies on tensile strength of rocks. Int. J. Rock Mech. Min. Sci. *49*, 21–30.

Evans, A.G., Gulden, M.E., and Rosenblatt, M. (1978). Impact damage in brittle materials in the elastic-plastic response régime. Proc R Soc Lond A *361*, 343–365.

Evans, A.G., Ito, Y.M., and Rosenblatt, M. (1980). Impact damage thresholds in brittle materials impacted by water drops. J. Appl. Phys. *51*, 2473–2482.

Griffith, A.A. (1924). The theory of rupture. Proc First Int Congr Appl Mech 56–63.

Hillerborg, A., Modéer, M., and Petersson, P.-E. (1976). Analysis of crack formation and crack growth in concrete by means of fracture mechanics and finite elements. Cem. Concr. Res. *6*, 773–781.

Holcomb, D.J., and Costin, L.S. (1986). Detecting Damage Surfaces in Brittle Materials Using Acoustic Emissions. J. Appl. Mech. *53*, 536–544.

Homand-Etienne, F., Hoxha, D., and Shao, J.F. (1998). A continuum damage constitutive law for brittle rocks. Comput. Geotech. *22*, 135–151.

Huang, Y., Liu, C., and Stout, M.G. (1996). A Brazilian disk for measuring fracture toughness of orthotropic materials. Acta Mater. *44*, 1223–1232.

Ishida, T., Chigira, M., and Hibino, S. (1987). Application of the Distinct Element Method for analysis of toppling observed on a fissured rock slope. Rock Mech. Rock Eng. *20*, 277–283.

Jenq Yeoushang, and Shah Surendra P. (1985). Two Parameter Fracture Model for Concrete. J. Eng. Mech. *111*, 1227–1241.

Jiang, T., Shao, J.F., Xu, W.Y., and Zhou, C.B. (2010). Experimental investigation and micromechanical analysis of damage and permeability variation in brittle rocks. Int. J. Rock Mech. Min. Sci. *47*, 703–713.

Kim, J.J., and Reda Taha, M. (2014). Experimental and Numerical Evaluation of Direct Tension Test for Cylindrical Concrete Specimens.

Krajcinovic, D., and Fonseka, G.U. (1981). The Continuous Damage Theory of Brittle Materials, Part 1: General Theory. J. Appl. Mech. *48*, 809–815.

L. R. Lenke and W. H. Gerstle (2001). Tension Test of Stress Versus Crack Opening Displacement Using Cylindrical Concrete Specimens. Spec. Publ. *201*.

Landis Eric N., and Baillon Lucie (2002). Experiments to Relate Acoustic Emission Energy to Fracture Energy of Concrete. J. Eng. Mech. *128*, 698–702.

Lemaitre, J., and Chaboche, J.-L. (1994). Mechanics of Solid Materials (Cambridge University Press).

Li, D., and Wong, L.N.Y. (2013). The Brazilian Disc Test for Rock Mechanics Applications: Review and New Insights. Rock Mech. Rock Eng. *46*, 269–287.

Lockner, D. (1993). The role of acoustic emission in the study of rock fracture. Int. J. Rock Mech. Min. Sci. Geomech. Abstr. *30*, 883–899.

Mahabadi O. K., Lisjak A., Munjiza A., and Grasselli G. (2012). Y-Geo: New Combined Finite-Discrete Element Numerical Code for Geomechanical Applications. Int. J. Geomech. *12*, 676–688.

Maso, J.C. (1982). "La liaison pâte-granulats." béton hydraulique, connaissance et pratique (Paris, France).

Mazars, J., and Pijaudier-Cabot, G. (1989). Continuum Damage Theory—Application to Concrete. J. Eng. Mech. *115*, 345–365.

Minh Phong Luong (1990). Tensile and shear strengths of concrete and rock. Eng. Fract. Mech. *35*, 127–135.

Munjiza, A. (2004). The Combined Finite-Discrete Element Method (New York: Wiley).

Munjiza, A. (2013). HOSS: An integrated platform for discontinua simulations. In Frontiers of Discontinuous Numerical Methods and Practical Simulations in Engineering and Disaster Prevention, (London: Taylor & Francis Group), pp. 97–100.

Munjiza, A., and Rougier, E. (2010). MRCK 3D CONTACT DETECTION ALGORITHM. Fifth Int. Conf. Discrete Elem. Methods.

Munjiza, A., Andrews, K.R.F., and White, J.K. (1999). Combined single and smeared crack model in combined finite-discrete element analysis. Int. J. Numer. Methods Eng. *44*, 41–57.

Munjiza, A., Knight, E.E., and Rougier, E. (2015). Large Strain Finite Element Method: A Practical Course (John Wiley & Sons).

Munjiza A., and Andrews K. R. F. (1998). NBS contact detection algorithm for bodies of similar size. Int. J. Numer. Methods Eng. *43*, 131–149.

Munjiza A., and Andrews K. R. F. (2000). Penalty function method for combined finite–discrete element systems comprising large number of separate bodies. Int. J. Numer. Methods Eng. *49*, 1377–1396.

Munjiza A., Latham J. P., and Andrews K. R. F. (2000). Detonation gas model for combined finite-discrete element simulation of fracture and fragmentation. Int. J. Numer. Methods Eng. *49*, 1495–1520.

Munjiza A., Latham J. P., and John N. W. M. (2002). 3D dynamics of discrete element systems comprising irregular discrete elements—integration solution for finite rotations in 3D. Int. J. Numer. Methods Eng. *56*, 35–55.

Mustoe, G., and Williams, J.R. (1989). In Proceedings 1st U.S. Conference on Discrete Element Methods, (Golden, CO), p.

O'Brien, T.K. (1980). Stiffness Change as a Nondestructive Damage Measurement. In Mechanics of Nondestructive Testing, (Springer, Boston, MA), pp. 101–121.

Oda, M., Takemura, T., and Aoki, T. (2002). Damage growth and permeability change in triaxial compression tests of Inada granite. Mech. Mater. *34*, 313–331.

Osthus, D., Godinez, H.C., Rougier, E., and Srinivasan, G. (2018). Calibrating the stress-time curve of a combined finite-discrete element method to a Split Hopkinson Pressure Bar experiment. Int. J. Rock Mech. Min. Sci. *106*, 278–288.

Read, H.E., and Hegemier, G.A. (1984). Strain softening of rock, soil and concrete — a review article. Mech. Mater. *3*, 271–294.

Reifsnider, K.L., and Highsmith, A. (1982). The Relationship of Stiffness Changes in Composite Laminates to Fracture-Related Damage Mechanisms. In Fracture of Composite Materials, (Springer, Dordrecht), pp. 279–290.

Scholz, C. (1972). Static fatigue of quartz. J. Geophys. Res. *77*, 2104–2114.

Shah, S.P., Swartz, S.E., and Ouyang, C. (1995). Fracture Mechanics of Concrete: Applications of Fracture Mechanics to Concrete, Rock and Other Quasi-Brittle Materials (John Wiley & Sons).

Shao, J.F., Zhou, H., and Chau, K.T. Coupling between anisotropic damage and permeability variation in brittle rocks. (2005). Int. J. Numer. Anal. Methods Geomech. *29*, 1231–1247.

Souley, M., Homand, F., Pepa, S., and Hoxha, D. (2001). Damage-induced permeability changes in granite: a case example at the URL in Canada. Int. J. Rock Mech. Min. Sci. *38*, 297–310.

Walsh, P.F. (1976). Crack initiation in plain concrete. Mag. Concr. Res. *28*, 37–41.

Wang, Q.-Z., and Xing, L. (1999). Determination of fracture toughness KIC by using the flattened Brazilian disk specimen for rocks. Eng. Fract. Mech. *64*, 193–201.

Wittmann, F.H., Sun, Z., and Zhao, T. (2010). Surface energy and fracture energy. Proc Fram.-7 13–20.

World Congress on Engineering (2016). World Congress on Engineering: WCE 2016: 29 June - 1 July, 2016, London, Imperial College London, U.K. Volume 2: ... (Hong Kong: IAENG, International Association of Engineers).

Xi Yunping, and Nakhi Ammar (2005). Composite Damage Models for Diffusivity of Distressed Materials. J. Mater. Civ. Eng. *17*, 286–295.

Yan, A., Wu, K.-R., Zhang, D., and Yao, W. (2001). Effect of fracture path on the fracture energy of high-strength concrete. Cem. Concr. Res. *31*, 1601–1606.

Yu, A.B. (2004). Discrete element method: An effective way for particle scale research of particulate matter. Eng. Comput. *21*, 205–214.

Zdenek, P., Bazant, Mohammad, K., Hasegawa, T., and Mazars, J. (1991). Size Effect in Brazilian Split-Cylinder Tests: Measurements and Fracture Analysis. ACI Mater. J. *88*.

Zhang, C.-L. (2016). The stress–strain–permeability behaviour of clay rock during damage and recompaction. J. Rock Mech. Geotech. Eng. *8*, 16–26.

Zoback, M.D., and Byerlee, J.D. The effect of microcrack dilatancy on the permeability of westerly granite. (1975). J. Geophys. Res. *80*, 752–755.